UNIVERSIDADE FEDERAL DO RIO GRANDE DO SUL
INSTITUTO DE MATEMÁTICA
PROGRAMA DE PÓS-GRADUAÇÃO EM MATEMÁTICA APLICADA

Nyström method applied to the transport equation in cylindrical geometries

por

César Bublitz

Trabalho submetido como requisito parcial
para a obtenção do título de

Doutor em Matemática Aplicada

Prof. Dr. Fabio Souto De Azevedo
Orientador

Porto Alegre, janeiro de 2022.

CIP - CATALOGAÇÃO NA PUBLICAÇÃO

Bublitz, César

Nyström method applied to the transport equation in cylindrical geometries / César Bublitz.—Porto Alegre: PPGMAp da UFRGS, 2022.

99 p.: il.

Tese (Doutorado) —Universidade Federal do Rio Grande do Sul, Programa de Pós-Graduação em Matemática Aplicada, Porto Alegre, 2022.
Orientador: De Azevedo, Fabio Souto

Tese: Matemática Aplicada,
Matemática Aplicada, Teoria de Transporte de Partículas, Geometria Cilíndrica, Método de Nyström

Nyström method applied to the transport equation in cylindrical geometries

por

César Bublitz

Trabalho submetido ao Programa de Pós-Graduação em Matemática Aplicada do Instituto de Matemática da Universidade Federal do Rio Grande do Sul, como requisito parcial para a obtenção do título de

Doutor em Matemática Aplicada

Linha de Pesquisa: Teoria de Transporte de Partículas

Orientador: Prof. Dr. Fabio Souto De Azevedo

Banca examinadora:

Prof. Dr. Julio Cesar Lombaldo Fernandes
PPGMAp-UFRGS

Prof. Dr. Richard Vasques
The Ohio State University

Prof. Dr. Roberto David Martinez Garcia
IEAv-CTA

Tese defendida em
janeiro de 2022.

Prof. Dr. Lucas da Silva Oliveira
Coordenador

ACKNOWLEDGEMENTS

I would like to thank everyone who contributed to the completion of this research.

My advisor Prof. Dr. Fabio S. de Azevedo, whose insight and knowledge into the subject matter guided me through this work. His support, classes, recommendations, encouragement, and trust in my work have made this an inspiring experience for me.

My parents, for the ethical and moral training.

My teachers, colleagues and friends, for being part of this journey. A special thanks to my colleague and friend Gustavo, who has supported and helped me a lot to finish this work.

The PPGMAp, for the opportunity.

The CAPES and the IFRS, for their financial support.

And last, but definitely not the least, my wife Madalene and my son Bernardo for always trust in me. Thank you for being by my side every time, encouraging me and giving me all the necessary support, for understanding the moments of absence and for lighting up my life every day. I know I would not have finished this thesis without you. Thank you, and I love you!

SUMÁRIO

LISTA DE FIGURAS

LISTA DE TABELAS

LIST OF ACRONYMS AND SYMBOLS

List of Acronyms

ADO	Analytical discrete ordinates
GL	Gauss-Legendre
GSL	GNU Scientific Library
S_N	Discrete ordinates
SK_N	Synthetic kernel
P_N	Spherical harmonics

List of Symbols

c	Mean number of secondary neutrons per collision
D	Domain
E	Particle energy
E	Complete elliptic integral of the second kind
$\mathbf{J}$	Current vector
J	Current
J_r	Radial component of the current
J_z	Axial component of the current
J_θ	Angular component of the current
$\mathbf{J}$	Current vector

K	Complete elliptic integral of the first kind
Ki_1	Bickley-Naylor function of the first kind
Ki_2	Bickley-Naylor function of the second kind
Ki_3	Bickley-Naylor function of the third kind
L	Height of finite cylinder
n	Expected number of particles
$\mathbf{n}$	Unit normal (to surface) vector
N	Number of points of the mesh
P	Surrogate flux
Q	Internal source
r	Radial component of the position variable
R	Cylinder radius
t	Time
v	Particle speed
$\mathbf{x}, \mathbf{y}$	Position variables
z	Axial component of the position variable
α	Boundary incidence angle
δ	Dirac delta distribution
∂D	Boundary of D
θ	Angular component of the position variable

λ_c	Dominant eigenvalue
η	Cosine of the elevation angle
ν	Average number of neutrons produced per fission
σ_t	Total macroscopic cross section
σ_s	Scattering macroscopic cross section
σ_f	Fission macroscopic cross section
σ_c	Critical value
Φ	Scalar flux
Ψ	Angular flux
Ω	Travel direction of the particle
∇	Gradient operator

ABSTRACT

The transport equation has a wide range of applications, such as neutron transport, heat transfer, radiation in gas turbines, radiative cooling of glass, fluorescence tomography, crystal growth of semitransparent materials, and photon and electron radiotherapy. The numerical simulation of this equation tends to be very difficult and the computational complexity arising from the high number of dimensions in the phase space and from its integro-differential structure leads to the challenge of conciliating accuracy and performance. Several different methodologies have been investigated over the years by many research groups. Among them, the Nyström method with the singularity-subtraction technique to the integral formulation has been shown to be as effective as more traditional methods. From the point of view of numerical implementation, the Nyström method is well established for the solution of integral equations and allows good accuracy, noting that the basic idea of the method is to replace the integral operator by a numerical quadrature scheme and produce a linear system to be solved. In recent works of Fabio S. De Azevedo and other researchers, Nyström method was used to solve different classes of two-dimensional problems of neutron transport in X-Y geometry. In such works, analytical and computational refinements were made in order to work with singularities, to obtain numerical precision and to accelerate the computation process, producing high quality numerical results with relatively low computational times. The contribution of the present research goes in this direction, advancing in pre-existent transport theory. High precision numerical results for transport problems in cylindrical geometries are obtained from the mathematical analysis involved, using tools such as elliptic integrals and their properties. The quality of these results shows that the method, in addition to suppressing the ray effects and producing accurate results, has the potential to efficiently treat curved geometries.

RESUMO

A equação do transporte tem uma ampla gama de aplicações, como transporte de nêutrons, transferência de calor, radiação em turbinas a gás, resfriamento radiativo de vidro, tomografia por fluorescência, crescimento de cristais de materiais semitransparentes e radioterapia de fótons e elétrons. A simulação numérica dessa equação tende a ser muito difícil e a complexidade computacional decorrente do elevado número de dimensões no espaço de fase e de sua estrutura integro-diferencial leva ao desafio de conciliar precisão e desempenho. Diversas metodologias diferentes foram investigadas ao longo dos anos por muitos grupos de pesquisa. Entre elas, o método de Nyström com a técnica de subtração de singularidade para a formulação integral tem se mostrado tão eficaz quanto os métodos mais tradicionais. Do ponto de vista da implementação numérica, o método de Nyström está bem estabelecido para a solução de equações integrais e permite boa precisão, sendo a ideia básica do método substituir o operador integral por um esquema de quadratura numérica e produzir um sistema linear para ser resolvido. Em trabalhos recentes de Fabio S. De Azevedo e outros pesquisadores, o método de Nyström foi usado para resolver diferentes classes de problemas de transporte de nêutrons bidimensionais na geometria X-Y. Nesses trabalhos, refinamentos analíticos e computacionais foram feitos para trabalhar com singularidades, obter precisão numérica e acelerar o processo computacional, produzindo resultados numéricos de alta qualidade em tempos computacionais relativamente baixos. A contribuição da presente pesquisa vai nessa direção, avançando na teoria de transporte preexistente. Resultados numéricos de alta precisão, para problemas de transporte em geometrias cilíndricas, são obtidos a partir da análise matemática envolvida, utilizando ferramentas como integrais elípticas e suas propriedades. A qualidade desses resultados mostra que o método, além de suprimir o efeito raio e produzir resultados precisos, tem potencial para tratar geometrias curvas de maneira eficiente.

RESUMO EXPANDIDO

Título: Método de Nyström aplicado à equação do transporte em geometrias cilíndricas

A equação de transporte tem uma ampla gama de aplicações, como transporte de nêutrons [61], transferência de calor [78], radiação em turbinas a gás, resfriamento radiativo de vidro, tomografia de fluorescência, crescimento de cristal de materiais semitransparentes e fótons e radioterapia de elétrons [82]. Uma pesquisa contínua na comunidade da matemática aplicada está sendo realizada para expandir as classes de problemas para os quais as soluções analíticas podem ser obtidas, mas o trabalho é limitado a configurações que são muito idealizadas para serem relevantes para a maioria dos problemas encontrados na análise de engenharia [68]. Isso implica na grande necessidade de resolver numericamente a equação de transporte ou, mais efetivamente e de forma a aumentar a precisão e o desempenho, adotar abordagens híbridas que combinem métodos computacionais e refinamentos analíticos.

A equação de transporte de nêutrons é difícil e cara de resolver numericamente devido, em parte, ao grande número de dimensões no espaço de fase e à sua estrutura integro-diferencial [10, 11, 17, 68]. Porém, com o aumento contínuo do poder computacional, diversos métodos numéricos foram desenvolvidos por diversos grupos de pesquisa nas últimas décadas. Listas abrangentes de métodos para resolver a equação de transporte são apresentadas em [4, 8, 11, 43].

A modelagem do processo de transporte de nêutrons geralmente segue duas abordagens diferentes: a abordagem probabilística ou a abordagem determinística [88]. Uma das abordagens determinísticas mais clássicas utilizadas na solução da equação de transporte em diferentes aplicações é o método das ordenadas discretas (S_N), que consiste em discretizar a variável angular e resolver um sistema de equações diferenciais ordinárias. Deve-se notar que tal técnica ou métodos semel-

hantes exibem anomalias computacionais chamadas de "efeito raio", às quais são originadas da discretização da variável angular [8, 28, 64]. Por outro lado, métodos integrais, que consistem em escrever a formulação integral da equação de transporte onde a variável angular não aparece explicitamente (a variável angular é eliminada por integração sobre o ângulo sólido), são conhecidas por atenuar o efeito raio e produzir resultados numéricos mais precisos [9, 87]. No entanto, podem produzir algoritmos complexos com elevado custo computacional [88].

Em sua formulação integral, a equação de transporte é uma equação de Fredholm do segundo tipo, que é um tipo de equação cujas soluções analíticas raramente são possíveis de obter [8]. Uma equação de Fredholm não homogênea do segundo tipo é dada por

$$\phi(t) = y(t) + \lambda \int_a^b K(t,s)\phi(s)ds \tag{1}$$

ou, em notação de operador, $(1 - \lambda L)\phi = y$, onde L é o operador integral. Esta equação tem uma solução ϕ sempre que o operador $1 - \lambda L$ é invertível e a inversão pode ser feita em diferentes espaços funcionais [36]. Em qualquer álgebra de Banach com a norma $\| \cdot \|$, o operador inverso $(1 - \lambda L)^{-1}$ é bem definido pela série de Neumann se

$$\lambda \lim_{k\to\infty} \|L^k\|^{1/k} < 1, \tag{2}$$

o que sempre acontece quando $\lambda\|L\| < 1$ (veja [67, §17, pg. 195] ou [110, §2, pg. 69]). Assim, ϕ admite a representação

$$\phi = (1 - \lambda L)^{-1} y = y + \sum_{n=1}^{\infty} \lambda^n L^n y. \tag{3}$$

Desta forma, a equação (1) pode ser resolvida numericamente pelo método de Nyström, uma abordagem bem estabelecida para a solução de equações integrais que consiste em substituir a integral na equação por um somatório usando-se um esquema de quadratura numérica [40, 85]. Ou seja,

$$\int_a^b K(t,s)\phi(s)ds = \sum_{j=1}^{N} w_j K(t,s_j)\phi(s_j) \tag{4}$$

onde $\{w_j\}_{j=1}^{N}$ são os pesos e $\{s_j\}_{j=1}^{N}$ são os nodos do esquema de quadratura numérica selecionado. Um sistema linear com N variáveis é produzido e sua solução fornece a função ϕ nos pontos s_j da quadratura.

No entanto, observa-se que as integrais podem conter singularidades, que devem ser removidas antes que a quadratura seja aplicada para que se possa obter soluções precisas [108]. Em alguns casos, o problema da singularidade pode ser superado por tratamentos analíticos em tais integrais [78]. Quando $K(t,t)$ não está definido, ou seja, o problema tem uma singularidade diagonal, a aplicação direta do método de Nyström não funciona. Uma estratégia simples para lidar com a singularidade na diagonal, proposta por Loyalka e Tsai [73, 104], é a subtração de singularidade [40, 85], que consiste em reescrever o operador integral da seguinte maneira:

$$\int_a^b K(t,s)\phi(s)ds = \int_a^b K(t,s)[\phi(s)-\phi(t)]ds + \phi(t)\int_a^b K(t,s)ds. \qquad (5)$$

Assim, a singularidade é removida, deixando a integral do núcleo para ser resolvida. Esta também é singular, mas em alguns casos pode ser integrado analiticamente ou transformado em funções conhecidas [29]. O método de Nyström com a técnica de subtração de singularidade foi usado eficientemente por diferentes autores [36, 56, 72, 79, 88].

Recentemente, Azevedo *et al.* [36] e Sauter *et al.* [88] usaram a metodologia proposta por Tsai e Loyalka [73,104] para resolver diferentes classes de problemas bidimensionais (em geometria XY) de transporte de nêutrons. Nestes trabalhos, observou-se que tal método é promissor se combinado com adequados refinamentos matemáticos e computacionais, permitindo a obtenção de resultados precisos para problemas mais complexos em tempos computacionais relativamente baixos.

Nota-se que outros métodos integrais têm se mostrado eficazes no tratamento de problemas de transporte em geometrias cilíndricas [5, 93, 94, 96, 112]. Porém, o número de pesquisas relacionadas ao transporte de partículas em meios

cilíndricos ainda é escasso e a literatura contém apenas um número limitado de trabalhos com resultados de alta precisão. A carência é mais evidente no caso de problemas multidimensionais, como aqueles em que o fluxo escalar e a corrente variam na direção axial, para os quais a maioria dos trabalhos publicados se limita a apresentar os resultados apenas em gráficos.

Desta forma, o objetivo principal deste trabalho é avançar a teoria do transporte pré-existente, dando continuidade aos trabalhos já realizados pelos professores Fabio Souto de Azevedo, Esequia Sauter, Pedro H. de Almeida Konzen, Mark Thompson e Marco Tulio Vilhena, entre eles [37–39, 89, 98, 99]. Em especial, pretende-se dar continuidade ao trabalho desenvolvido em [36] e [88], usando-se o método Nyström com a técnica de subtração de singularidade em problemas de transporte com geometrias cilíndricas. Os principais objetivos estão listados abaixo:

- Ampliar a análise matemática do problema, levando em consideração aspectos como teoria da existência e unicidade de soluções;
- Realizar a simulação numérica de problemas de transporte em geometrias cilíndricas, especialmente para o caso axissimétrico.

Para atingir os objetivos propostos foram consideradas as seguintes suposições para o problema de transporte de nêutrons:

- caso monoenergético;
- regime permanente;
- meio homogêneo;
- meio não multiplicador;
- espalhamento isotrópico;
- fonte isotrópica.

Asim, iniciou-se com o problema:

$$\Omega \cdot \nabla\Psi(\mathbf{x},\Omega) + \sigma_t\Psi(\mathbf{x},\Omega) = \frac{\sigma_s}{4\pi}\int_{S^2}\Psi(\mathbf{x},\Omega')\,d\Omega' + Q, \tag{6a}$$

onde $\mathbf{x} = (x_1, x_2, x_3) \in D$, $\Omega \in S^2$ é a esfera unitária bidimensional em $\mathbb{R}^3$, ou seja, $\Omega = (\Omega_1, \Omega_2, \Omega_3)$, $\Omega_1^2 + \Omega_2^2 + \Omega_3^2 = 1$, e $\nabla\Psi$ é o gradiente de Ψ. A equação é complementada com a condição de contorno dada por

$$\Psi(\mathbf{x},\Omega) = \Psi_b(\mathbf{x},\Omega), \qquad \mathbf{n}\cdot\Omega < 0, \quad \mathbf{x} \in \partial D. \tag{6b}$$

Aqui σ_t e σ_s são as seções de choque macroscópicas total e de espalhamento, respectivamente. Além disso, na equação (6b), $\mathbf{n}$ é o vetor normal externo a D.

Definindo $S(\mathbf{x})$ como o lado direito da equação (3.1a), ou seja,

$$S(\mathbf{x}) := \frac{\sigma_s}{4\pi}\int_{S^2}\Psi(\mathbf{x},\Omega)\,d\Omega + Q. \tag{7}$$

e aplicando o método das características à equação (3.1a), uma expressão para o fluxo escalar Φ foi obtida. Definindo-se os operadores integrais L_g e L_b como

$$(L_gS)(\mathbf{x}) := \int_D S(\mathbf{y})k_1(\mathbf{x},\mathbf{y})\,d\mathbf{y}, \tag{8}$$

$$(L_b\Psi_b)(\mathbf{x},\Omega) := \int_{\partial D}\Psi_b(\mathbf{y},\Omega)k_2(\mathbf{x},\mathbf{y})\,d\mathcal{S}, \tag{9}$$

tal expressão pôde ser reescrita como

$$\Phi = 4\pi L_g\left(\frac{\sigma_s}{4\pi}\Phi + Q\right) + 4\pi L_b\Psi_b, \tag{10}$$

que é equivalente a

$$(1 - \sigma_s L_g)\Phi = 4\pi(L_gQ + L_b\Psi_b). \tag{11}$$

Assim, uma representação em série de Neumann para Φ é dada por

$$\Phi = 4\pi(1-\sigma_sL_g)^{-1}(L_gQ + L_b\Psi_b) = 4\pi\sum_{n=0}^{\infty}\sigma_s^nL_g^n(L_gQ + L_b\Psi_b), \tag{12}$$

a qual foi usada para construir um processo iterativo para calcular Φ.

No presente trabalho foram obtidas soluções numéricas para o problema acima exposto considerados os seguintes domínios:

- Problema 1: Cilindro infinito axissimétrico;
- Problema 2: Cilindro infinito não axissimétrico;
- Problema 3: Cilindro finito axissimétrico.

A obtenção de nossos resultados numéricos consistiu na aplicação do método de Nyström com a estratégia de subtração de singularidade. Para tanto, foi considerada a seguinte sequência de etapas:

1. Cálculo das integrais necessárias, como núcleos e contribuições de fronteira;
2. Utilização do processo iterativo baseado na série de Neumann para calcular o fluxo escalar nos pontos da malha;
3. Aplicação do esquema de quadratura selecionado nas equações apropriadas para calcular a corrente usando-se o fluxo escalar previamente calculado.

Na etapa 2, para calcular o fluxo escalar em pontos fora da malha, uma fórmula de interpolação é usada. Para o Problema 1, o fluxo escalar nos pontos da malha pode ser obtido alternativamente pela solução numérica do sistema linear associado (veja (3.63)).

Todos os algoritmos usados para gerar os resultados numéricos foram implementados em linguagem de programação C e C++. A biblioteca GNU Scientific Library Free Software Foundation (GSL) [45] foi usada para resolver os Problemas 1 e 2. Para o Problema 3, o uso da GSL foi combinado com o uso da biblioteca Cubature [1] para acelerar os cálculos de integrais múltiplas. A abordagem híbrida com bibliotecas permitiu obter resultados de alta qualidade com tempos computacionais reduzidos. Além disso, a paralelização com OpenMP [76] foi usada para acelerar o cálculo e tabulação dos núcleos (na etapa 1) para os Problemas 2 e 3.

Técnicas matemáticas foram aplicadas para lidar com singularidades, otimizar cálculos e reduzir o armazenamento de memória. Por exemplo, as funções de Bickley-Naylor foram tabuladas em tabelas unidimensionais após a remoção das singularidades [36,88]. Para melhorar a precisão, a remoção foi feita apenas próximo ao ponto de singularidade. Além disso, uma interpolação quadrática foi usada para agilizar a obtenção dos resultados numéricos para as funções de Bickley-Naylor.

Resultados numéricos de alta precisão para o fluxo escalar e para a corrente foram obtidos usando um computador pessoal (Intel Core i7-7500U 2.70GHz). Os resultados se mostraram consistentes com os disponíveis na literatura [47, 48, 57, 69, 94, 96, 109, 111, 112]. Mais do que isso, espera-se que sejam mais precisos em diversos casos. Um estudo completo referente ao Problema 1 foi apresentado no artigo [23].

Além disso, deve-se observar que os experimentos numéricos foram realizados para problemas de transporte em geometrias cilíndricas considerando termo fonte e condição de contorno constantes e espalhamento isotrópico, de forma que foi possível comparar os resultados com os disponíveis na literatura. No entanto, com um desenvolvimento matemático adicional, o método também tem potencial de produzir resultados de alta precisão para casos mais gerais de transporte de nêutrons em um cilindro, como problemas envolvendo espalhamento anisotrópico, condição de contorno reflexiva e meio não homogêneo.

1 INTRODUCTION

The transport equation has a wide range of applications, such as neutron transport [61], heat transfer [78], radiation in gas turbines, radiative cooling of glass, fluorescence tomography, crystal growth of semitransparent materials, and photon and electron radiotherapy [82]. The roots of the theory go back more than a century to the Boltzmann equation, formulated initially for the study of the kinetic theory of gases in 1872 by Ludwig Boltzmann [20].

While continuing research in the applied mathematics community is being performed to expand the classes of problems for which analytical solutions can be obtained, the work is limited to configurations that are far too idealized to be relevant for most problems encountered in engineering analysis [68]. This implies the great need to numerically solve the transport equation or, more effectively and in order to increase accuracy and performance, to take hybrid approaches that combine computational methods and analytical refinements.

The neutron transport equation is difficult and costly to solve numerically because, in part, of the high number of dimensions in the phase space and of its integro-differential structure [10, 11, 17, 68]. However, with the increase of computational power, several numerical methods have been developed by many research groups over the past decades. Comprehensive lists of methods to solve the transport equation are presented in [4, 8, 11, 43].

The modeling of the process of neutron transport generally follows two different approaches: the probabilistic approach or the deterministic approach [88]. One of the most classical deterministic approaches used in the solution of the transport equation in different applications is the discrete ordinates method (S_N), which consists in discretizing the angular variable and solving a system of ordinary differential equations. Generalizations and improvements of the discrete ordinates, as

described by Barichello and Siewert [15] and Abreu [35] have been proposed in the last years.

It is also observed that the complexity to numerically solve high dimensional problems motivated the study of simpler problems, especially the one-dimensional transport equation, defined in the space of two dimensions (with a spatial and an angular variable). The LTS_N method, which discretizes the angular variable and applies the Laplace transform to the spatial variable, is one of the methodologies used for one-dimensional transport problems (see [106], [105], [90] and [91]). Estimates for the truncation error of the LTS_N method are presented by Pazos [83] and Hauser [55].

The P_N approximation for the transport equation, which approximates the angular dependence by a finite number of Legendre polynomials, is also a tool used, as shown by Frank [44], Caldeira [25], Garcia *et al.* [49] and Davison [34]. Another example, less accurate but simpler than the P_N approximation, is the SP_N approximation, which was first proposed in [51,52] in order to simplify the transport equation in the context of nuclear engineering problems. Although these approaches have been developed to solve stationary problems in nuclear engineering involving neutron transport, they have been applied to other situations such as radiative transfer theory (see [63]).

It should be noted that discrete ordinates or discrete-ordinates-like methods display computational anomalies, called "ray effects", originating from the discretization of the angular variables [8, 28, 64]. On the other hand, integral methods, which consist in writing the integral formulation of the transport equation where the angular variable does not appear explicitly (the angular variables are eliminated by integration over the solid angle), are known for mitigating ray effects and producing more precise numerical results [9, 87]. However, they may produce complex algorithms with an elevated computational cost [88].

Integral methods have been shown to be effective in treating transport problems in cylindrical geometries [5, 93, 94]. However, the number of researches related with particle transport in cylindrical media is still scarce and the literature contains only a limited number of works with high precision results. The shortage is more evident in the case of multidimensional problems, like those in which scalar flux and current vary in the axial direction, for which most published works are limited to presenting results only in graphics.

High precision benchmarks for problems in one-dimensional (1-D) infinitely long cylinders case were obtained with the use of F_N method [47,48,93,94,97]. The F_N method, a modified version of the C_N method [60], is a technique introduced by Siewert and Benoist [92] that gives an approximation based on singular integral equations and constraints originated from the Placzek lemma. Results for the related problem in radiative transfer theory were provided by Thynell and Özişik [101,102], Wu and Wu [108], Abulwafa and Attia [2, 3], Altaç [5], and Zhou and Li [113]. Although in some of these works more general problems were also considered, the proposed methodologies were not able to provide results with the same precision as those presented by Siewert and Thomas Jr. for the problem proposed in [94].

For the finite solid cylinder problem, papers with different methodologies are available in the literature in the context of radiative transfer theory, predominantly for the axisymmetric case. Thynell [100] presented numerical results for the isotropic scattering case using power series expansions and a collocation method. Li *et al.* [69] used the discrete ordinates method to obtain results for more general cases, especially the anisotropic scattering medium. However, such results were of limited accuracy, as noticed in the papers of Zhang and Sutton [111, 112], which provided more precise results. An integral formulation using a product-integration method [111] and a surface-related integral equation based on source approximation [112] were used by the authors to solve several problems, including cases with space-dependent properties. Wu and Wu [109] used the Nyström method with the

partition-extrapolation technique to provide accurate results for a problem in a finite cylinder exposed to a normal collimated flux on the top surface. Later, such research was extended by Hsu *et al.* [57], who presented numerical results for more complicated cases, such as problems with non-homogeneous scattering media, by using the YIX method and the quadrature method.

Dealing with more complex problems, Chen and Sutton [29, 96] presented good results, although their presentation was limited to graphs. The authors used an integral method to solve two and three-dimensional transport problems in finite cylindrical media, including results for hollow cylinders in [96]. The strategy has limitations in computing scalar flux and current at boundaries, but the removal of singularity from integrals looked promising. It should be noted that for integral methods an effective treatment of the integral singularity is essential in order to obtain accurate solutions [108]. An alternative, proposed by Loyalka and Tsai [73,104], is the Nyström method with the singularity-subtraction technique coupled with the analytical evaluations of the remainder integrals caused by the subtraction process. Nyström method is well-established approach for the solution of integral equations that consists in replacing the integral operator by a quadrature numerical scheme and producing a linear system to be solved. This strategy was efficiently used by different authors [36, 56, 72, 79, 88].

Recently, Azevedo *et al.* [36] and Sauter *et al.* [88] used the methodology proposed by Tsai and Loyalka [73, 104] to solve different classes of two-dimensional problems (in X-Y geometry) of neutron transport. In these works, it was observed that such method is promising if combined with adequate mathematical and computational refinements, allowing the obtainment of accurate results for more complex problems in relatively low computational times.

The contribution of the present research goes in this direction, advancing pre-existent transport theory. Numerical results for transport problems in cylindrical geometries are obtained from the mathematical analysis involved, using the

Nyström method with the singularity-subtraction technique and tools such as elliptic integrals and their properties (see [23]. The results are set side by side with the results available in the literature [47, 48, 57, 69, 94, 96, 109, 111, 112]. The quality of these results shows that the method, in addition to suppressing the ray effects and producing accurate results, has the potential to efficiently treat curved geometries.

1.1 Objectives

Since the formulation of the integro-differential linear Boltzmann equation, several techniques have been developed for its solution. This paper aims to present some of the main mathematical techniques already developed for this purpose. According to the content presented in the literature, important considerations and comparisons should be made regarding methods such as discrete ordinates, spherical harmonics, and SK_N, among others.

In the last years, a great number of articles and other works dealing with the solution of the transport equation under specific conditions have been produced [37]. In this way, the main objective of this work is to advance the pre-existent theory of transport, giving continuity to the works already done by professors Fabio Souto de Azevedo, Esequia Sauter, Pedro H. de Almeida Konzen, Mark Thompson, and Marco Tulio Vilhena, among them [37–39,89,98,99], mainly continuing the work developed in [36] and [88]. The main goals are listed below:

1. Extend the mathematical analysis of the problem, taking into account aspects such as theory of existence and uniqueness of solutions;

2. Perform numerical simulation of transport problems in cylindrical geometries, starting with the axisymmetric case.

1.2 Organization of the Work

This work is divided into five chapters. Here in the first chapter the motivations that led to the development of the research are presented, focusing on the relevance of the problem. In section 1.1, we describe in detail the objectives of the work, dividing them into topics in order to identify relevant problems that can generate publications.

In the second chapter, we briefly describe the mathematical context in which our research project is inserted, based on the pre-existing literature. The third chapter presents the formulation and solution of the problem dealt with in this research. A benchmark problem for an axisymmetric cylinder was set as a one group problem for homogeneous systems, following results that have already been published by our research group, especially the recent articles developed by De Azevedo *et al.* [36] and Sauter *et al.* [88].

In the fourth chapter we present numerical results for the scalar flux and current for several transport problems in cylindrical geometries. We also include the results for a critical problem, which are obtained from the specified size of the cylinder. In addition, computational details and comparisons with data available in the literature are provided. In the last chapter final considerations are made, including perspectives of future work.

2 THE PARTICLE TRANSPORT EQUATION

The modeling and simulation of phenomena involving the transport of particles is a relevant topic of current research in several areas. Interest in the study of electric power generation or even medical applications are among the reasons for experimental, numerical, and computational studies involving the transport of particles (neutrons, for example) [32]. These phenomena can be modeled by the Boltzmann equation, which was formulated initially for the study of the kinetic theory of gases in 1872 by Ludwig Boltzmann [20].

The Boltzmann equation provides a quantitative description of the spatial, directional, energy, and temporal distribution of the particles in material media [17]. The unknown is a distribution function that depicts the temporal evolution of the particle distribution. In the most general cases seven independent variables are required to describe the distribution of particles: three spatial coordinates $\mathbf{x}$, two angles specifying the particle direction of travel Ω, particle energy E, and time t [68].

In the case of uncharged particles (e.g., neutrons and photons), the transport process is of self-diffusion. Based on physical hypotheses such as the particles densities much smaller than the nuclear densities and no interaction between particles, the Boltzmann equation reduces to a linear transport equation (or linear Boltzmann equation) [74]. This equation represents a detailed balance relation between particle production and loss mechanisms over an element in phase space [11]. Then, it can be deduced from a particle balance performed in the phase space of the problem, that is, space of the magnitude variations where position and direction change. A detailed study on the properties and derivation of the Boltzmann equation, as well as the description in its linear and linearized form, can be found in the books of Bell and Glasstone [17], and Duderstadt [43]. Modest [78] presents a complete study in the context of radiative transfer.

Several forms of the neutron transport equation exist, each one with a particular mathematical property facilitating a class of solutions. Among them are integral even/odd parity, slowing down kernel, multiple collision, invariant embedding, singular integral, Green's function, pseudo flux, and the most popular form in neutron transport and reactor physics applications: the integro-differential formulation [47].

For most purposes it is more economical to formulate transport problems in terms of the angular flux $\Psi(\mathbf{x}, \Omega, E, t) = vn(\mathbf{x}, \Omega, E, t)$, where v is the particle speed and n is the expected number of particles in a volume element dV about $\mathbf{x}$ traveling in the cone of directions $d\Omega$ about Ω with energies between E and $E + dE$ at time t. The angular flux is particularly useful since it serves as a starting point for the calculation of both reaction rates and boundary crossings [68]. However, for most purposes the direction that the particles are traveling is immaterial in calculating reactions rates. Thus, the scalar flux is defined as the integral of Ψ over all directions

$$\Phi(\mathbf{x}, E, t) = \int \Psi(\mathbf{x}, \Omega, E, t) d\Omega. \tag{2.1}$$

According to Lewis and Miller [68], if spatial domain within which the neutron transport equation is to be solved has volume V, the time independent transport equation in a non-multiplying media (photons systems and neutrons systems where no fissionable isotopes are present) in one energy group is given by

$$[\Omega \cdot \nabla + \sigma_t(\mathbf{x})]\, \Psi(\mathbf{x}, \Omega) = \int_{S^2} \sigma_s(\mathbf{x}, \Omega' \cdot \Omega) \Psi(\mathbf{x}, \Omega')\, d\Omega' + Q(\mathbf{x}, \Omega), \tag{2.2}$$

where $\Psi(\mathbf{x}, \Omega)$ stands for the angular flux of neutrons in a volume element dV, $d\Omega$ is the incremental solid angle, $\mathbf{x} = (x_1, x_2, x_3)$ is the position vector, $S^2 \ni \Omega$ is the two-dimensional unit sphere in $\mathbb{R}^3$, that is, $\Omega = (\Omega_1, \Omega_2, \Omega_3)$, $\Omega_1^2 + \Omega_2^2 + \Omega_3^2 = 1$ where Ω is the direction of travel of the particles, $\sigma_t(\mathbf{x})$ is the macroscopic total cross section, and $\sigma_s(\mathbf{x}, \Omega' \cdot \Omega)$ is the the macroscopic differential scattering cross

section. The internal source is given by the term $Q(\mathbf{x}, \Omega)$ and ∇ is the gradient operator.

The integral in equation (2.2) is evaluated in all directions in the unitary sphere. To solve the transport equation, the flux distribution entering across a surface that surrounds V must be known. In other words, if $\mathbf{n}$ is an outward normal to surface, then $\Psi(\mathbf{x}, \Omega, E, t)$ for $\mathbf{n} \cdot \Omega < 0$ and $\mathbf{x}$ on the boundary are required as boundary data.

In the case of neutron transport, the interaction of neutrons can occur with the nuclei of the elements that compose the material media in various ways, such as absorption (e.g., fission) and scattering. Such processes are measured using the concept of macroscopic cross section, which is the inverse of the mean free path. The macroscopic cross section represents the probability of interaction of the neutron per unit path length for a neutron travelling from position $\mathbf{x}$ and in the direction Ω in an interval of directions $d\Omega$ around Ω. Thus, the total cross section can be divided into cross sections for particular types of reactions between particles [42].

Moreover, if we consider a multiplying media containing fissionable material, important subject in the study of nuclear reactors for example, an understanding of the criticality of a system becomes necessary. Physically, the system is said to be critical if there is a self-sustaining time-independent chain reaction in the absence of external sources of neutrons, i.e., if neutrons are inserted into a critical system, then after sufficient time has elapsed for the decay of transient effects, a time-independent asymptotic distribution of neutrons will exist in which the rate of fission neutron production is just equal to the losses and leakage from the system. From the mathematical point of view, a system is critical if a time-independent non-negative solution to the source-free transport equation can be found. Criticality calculations are normally expressed into the form of eigenvalue problems, where the eigenvalue provides a measure of whether the system is subcritical, critical, or supercritical.

2.1 Solution Methods to the Transport Equation

In the 1940s, the advent of nuclear chain reactors arose the interest in solving neutral particle transport problems in the broad range of geometrical configurations found in nuclear reactor and radiation shielding applications. Since then, several analytical methods have been emerged, such as the Weiner-Hopf technique, Case's method (singular eigenfunction expansions), and other analytical techniques that have provided a great deal of insight into the nature of transport processes through the study of highly idealized configurations. The most important of these results have been incorporated into standard reactor theory texts [17, 34, 43, 68].

Given the complexity of the analytical treatment, in the last decades several sophisticated numerical methods have been developed by different research groups. Numerical methods are classified in two categories, namely, deterministic and probabilistic. Here, we will discuss briefly some of the main approaches in transport theory.

2.1.1 Deterministic Methods

Among deterministic methodologies are discrete ordinates methods, which consist in discretizing the angular variable (by approximating the integral term in equation (2.2) by a numerical quadrature) and solving a system of ordinary differential equations. In this context there are two main challenges: a good choice of discrete directions and an accurate treatment of the spatial variable. These aspects are essential to produce computationally efficient discretizations and accurate results. The system of ordinary differential equations obtained from the angular discretization has been solved by many approaches such as Diamond Difference, Spectral Green Function, Arbitrarily High Order Transport, Finite Element Method, and Finite Volume Methods [88].

Although they can be easily applied, all the methods which deal with the solution of the Boltzmann equation using discrete ordinates or discrete-ordinates-like methods display computational anomalies called ray effects. This is due to the discretization of the angular variables, so that the solutions contain spatial ripples which are not accounted by the physics of the problem [8]. Ray effects were first discovered by Gelbard [50], who presented anomalous numerical results obtained from discrete ordinates approximations during a panel discussion of problems in reactor mathematics. The anomalies tend to have the greater consequences in two-dimensional problems where the sources are localized and the effects of scattering are relatively small [68].

The numerical inaccuracies are more pronounced if a small number of discrete directions is used, but they are remarkably persistent even when high-order discrete ordinates approximations are used, i.e. if larger numbers of directions are allowed [8,64]. More specifically the increase in the discrete ordinates order increases the frequency error, but decreases its magnitude [65]. It should be mentioned, also, that the discrete ordinates method can suffer from false scattering (known as numerical smearing where sharp beams are erroneously smoothed) [9, 28, 78]. A comprehensive discussion about ray effects is presented in [64] and [28].

Since ray effects result from the inability of S_N to integrate accurately over the angular flux, some alternative angular treatments have been investigated [68]. Among them is the analytical discrete ordinates (ADO) method, which was proposed by Barichello and Siewert [15]. Such method consists in constructing the homogeneous solution of the associated problem in terms of separation constants and eigenfunctions, which are defined by expressions involving eigenvalues and eigenvectors, being the solution obtained analytically in the spatial variable [32]. In this approach the solution of the transverse integrated one-dimensional equations are explicitly written in terms of the spatial variables and the general solutions are obtained from a spectral method where the associated eigenvalue problem is of re-

duced order, to only half of the number of discrete directions [33]. The ADO method has been widely used for solving multidimensional transport problems in the last years [13, 14, 16, 33, 84, 103].

The ADO method is a nodal methodology where no approximations are used to express the source term. Nodal methods are known as coarse mesh methods and since the original equation is transversely integrated in one or more spatial variables the dimension of the model is reduced such that the resulting formulation may be more easily associated with analytical approaches. In general, the angular flux in the node is represented by low order polynomials as well as the unknown leakage terms arising from the transverse integration [12, 16, 33, 66].

One of the widely used approaches is the diffusive approximation, that consists in solving a transport problem by using the diffusion equation [34], which is known to be an asymptotic limit of the transport equation [62]. This approach has some merit but, although very easy to solve, the diffusion equation is inaccurate in optically thin regions and where the gradient of the energy density is large [21, 78]. The method also produces inaccurate results when absorption is not small or when a source term dominates the solution. Moreover, it is observed that in many applications, only a part of the physical system is diffusive, and it may not be obvious where this diffusive part is. In addition, some energy groups may be diffusive, while others are not and, for time-dependent problems, some regions of space-energy phase space may be diffusive for certain times but not for others [11]. For these reasons, the diffusive approximation may not provide precise solutions to diverse transport problems.

The diffusive approximation and P_1 are very closely related, being equivalent for some transport problems [21]. The multigroup P_1 equations and the diffusion equations are the most widely used in reactor problems [17]. The spherical harmonics (P_N) method [59], which consists in expand the angular dependence of the flux Ψ in terms of Legendre polynomials of the angular variables, is one the earli-

est methods applied to the solution of integro-differential equations in both neutron transport theory and thermal radiative transfer [8, 17, 34]. Accurate results can be obtained by the P_1 method, as for the case of an optically thick media in a diffusive system, as well as for hot, radiating media in cold surroundings [78].

The P_1 approximation is easy to apply and solve. However, the solutions of the spherical harmonic equations for large N are difficult to obtain due to a complicated coupling present in these equations [8, 78]. Another point to note is that even-order approximations for P_N method are not commonly used because they usually produce less accurate results [17]. In addition, while the S_N method suffers from ray effects, the P_N equations suffer from wave effects in time dependent problems [21].

Most frequently applied to situations where the effects of anisotropic scattering are small, integral methods are based on integrating out the angular dependence from the transport equations. This leaves one to deal only with the scalar flux and, in some cases, the partial currents crossing cell boundaries [68]. By integrating out the angular dependence one can treat the angular variables with the accuracy to which one is willing to evaluate the kernels numerically [8]. In this way, integral methods are known to provide precise numerical results, although they may produce complex algorithms with elevated computational cost (prohibitive requirements for computer memory and execution time). However, the Nyström method and the Synthetic Kernel method are two schemes for the integral formulation which have been provided good results in recent publications [5, 9, 10, 36, 88].

The SK_N method [7,8,95] relies on approximating the integral transport kernels by a sum of diffusion-like kernels that preserve spatial moments of the kernels, i.e., replacing the kernels by Gaussian summation over the integration parameter [8]. Thus, the integral equation is converted in a set of second-order coupled differential equations [9]. The ray effects are completely removed by this method, but it did not provide high precision in the early results for cylindrical and spherical problems

[8, 41]. Cylindrical geometry is difficult to treat due to the fact that even in one spatial dimension two angular variables are necessary to describe the angular flux [68].

The Nyström method [81] is a well-established approach for the solution of integral equations and consists in replacing the integral operator by a quadrature numerical scheme, producing a linear system to be solved. In 1975 and 1976, Tsai and Loyalka [73, 104] drew attention to the application of the Nyström method with the singularity-subtraction strategy to the integral formulation of the transport equation in a seminal series of notes discussing the best way to solve the neutron transport equation at those times. Their work was limited by the lack of computational power at the time, but it was pointed that the approach had some merit mainly for the fact of suppressing ray effects, although very time consuming.

2.1.1.1 Nyström Method

In its integral formulation, the transport equation is a Fredholm equation of the second kind, which is a type of equation whose analytical solutions are rarely possible to obtain [8]. An inhomogeneous Fredholm equation of the second kind is given by

$$\phi(t) = y(t) + \lambda \int_a^b K(t,s)\phi(s)ds \tag{2.3}$$

or, in operational notation, $(1 - \lambda L)\phi = y$, where L is the integral operator. This operator equation has a solution ϕ whenever the operator $1 - \lambda L$ is invertible and this inversion may be done in different functional spaces [36]. In any Banach algebra with norm $\|\cdot\|$, the inverse operator $(1 - \lambda L)^{-1}$ is well-defined by the Neumann series if

$$\lambda \lim_{k\to\infty} \|L^k\|^{1/k} < 1, \tag{2.4}$$

which always happens when $\lambda\|L\| < 1$ (see [67, §17, pg. 195] or [110, §2, pg. 69]). Then, ϕ admits the representation

$$\phi = (1 - \lambda L)^{-1} y = y + \sum_{n=1}^{\infty} \lambda^n L^n y. \tag{2.5}$$

In this way, equation (2.3) can be solved numerically by the Nyström method, which consists in replacing the integral in the equation with a summation by a selected numerical quadrature scheme [40, 85]. That is,

$$\int_a^b K(t,s)\phi(s)ds = \sum_{j=1}^{N} w_j K(t,s_j)\phi(s_j) \tag{2.6}$$

where $\{w_j\}_{j=1}^N$ are the weights and $\{s_j\}_{j=1}^N$ are the nodes of the numerical quadrature scheme. A linear system with N variables is produced and its solution provides the function ϕ in the quadrature points s_j.

Nonetheless, integrands may contain singularities, which must be removed before the quadrature can be applied. In some cases the problem of singularities may be overcome by analytical treatments in such integrals [78]. When $K(t,t)$ is not defined, i.e. the problem has a diagonal singularity, the direct application of the Nyström method does not work. A simple strategy to deal with the singularity on the diagonal is the singularity-subtraction [40, 85], which consists in rewriting the integral operator as follows:

$$\int_a^b K(t,s)\phi(s)ds = \int_a^b K(t,s)[\phi(s) - \phi(t)]ds + \phi(t)\int_a^b K(t,s)ds. \tag{2.7}$$

Thus, the singularity is removed, while leaving the integral of the kernel to be evaluated. This remainder is singular also, but in some cases can be integrated analytically or transformed to known functions [29].

2.1.2 Probabilistic Methods

Several mathematical problems may be solved by statistical methods, through sampling techniques, with any degree of accuracy. The precision of the

prediction dependent primarily on the sample size. Solving mathematical problems statistically always involves the use of random numbers and for this reason these sampling methods are called Monte Carlo methods. Monte Carlo is not an approximation of the transport equation and the name does not refer to a single scheme so that any method of solving a mathematical problem with an appropriate statistical sampling technique is commonly referred to as a Monte Carlo method [78].

While the transport equation describes the statistical average of the particles in the system, Monte Carlo methods try to build up an average by simulating many individual particles [21]. In neutron transport calculations, the applicability of the Monte Carlo techniques arises from the fact that the macroscopic cross section may be interpreted as a probability of interaction per unit distance traveled by a neutron. The strategy consists in generating a set of neutron histories by following individual neutrons through successive collisions. The locations of actual collisions and the results of such collisions, e.g., direction and energy of the emerging neutrons, are determined from the range of possibilities by sets of random numbers [17].

One of the advantages of the Monte Carlo technique is that it can solve complicated problems. It has proved useful in special cases, such as complex geometries, where other methods encounter difficulties [78]. Moreover, when there is considerable detail in the variation of the neutron cross section with energy, the Monte Carlo technique eliminates the necessity for making subsidiary calculations, for example, of resonance flux, being useful in the multigroup approximations [17].

Although it generally yields very accurate results, the main disadvantage of the method is its high consumption of time and memory. Another negative point of the Monte Carlo methods is that, as statistical methods, they are subject to statistical error [78]. In addition, usually the Monte Carlo simulation has the largest error where there are the fewest particles in contrast to the deterministic approximations which have a uniform error throughout the system. In particular,

in very rare cases, the simulation can produce completely wrong results, especially in important regions of the domain where there are not many particles [21].

3 FORMULATION AND SOLUTION OF THE PROBLEMS

We consider the following assumptions for the neutron transport problem:

- monoenergetic case;
- steady-state;
- homogeneous medium;
- nonmultiplying medium;
- isotropic scattering;
- isotropic source.

That is, we begin with the problem:

$$\Omega \cdot \nabla \Psi(\mathbf{x}, \Omega) + \sigma_t \Psi(\mathbf{x}, \Omega) = \frac{\sigma_s}{4\pi} \int_{S^2} \Psi(\mathbf{x}, \Omega')\, d\Omega' + Q, \tag{3.1a}$$

where $\mathbf{x} = (x_1, x_2, x_3) \in D$, $\Omega \in S^2$ is the two-dimensional unit sphere in $\mathbb{R}^3$, i.e., $\Omega = (\Omega_1, \Omega_2, \Omega_3)$, $\Omega_1^2 + \Omega_2^2 + \Omega_3^2 = 1$, and $\nabla\Psi$ is the gradient of Ψ. The equation is complemented with the boundary condition given by

$$\Psi(\mathbf{x}, \Omega) = \Psi_b(\mathbf{x}, \Omega), \qquad \mathbf{n} \cdot \Omega < 0, \quad \mathbf{x} \in \partial D. \tag{3.1b}$$

Here σ_t and σ_s are total and scattering macroscopic cross sections, respectively. Furthermore, in equation (3.1b), $\mathbf{n}$ is the outward unit normal vector. We note that, in this formulation, the ratio σ_s/σ_t corresponds to the mean number of secondary neutrons emerging (isotropically) from an interaction (see [79]).

In this context, the scalar flux and the current can be defined by, respectively,

$$\Phi(\mathbf{x}) = \int_{S^2} \Psi(\mathbf{x}, \Omega)\, d\Omega \tag{3.2}$$

and

$$\mathbf{J}(\mathbf{x}) = \int_{S^2} \Omega\Psi(\mathbf{x}, \Omega)\, d\Omega. \tag{3.3}$$

3.1 Two-dimensional Problems

We consider $\mathbf{x} \in D \times \mathbb{R}$, $D \subset \mathbb{R}^2$, with $\nabla\Psi(\mathbf{x}, \Omega) = \frac{\partial\Psi}{\partial x_1}\vec{i} + \frac{\partial\Psi}{\partial x_2}\vec{j}$, i.e., the medium is infinite and Ψ does not vary in x_3 direction.

To solve the problem described by equations (3.1) [36, 88], initially we consider vacuum boundary conditions and then treat the general case. Thus, we start with the auxiliary problem

$$\Omega \cdot \nabla\Psi(\mathbf{x}, \Omega) + \sigma_t\Psi(\mathbf{x}, \Omega) = S(\mathbf{x}), \quad \mathbf{x} \in D \times \mathbb{R}, \quad D \subset \mathbb{R}^2, \quad \Omega \in S^2, \tag{3.4a}$$

$$\Psi(\mathbf{x}, \Omega) = 0, \qquad \mathbf{n} \cdot \Omega < 0, \quad \mathbf{x} \in \partial D \times \mathbb{R}, \tag{3.4b}$$

where the function $S(\mathbf{x})$ represents the right-hand side of the equation (3.1a), i.e.,

$$S(\mathbf{x}) := \frac{\sigma_s}{4\pi} \int_{S^2} \Psi(\mathbf{x}, \Omega)\, d\Omega + Q. \tag{3.5}$$

By applying the method of characteristics [78] to equation (3.4a), we obtain

$$\Psi(\mathbf{x}, \Omega) = \int_0^{s(\mathbf{x},\Omega)} S(\mathbf{x} - t\Omega)e^{-\sigma_t t}\, dt, \tag{3.6}$$

where $s(\mathbf{x}, \Omega) = \sup_{s>0} \{s : \mathbf{x} - s\Omega \in D \times \mathbb{R}\}$. In this context, we write the scalar flux as

$$\Phi(\mathbf{x}) = \int_{S^2} \int_0^{s(\mathbf{x},\Omega)} S(\mathbf{x} - t\Omega)e^{-\sigma_t t}\, dt\, d\Omega. \tag{3.7}$$

The change of variables $\mathbf{y} = \mathbf{x} - t\Omega$, associated to $d\mathbf{y} = t^2 dt d\Omega$ (note that $d\mathbf{y} = dy_1 dy_2 dy_3$), produces [70]

$$\Phi(\mathbf{x}) = \int_{D\times\mathbb{R}} S(\mathbf{y}) \frac{e^{-\sigma_t|\mathbf{x}-\mathbf{y}|}}{|\mathbf{x}-\mathbf{y}|^2}\, d\mathbf{y} = 2\int_0^\infty \int_D S(\mathbf{y}) \frac{e^{-\sigma_t|\mathbf{x}-\mathbf{y}|}}{|\mathbf{x}-\mathbf{y}|^2}\, d\mathbf{y}. \tag{3.8}$$

Now, if we write $|\mathbf{x}-\mathbf{y}|_2 := \sqrt{(x_1-y_1)^2 + (x_2-y_2)^2}$ and introduce the cosine of the elevation angle η by

$$\eta := \frac{\sqrt{(x_1-y_1)^2 + (x_2-y_2)^2}}{\sqrt{(x_1-y_1)^2 + (x_2-y_2)^2 + (x_3-y_3)^2}} = \frac{|\mathbf{x}-\mathbf{y}|_2}{|\mathbf{x}-\mathbf{y}|}, \tag{3.9}$$

we finally obtain (by abuse of notation we will denote $dy_1 dy_2$ by $d\mathbf{y}$)

$$\Phi(\mathbf{x}) = \int_0^1 \int_D S(\mathbf{y}) \frac{e^{-\frac{\sigma_t}{\eta}|\mathbf{x}-\mathbf{y}|_2}}{\sqrt{1-\eta^2}|\mathbf{x}-\mathbf{y}|_2}\, dy_1\, dy_2\, d\eta = 4\pi \int_D S(\mathbf{y}) k_1(\mathbf{x},\mathbf{y})\, d\mathbf{y}. \tag{3.10}$$

Here, we note that the kernel $k_1(\mathbf{x},\mathbf{y})$ can be expressed as

$$k_1(\mathbf{x},\mathbf{y}) := \frac{1}{2\pi}\frac{1}{|\mathbf{x}-\mathbf{y}|_2}\int_0^1 \frac{e^{-\frac{\sigma_t}{\eta}|\mathbf{x}-\mathbf{y}|_2}}{\sqrt{1-\eta^2}}\, d\eta = \frac{1}{2\pi}\frac{\mathrm{Ki}_1(\sigma_t|\mathbf{x}-\mathbf{y}|)}{|\mathbf{x}-\mathbf{y}|_2}. \tag{3.11}$$

where $\mathrm{Ki}_1(t)$ stands for the Bickley-Naylor function of the first kind, i.e., the integral of the modified Bessel function of the second kind, $K_0(t)$ (see [6] and [80, §10.43]), which admits the representation

$$\begin{aligned}\mathrm{Ki}_1(t) = \frac{\pi}{2} &+ t\left[\gamma + \ln(t/2)\right]\sum_{j=0}^{\infty}\frac{(t/2)^{2j}}{(j!)^2(2j+1)} \\ &- t\sum_{j=0}^{\infty}\frac{(t/2)^{2j}}{(j!)^2(2j+1)^2} - t\sum_{j=0}^{\infty}\frac{(t/2)^{2j}H(j+1)}{(j!)^2(2j+1)},\end{aligned} \tag{3.12}$$

where

$$H(j+1) = 1 + \frac{1}{2} + \frac{1}{3} + \cdots + \frac{1}{j}. \tag{3.13}$$

and γ is the Euler-Mascheroni constant.

Now, if we consider the original boundary condition (3.1b), the method of characteristics produces [23]

$$\Psi(\mathbf{x},\Omega) = \Psi_b(\mathbf{x} - s\Omega, \Omega)e^{-\sigma_t s} + \int_0^{s(\mathbf{x},\Omega)} S(\mathbf{x} - t\Omega)e^{-\sigma_t t}\, dt, \tag{3.14}$$

and the scalar flux can be rewritten as

$$\begin{aligned}\Phi(\mathbf{x}) &= \int_{S^2}\int_0^{s(\mathbf{x},\Omega)} S(\mathbf{x}-t\Omega)e^{-\sigma_t t}\,dt\,d\Omega + \int_{S^2}\Psi_b(\mathbf{x}-s\Omega,\Omega)e^{-\sigma_t s}\,d\Omega \\ &= 4\pi\int_D S(\mathbf{y})k_1(\mathbf{x},\mathbf{y})\,d\mathbf{y} + 4\pi\int_{\partial D}\Psi_b(\mathbf{y},\Omega)k_2(\mathbf{x},\mathbf{y})\,d\mathcal{S},\end{aligned} \tag{3.15}$$

where $d\mathcal{S}$ is the surface element.

Here, we observe that the kernel $k_2(\mathbf{x},\mathbf{y})$ can be expressed in terms of the Bickley-Naylor function of the second kind $\mathrm{Ki}_2(t)$ (see [18, 19] and [80, §10.43]) as

$$\begin{aligned}k_2(\mathbf{x},\mathbf{y}) &:= \frac{1}{2\pi}\frac{(\mathbf{y}-\mathbf{x})\cdot\mathbf{n}}{|\mathbf{x}-\mathbf{y}|_2^2}\int_0^1 \frac{\eta e^{-\frac{\sigma_t}{\eta}|\mathbf{x}-\mathbf{y}|_2}}{\sqrt{1-\eta^2}}\,d\eta \\ &= \frac{1}{2\pi}\frac{(\mathbf{y}-\mathbf{x})\cdot\mathbf{n}}{|\mathbf{x}-\mathbf{y}|_2^2}\int_0^1 e^{-\frac{\sigma_t}{\sqrt{1-\eta^2}}|\mathbf{x}-\mathbf{y}|_2}\,d\eta. \\ &= \frac{1}{2\pi}\frac{(\mathbf{y}-\mathbf{x})\cdot\mathbf{n}}{|\mathbf{x}-\mathbf{y}|_2^2}\mathrm{Ki}_2(\sigma_t|\mathbf{x}-\mathbf{y}|)\end{aligned} \tag{3.16}$$

noting that $\mathrm{Ki}_2(t)$ admits the representation

$$\begin{aligned}\mathrm{Ki}_2(t) = 1 - \frac{\pi}{2}t - \frac{t^2}{2}\left[\gamma + \ln(t/2)\right]\sum_{j=0}^{\infty}\frac{(t/2)^{2j}}{j!(j+1)!(2j+1)} \\ + \frac{t^2}{4}\sum_{j=0}^{\infty}\frac{(4j+3)(t/2)^{2j}}{[(j+1)!(2j+1)]^2} + \frac{t^2}{2}\sum_{j=0}^{\infty}\frac{(t/2)^{2j}H(j+1)}{j!(j+1)!(2j+1)}.\end{aligned} \tag{3.17}$$

In order to apply this development to solve the transport equation with $\sigma_s \neq 0$ it is convenient to use an operational notation. We define the integral operators L_g and L_b as

$$(L_g S)(\mathbf{x}) := \int_D S(\mathbf{y})k_1(\mathbf{x},\mathbf{y})\,d\mathbf{y}, \tag{3.18}$$

$$(L_b\Psi_b)(\mathbf{x},\Omega) := \int_{\partial D}\Psi_b(\mathbf{y},\Omega)k_2(\mathbf{x},\mathbf{y})\,d\mathcal{S}, \tag{3.19}$$

so that by definition of $S(\mathbf{x})$, we have

$$\Phi = 4\pi L_g\left(\frac{\sigma_s}{4\pi}\Phi + Q\right) + 4\pi L_b\Psi_b, \tag{3.20}$$

which is equivalent to

$$(1 - \sigma_s L_g)\Phi = 4\pi(L_g Q + L_b \Psi_b). \tag{3.21}$$

Then, Φ admits the Neumann series representation

$$\Phi = 4\pi(1 - \sigma_s L_g)^{-1}(L_g Q + L_b \Psi_b) = 4\pi \sum_{n=0}^{\infty} \sigma_s^n L_g^n (L_g Q + L_b \Psi_b), \tag{3.22}$$

which can be used to build an iterative process to compute Φ.

We observe that the critical value of σ_s is given by $\sigma_c := 1/\|L_g\|_2$ and the representation (3.22) is valid whenever $\sigma_s < \sigma_c$. In [36] it was shown that $\sigma_c \geq \sigma_t$ and $\sigma_c > \sigma_t$ when $\mathbb{R}^2 \backslash D$ is a positive Lebesgue measure set.

3.1.1 Problem 1: Infinite Axisymmetric Cylinder

Let's consider the cylindrical domain $D = \{(x_1, x_2, x_3) : x_1^2 + x_2^2 \leq R^2\}$. We restrict ourselves to the infinitely long axisymmetric cylinder case, i.e., if $\mathbf{x} = (r\cos\theta, r\sin\theta, z)$, the flux $\Phi(\mathbf{x})$ depends only of r. That said, we write $\Phi(\mathbf{x})$ as $\Phi(r)$. The development in the present section has been published in the paper [23]. For more details, see the reference at https://doi.org/10.1016/j.jqsrt.2022.108087.

We start by considering α as the acute angle between $\mathbf{y}$ and the boundary incidence (see Figure 3.1). Then, the equation (3.15) take the form

$$\begin{aligned}
\Phi(r) =& 4\pi \int_D S(r') k_1(\mathbf{x}, \mathbf{y})\, d\mathbf{y} + 4\pi \int_{\partial D} \Psi_b(r') k_2(\mathbf{x}, \mathbf{y})\, d\mathcal{S} \\
=& 4\pi \int_0^R r' S(r') \int_0^{2\pi} k_1(\mathbf{x}, \mathbf{y})\, d\theta dr' + 4\pi \int_0^{2\pi} \Psi_b(\alpha) k_2(\mathbf{x}, \mathbf{y})\, d\theta \\
=& 4\pi \int_0^R S(r') \mathcal{K}(r, r') dr' + 4\pi \mathcal{K}_b(r)
\end{aligned} \tag{3.23}$$

where

$$\mathcal{K}(r, r') = \frac{r'}{2\pi} \int_0^{2\pi} \frac{\mathrm{Ki}_1\left(\sigma_t \sqrt{r^2 - 2rr'\cos(\theta) + r'^2}\right)}{\sqrt{r^2 - 2rr'\cos(\theta) + r'^2}} d\theta \tag{3.24}$$

and

$$\mathcal{K}_b(r) = \frac{R}{2\pi}\int_{-\pi}^{\pi}(R - r\cos(\theta))\Psi_b(\alpha)\frac{\mathrm{Ki}_2\left(\sigma_t\sqrt{r^2 - 2rR\cos(\theta) + R^2}\right)}{r^2 - 2rR\cos(\theta) + R^2}d\theta, \tag{3.25}$$

noting that

$$|\mathbf{x} - \mathbf{y}|_2 = \sqrt{(r - r'\cos\theta)^2 + (r'\sin\theta)^2}. \tag{3.26}$$

To the boundary term, since $\mathbf{n}$ is the unit vector normal to the frontier ∂D, we choose $\mathbf{x} = (r, 0)$, $\mathbf{y} = (R\cos(\theta), R\sin(\theta))$, and $\mathbf{n} = (\cos(\theta), \sin(\theta))$, so that

$$(\mathbf{y} - \mathbf{x}) \cdot \mathbf{n} = (R\cos(\theta) - r)\cos(\theta) + R\sin^2(\theta) = R - r\cos(\theta), \tag{3.27}$$

$$(\mathbf{y} - \mathbf{x}) \times \mathbf{n} = (R\cos(\theta) - r)\sin(\theta) - R\sin(\theta)\cos(\theta) = -r\sin(\theta). \tag{3.28}$$

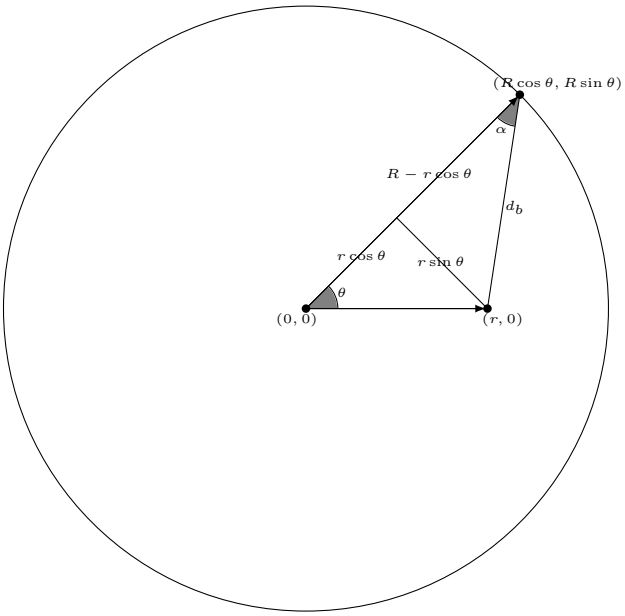

Figure 3.1: Right section of domain of for $\mathbf{y}$ in the frontier.

By starting from equation (3.20) and from the definition of operators L_g and L_b, we obtain

$$\Phi = \int_D \left[\sigma_s\Phi(\mathbf{y}) + 4\pi Q\right] k_1(\mathbf{x}, \mathbf{y})\, d\mathbf{y} + 4\pi\int_{\partial D}\Psi_b(\mathbf{y}, \Omega)k_2(\mathbf{x}, \mathbf{y})\, d\mathcal{S}, \tag{3.29}$$

and, consequently

$$\Phi(\mathbf{x}) = \sigma_s \int_D \Phi(\mathbf{y}) k_1(\mathbf{x},\mathbf{y})\, d\mathbf{y} + 4\pi Q \int_D k_1(\mathbf{x},\mathbf{y})\, d\mathbf{y} \tag{3.30}$$

$$+ \int_{\partial D} \Psi_b(\mathbf{y},\Omega) k_2(\mathbf{x},\mathbf{y})\, d\mathcal{S}. \tag{3.31}$$

Then, it follows that for the axisymmetric case

$$\Phi(r) = \sigma_s \int_0^R \Phi(r')\mathcal{K}(r,r')dr' + 4\pi Q \int_0^R \mathcal{K}(r,r')dr' + 4\pi \mathcal{K}_b(r). \tag{3.32}$$

In order to deal with the diagonal singularity ($r = r'$), we apply the singularity-subtraction strategy [71, 73, 104], i.e., we rewrite the above equation as

$$\Phi(r) = \sigma_s \int_0^R \left[\Phi(r') - \Phi(r)\right] \mathcal{K}(r,r')dr' + \left[\sigma_s \Phi(r) + 4\pi Q\right] B(r) + 4\pi \mathcal{K}_b(r), \tag{3.33}$$

where

$$B(r) := \int_0^R \mathcal{K}(r,r')dr'. \tag{3.34}$$

We compute $\mathcal{K}(r,r')$ numerically and, in order to deal with the singularity in the integrand, we decompose it into three parts, that is, we rewrite

$$\begin{aligned}
\mathcal{K}(r,r') &= \frac{r'}{2\pi} \int_0^{2\pi} \frac{\mathrm{Ki}_1\left(\sigma_t \sqrt{r^2 - 2rr'\cos(\theta) + r'^2}\right)}{\sqrt{r^2 - 2rr'\cos(\theta) + r'^2}} d\theta \\
&= \int_0^{\pi} \int_0^1 \frac{r'}{\pi} \frac{e^{-\frac{\sigma_t \sqrt{r^2 - 2rr'\cos(\theta) + r'^2}}{\eta}}}{\sqrt{1-\eta^2}\sqrt{r^2 - 2rr'\cos(\theta) + r'^2}} d\eta d\theta \\
&= \int_0^{\pi} \int_0^1 \frac{r'}{\pi} \frac{\left(e^{-\frac{\sigma_t d}{\eta}} - e^{-\sigma_t d}\right)}{\sqrt{1-\eta^2} d} d\eta d\theta + \frac{r'}{2} \int_0^{\pi} \frac{e^{-\sigma_t d}}{d} d\theta \\
&= \mathcal{K}_1(r,r') + \frac{r'}{2} \int_0^{\pi} \frac{e^{-\sigma_t d} - 1}{d} d\theta + \frac{r'}{2} \int_0^{\pi} \frac{1}{d} d\theta \\
&= \mathcal{K}_1(r,r') + \mathcal{K}_2(r,r') + \mathcal{K}_3(r,r'),
\end{aligned} \tag{3.35}$$

where

$$d := \sqrt{r^2 - 2rr'\cos(\theta) + r'^2} \tag{3.36}$$

$$\mathcal{K}_1(r, r') := \int_0^\pi \int_0^1 \frac{r'}{\pi} \frac{\left(e^{-\frac{\sigma_t d}{\eta}} - e^{-\sigma_t d}\right)}{\sqrt{1-\eta^2} d} d\eta d\theta \tag{3.37}$$

$$\mathcal{K}_2(r, r') := \frac{r'}{2} \int_0^\pi \frac{e^{-\sigma_t d} - 1}{d} d\theta \tag{3.38}$$

$$\mathcal{K}_3(r, r') := \frac{r'}{2} \int_0^\pi \frac{1}{d} d\theta. \tag{3.39}$$

We observe that $\mathcal{K}_3(r, r')$ can be written in terms of the elliptic integral of the first kind [26] as

$$\begin{aligned} \mathcal{K}_3(r, r') &= \frac{r'}{2} \int_0^\pi \frac{1}{\sqrt{r^2 - 2rr'\cos(\theta) + r'^2}} d\theta \\ &= \frac{r'}{r + r'} \int_0^{\frac{\pi}{2}} \frac{1}{\sqrt{1 - \frac{4rr'}{(r+r')^2}\sin^2(\theta)}} d\theta \\ &= \frac{r'}{r + r'} \mathrm{K}\left(\frac{2\sqrt{rr'}}{r + r'}\right). \end{aligned} \tag{3.40}$$

Here, $\mathrm{K}(t)$ refers to the complete elliptic integral of the first kind (see [54] and [80, §19]),

$$\mathrm{K}(t) = \int_0^{\frac{\pi}{2}} \frac{d\theta}{\sqrt{1 - t^2\sin^2(\theta)}} \tag{3.41}$$

which admits the expansion

$$\mathrm{K}(t) = \frac{\pi}{2} \sum_{n=0}^{\infty} \left(\frac{(2n-1)!!}{(2n)!!}\right)^2 t^{2n} = \frac{\pi}{2} \sum_{n=0}^{\infty} \left(P_{2n}(0)\right)^2 t^{2n} \tag{3.42}$$

where P_n is a Legendre polynomial and !! denotes the double factorial, or

$$\mathrm{K}(t) = \frac{\pi}{2} {}_2F_1\left(\frac{1}{2}, \frac{1}{2}; 1; t^2\right) \tag{3.43}$$

where ${}_2F_1$ is the Gauss hypergeometric function.

To calculate $B(r)$, we will compute the integrals of $\mathcal{K}_1(r, r')$ and of $\mathcal{K}_2(r, r')$ numerically and, in the case of the integral of $\mathcal{K}_3(r, r')$, whose direct numerical integration is very unstable because of the singularity, we will use the following

property (available in [54])

$$\mathrm{K}\left(\frac{2\sqrt{t}}{1+t}\right) = (1+t)\mathrm{K}(t). \tag{3.44}$$

We denote the integral of $\mathcal{K}_3(r,r')$ by $B_3(r)$ and we decompose it into two parts, as follows

$$\begin{aligned} B_3(r) &:= \int_0^R \mathcal{K}_3(r,r')dr' \\ &= \int_0^R \frac{r'}{r+r'}\mathrm{K}\left(\frac{2\sqrt{rr'}}{r+r'}\right)dr' \\ &= \int_0^r \frac{r'}{r+r'}\mathrm{K}\left(\frac{2\sqrt{rr'}}{r+r'}\right)dr' + \int_r^R \frac{r'}{r+r'}\mathrm{K}\left(\frac{2\sqrt{rr'}}{r+r'}\right)dr'. \end{aligned} \tag{3.45}$$

Now, we take $t = \frac{r'}{r}$ in the first part and $t = \frac{r}{r'}$ in the second, and use the given property. Thus, we have

$$\begin{aligned} B_3(r) &= \int_0^1 \frac{tr}{t+1}\mathrm{K}\left(\frac{2\sqrt{t}}{1+t}\right)dt + \int_1^{\frac{r}{R}} \frac{-r}{t^2(t+1)}\mathrm{K}\left(\frac{2\sqrt{t}}{1+t}\right)dt \\ &= \int_0^1 tr\mathrm{K}\left(t\right)dt + \int_1^{\frac{r}{R}} \frac{-r}{t^2}\mathrm{K}\left(t\right)dt \end{aligned} \tag{3.46}$$

Gradshteyn cites in [54] the following results:

$$\int t\mathrm{K}\left(t\right)dt = \mathrm{E}(t) - (1-t^2)\mathrm{K}(t), \tag{3.47}$$

and

$$\int \frac{\mathrm{K}\left(t\right)}{t^2}dt = -\frac{\mathrm{E}(t)}{t}, \tag{3.48}$$

where $\mathrm{E}(t)$ refers to the complete elliptic integral of the second kind (see [27], [54] and [80, §19]):

$$\mathrm{E}(t) = \int_0^{\frac{\pi}{2}} \sqrt{1-t^2\sin^2(\theta)}d\theta, \tag{3.49}$$

which admits the expansion

$$\mathrm{E}(t) = \frac{\pi}{2}\sum_{n=0}^{\infty}\left(\frac{(2n)!}{2^{2n}\left(n!\right)^2}\right)^2 \frac{t^{2n}}{1-2n} \tag{3.50}$$

or

$$\mathrm{E}(t) = \frac{\pi}{2}{}_2F_1\left(\frac{1}{2}, -\frac{1}{2}; 1; t^2\right). \tag{3.51}$$

By using (3.47) and (3.48) into (3.46), we obtain

$$\begin{aligned} B_3(r) &= r\left[(\mathrm{E}(1) - \mathrm{E}(0) + \mathrm{K}(0)) + \left(\frac{R}{r}\mathrm{E}\left(\frac{r}{R}\right) - \mathrm{E}(1)\right)\right] \\ &= r\left(-\mathrm{E}(0) + \mathrm{K}(0) + \frac{R}{r}\mathrm{E}\left(\frac{r}{R}\right)\right). \end{aligned} \tag{3.52}$$

Finally, the fact that $\mathrm{K}(0) = \mathrm{E}(0) = \dfrac{\pi}{2}$ produces

$$\int_0^R \mathcal{K}_3(r, r')dr' = R\mathrm{E}\left(\frac{r}{R}\right). \tag{3.53}$$

Now, to simplify our numerical computation, we also note that for the $\mathcal{K}(r, r')$ term,

$$\mathcal{K}(r, 0) = \frac{0}{2\pi}\int_0^{2\pi} \frac{\mathrm{Ki}_1(\sigma_t r)}{r}d\theta = 0 \tag{3.54}$$

and

$$\mathcal{K}(0, r') = \frac{r'}{2\pi}\int_0^{2\pi} \frac{\mathrm{Ki}_1(\sigma_t r')}{r'}d\theta = \mathrm{Ki}_1(\sigma_t r'), \tag{3.55}$$

and for the $B(r)$ integral we have

$$\begin{aligned} B(0) &= \int_0^{2\pi}\int_0^R\int_0^1 \frac{1}{2\pi}\frac{e^{-\frac{\sigma_t r'}{\eta}}}{\sqrt{1-\eta^2}}d\eta dr' d\theta \\ &= \int_0^R\int_0^1 \frac{e^{-\frac{\sigma_t r'}{\eta}}}{\sqrt{1-\eta^2}}d\eta dr' \\ &= \int_0^1\int_0^R \frac{e^{-\frac{\sigma_t r'}{\eta}}}{\sqrt{1-\eta^2}}dr' d\eta \\ &= \frac{1}{\sigma_t}\int_0^1 \frac{\eta}{\sqrt{1-\eta^2}}\left[1 - e^{-\frac{\sigma_t R}{\eta}}\right]d\eta \\ &= \frac{1}{\sigma_t}\left[1 - \int_0^1 \frac{\eta}{\sqrt{1-\eta^2}}e^{-\frac{\sigma_t R}{\eta}}d\eta\right] \\ &= \frac{1}{\sigma_t}\left[1 - \mathrm{Ki}_2(\sigma_t R)\right]. \end{aligned} \tag{3.56}$$

Moreover, if the boundary condition is constant, we obtain

$$\mathcal{K}_b(0) = \frac{R}{2\pi}\int_{-\pi}^{\pi} \frac{R\Psi_b\mathrm{Ki}_2(\sigma_t R)}{R^2}d\theta = \Psi_b\mathrm{Ki}_2(\sigma_t R). \tag{3.57}$$

3.1.1.1 Boundary Limit

To compute $\mathcal{K}_b(r)$ in $r = R$ we need to understand the behavior of the integral originated in the treatment of the boundary. We consider α as the acute angle between $\mathbf{y}$ and the boundary incidence and state the following theorem:

Theorem 3.1. *The limit of*

$$\int_{\partial D} \Psi_b(\alpha) k_2(\mathbf{x}, \mathbf{y})\, d\mathcal{S}, \tag{3.58}$$

when $r \to R^-$ *is*

$$\int_{\partial D} \Psi_b(\alpha) k_2(\mathbf{x}, \mathbf{y})\, d\mathcal{S} + \frac{1}{2\pi} \int_{-\frac{\pi}{2}}^{\frac{\pi}{2}} \Psi_b(\alpha) d\alpha. \tag{3.59}$$

The proof of this theorem can be seen in the paper [23]. From the theorem, we note that in the case of a constant boundary condition Ψ_b, the quantity $0.5\Psi_b$ has to be added to the value of $\mathcal{K}_b(r)$ computed from equation (3.25) when $r = R$.

3.1.1.2 Numerical Solution by the Nyström Method

Now, we return to equation (3.33) and apply the Nyström method to discretize the integral operator involved, obtaining

$$\begin{aligned} \Phi(r) \approx \sigma_s \sum_{j=1, s_j \neq r}^{N} w_j \mathcal{K}(r, s_j) \left[\Phi(s_j) - \Phi(r)\right] + \left[\sigma_s \Phi(r) + 4\pi Q\right] B(r) \\ + 4\pi \mathcal{K}_b(r), \end{aligned} \tag{3.60}$$

where $\{w_j\}_{j=1}^N$ are the weights and $\{s_j\}_{j=1}^N$ are the nodes of the numerical quadrature scheme selected. This equation in the quadrature points becomes, to $i = 1, \ldots, N$,

$$\begin{aligned} \Phi(r_i) \approx \sigma_s \sum_{j=1, s_j \neq r_i}^{N} w_j \mathcal{K}(r_i, s_j) \left[\Phi(s_j) - \Phi(r_i)\right] + \left[\sigma_s \Phi(r_i) + 4\pi Q\right] B(r_i) \\ + 4\pi \mathcal{K}_b(r_i). \end{aligned} \tag{3.61}$$

Again, to simplify the notation, we define $\mathcal{K}_{ij} = \mathcal{K}(r_i, s_j)$, $B_i = B(r_i)$, $K_{bi} = 4\pi\mathcal{K}_b(r_i)$, and $\Phi_i = \Phi(r_i)$, which is the variable of the discrete problem. Thus, the linear system to solve is given by

$$\Phi_i = \sigma_s \sum_{j=1, j\neq i}^{N} w_j \mathcal{K}_{ij}[\Phi_j - \Phi_i] + [\sigma_s \Phi_i + 4\pi Q]B_i + K_{bi}, \quad i = 1, \ldots, N, \tag{3.62}$$

or, in matrix notation

$$A\Phi = g, \tag{3.63}$$

where Φ and g are the vectors of entries Φ_i and $4\pi QB_i + K_{bi}$, respectively, and the matrix A is given by

$$\begin{bmatrix} 1 + \sigma_s \sum_{l\neq 1} w_l \mathcal{K}_{1l} - \sigma_s B_1 & -\sigma_s w_2 \mathcal{K}_{12} & \cdots & -\sigma_s w_N \mathcal{K}_{1N} \\ -\sigma_s w_1 \mathcal{K}_{21} & 1 + \sigma_s \sum_{l\neq 2} w_l \mathcal{K}_{2l} - \sigma_s B_2 & \cdots & -\sigma_s w_N \mathcal{K}_{2N} \\ \vdots & \vdots & \ddots & \vdots \\ -\sigma_s w_1 \mathcal{K}_{N1} & -\sigma_s w_2 \mathcal{K}_{N2} & \cdots & 1 + \sigma_s \sum_{l\neq N} w_l \mathcal{K}_{Nl} - \sigma_s B_N \end{bmatrix}.$$

The linear system (3.63) can be numerically solved by using Gaussian Elimination with partial pivoting [53] as implemented in the GNU Scientific Library (GSL) [45]. Alternatively, we may use the Neumann series expansion (3.22) to construct the following iterative process [36]:

$$\Phi_i = \sum_{n=0}^{M} \sigma_s^n L_i^n + \frac{\sigma_s^{M+1}\lambda_c}{1 - \sigma_s \lambda_c} L_i^{M+1}, \tag{3.64}$$

where

$$L_i^0 = 4\pi QB_i + K_{bi}, \tag{3.65}$$

$$L_i^{n+1} = \sum_{j=1, j\neq i}^{N} w_j [L_j^n - L_i^n]\mathcal{K}_{ij} + L_i^n \sigma_s B_i, \; n \geq 0, \tag{3.66}$$

and the dominant eigenvalue λ_c can be approximated by the Rayleigh quotient [110]

$$\lambda_c \approx \frac{\langle L^{M-1}, L^M \rangle}{\langle L^{M-1}, L^{M-1} \rangle}. \tag{3.67}$$

In both above presented approaches, the solution of linear system provides the scalar flux at mesh points. However, we may adapt the discretization (3.61) to compute the scalar flux at any point of the domain as follows:

$$\Phi(r) \approx \frac{\sigma_s \sum_{j=1, i\neq j}^{N} w_j \mathcal{K}(r, s_j)\Phi(s_j) + 4\pi Q B(r) + 4\pi \mathcal{K}_b(r)}{1 + \sigma_s \sum_{j=1, i\neq j}^{N} w_j \mathcal{K}(r, s_j) - \sigma_s B(r)}. \tag{3.68}$$

One may use any other alternative interpolation methods to calculate the scalar flux at any point in terms of scalar flux of mesh points, if speed is an issue. However, in our numerical experiments, as well as in the works [36, 88], this strategy yielded accurate results.

3.1.1.3 Computation of the Current

Here we discuss the procedure to calculate the current given by equation (3.3), i.e.

$$\mathbf{J}(\mathbf{x}) = \int_{S^2} \Psi(\mathbf{x}, \Omega)\Omega \, d\Omega.$$

As mentioned in [36], we note that the current $\mathbf{J}(\mathbf{x})$ is a vector in $\mathbb{R}^3$ being denoted in Cartesian coordinates as $\mathbf{J}(\mathbf{x}) = (J_1(\mathbf{x}), J_2(\mathbf{x}), J_3(\mathbf{x}))$. In the case of the infinitely long axisymmetric cylinder, $\mathbf{J}(\mathbf{x})$ depends only on r and the following expression for $J(r) := J_1(\mathbf{x})$ can be obtained in terms of $S(\mathbf{x})$ (see [70] for details):

$$\begin{aligned} J(r) &= \int_D k_J(\mathbf{x}, \mathbf{y}) S(\mathbf{y}) \, d\mathbf{y} + \int_{\partial D} \Psi_b(\mathbf{y}) k_B(\mathbf{x}, \mathbf{y}) \, d\mathcal{S} \\ &= \int_0^R \mathcal{K}_J(r, r') S(r') \, dr' + \mathcal{K}_B(r), \end{aligned} \tag{3.69}$$

with

$$k_J(\mathbf{x}, \mathbf{y}) := \frac{2(x_1 - y_1)}{|\mathbf{x} - \mathbf{y}|_2^2} \int_0^1 \frac{\eta e^{-\frac{\sigma_t}{\eta}|\mathbf{x}-\mathbf{y}|_2}}{\sqrt{1-\eta^2}} \, d\eta = \frac{2(x_1 - y_1)}{|\mathbf{x} - \mathbf{y}|_2^2} \mathrm{Ki}_2(\sigma_t |\mathbf{x} - \mathbf{y}|) \tag{3.70}$$

and

$$\begin{aligned} k_B(\mathbf{x}, \mathbf{y}) &:= 2(x_1 - y_1) \frac{(\mathbf{y} - \mathbf{x}) \cdot \mathbf{n}}{|\mathbf{x} - \mathbf{y}|_2^3} \int_0^1 \frac{\eta^2 e^{-\frac{\sigma_t}{\eta}|\mathbf{x}-\mathbf{y}|_2}}{\sqrt{1-\eta^2}} \, d\eta \\ &= 2(x_1 - y_1) \frac{(\mathbf{y} - \mathbf{x}) \cdot \mathbf{n}}{|\mathbf{x} - \mathbf{y}|_2^3} \mathrm{Ki}_3(\sigma_t |\mathbf{x} - \mathbf{y}|), \end{aligned} \tag{3.71}$$

where $\mathrm{Ki}_3(t)$ stands for the Bickley-Naylor function of the third kind [6]. Furthermore,

$$\mathcal{K}_J(r,r') = 2\int_0^{2\pi} r'(r - r'\cos(\theta))\frac{\mathrm{Ki}_2(\sigma_t d)}{d^2}d\theta, \tag{3.72}$$

and

$$\mathcal{K}_B(r) = 2R\int_{-\pi}^{\pi}(R - r\cos(\theta))(r - R\cos(\theta))\Psi_b(\alpha)\frac{\mathrm{Ki}_3(\sigma_t d_b)}{d_b^3}d\theta. \tag{3.73}$$

Now the equation (3.5) allows us to compute the components of the current $J(r)$ from the previously computed approximations of $\Psi(r)$ and $\Psi_b(r)$ at the mesh points. More precisely we have

$$J(r) = \frac{\sigma_s}{4\pi}\int_0^R \mathcal{K}_J(r,r')\Phi(r')\,dr' + Q\int_0^R \mathcal{K}_J(r,r')\,dr' + \mathcal{K}_B(r). \tag{3.74}$$

To remove the diagonal singularity, we rewrite as

$$\begin{aligned} J(r) = \frac{\sigma_s}{4\pi}\int_0^R \mathcal{K}_J(r,r')\left[\Phi(r') - \Phi(r)\right]\,dr' + \frac{\sigma_s}{4\pi}\int_0^R \mathcal{K}_J(r,r')\Phi(r)\,dr' \\ + Q\int_0^R \mathcal{K}_J(r,r')\,dr' + \mathcal{K}_B(r). \end{aligned} \tag{3.75}$$

Then, it follows that

$$J(r) = \frac{\sigma_s}{4\pi}\int_0^R \mathcal{K}_J(r,r')\left[\Phi(r') - \Phi(r)\right]\,dr' + \left[\frac{\sigma_s}{4\pi}\Phi(r) + Q\right]h(r) + \mathcal{K}_B(r), \tag{3.76}$$

where

$$h(r) = \int_0^R \mathcal{K}_J(r,r')\,dr'. \tag{3.77}$$

By using the quadrature $\{w_k, \rho_k\}$ we have the following approximation for the current

$$J(r) \approx \frac{\sigma_s}{4\pi}\sum_k w_k\mathcal{K}_J(r,\rho_k)\left[\Phi(\rho_k) - \Phi(r)\right] + \left[\frac{\sigma_s}{4\pi}\Phi(r) + Q\right]h(r) + \mathcal{K}_B(r). \tag{3.78}$$

We compute $\mathcal{K}_J(r,r')$ numerically and, again in order to deal with the singularity in the integrand, we decompose it into four integrals, that is, we rewrite

$$\begin{aligned}
\mathcal{K}_J(r,r') &= 4\int_0^\pi r'(r-r'\cos(\theta))\frac{\mathrm{Ki}_2(\sigma_t d)}{d^2}d\theta \\
&= \mathcal{K}_{J1} + 4r\int_0^\pi\int_0^1 \frac{(r-r'\cos(\theta))\eta e^{-\frac{\sigma_t d}{\eta}}}{d^2\sqrt{1-\eta^2}}d\eta d\theta \\
&= \mathcal{K}_{J1} + \mathcal{K}_{J2} + 4r\int_0^\pi\int_0^1 \frac{(r-r'\cos(\theta))\eta e^{-\sigma_t d}}{d^2\sqrt{1-\eta^2}}d\eta d\theta \\
&= \mathcal{K}_{J1} + \mathcal{K}_{J2} + 4r\int_0^\pi \frac{(r-r'\cos(\theta))e^{-\sigma_t d}}{d^2}d\theta \\
&= \mathcal{K}_{J1} + \mathcal{K}_{J2} + \mathcal{K}_{J3} + \mathcal{K}_{J4},
\end{aligned} \tag{3.79}$$

where

$$\mathcal{K}_{J1}(r,r') := 4\int_0^\pi\int_0^1 \frac{(r'-r)(r-r'\cos(\theta))\eta e^{-\frac{\sigma_t d}{\eta}}}{d^2\sqrt{1-\eta^2}}d\eta d\theta, \tag{3.80}$$

$$\mathcal{K}_{J2}(r,r') := 4r\int_0^\pi\int_0^1 \frac{(r-r'\cos(\theta))\eta\left(e^{-\frac{\sigma_t d}{\eta}} - e^{-\sigma_t d}\right)}{d^2\sqrt{1-\eta^2}}d\eta d\theta, \tag{3.81}$$

$$\mathcal{K}_{J3}(r,r') := 4r\int_0^\pi \frac{(r-r'\cos(\theta))\left(e^{-\sigma_t d}-1\right)}{d^2}d\theta, \tag{3.82}$$

$$\mathcal{K}_{J4}(r,r') := 4r\int_0^\pi \frac{(r-r'\cos(\theta))}{d^2}d\theta. \tag{3.83}$$

Here it can be seen that $\mathcal{K}_{J4}$ may be analytically computed, producing

$$\mathcal{K}_{J4}(r,r') = \begin{cases} 0, & \text{if } r' < r \\ 2\pi, & \text{if } r' = r \\ 4\pi, & \text{if } r' > r. \end{cases} \tag{3.84}$$

We also note that for $r' \neq 0$

$$\begin{aligned}
\mathcal{K}_J(0,r') &= 4\int_0^\pi r'(-r'\cos(\theta))\frac{\mathrm{Ki}_2(\sigma_t r')}{r'^2}d\theta \\
&= -4\mathrm{Ki}_2(\sigma_t r')\int_0^\pi \cos(\theta)d\theta = 0
\end{aligned} \tag{3.85}$$

and for $r \neq 0$ the definition of $\mathcal{K}_J$ produces

$$\mathcal{K}_J(r,0) = 4\int_0^\pi 0\frac{\mathrm{Ki}_2(\sigma_t r)}{r^2}d\theta = 4\frac{\mathrm{Ki}_2(\sigma_t r)}{r^2}\int_0^\pi 0 d\theta = 0. \tag{3.86}$$

Moreover, if the boundary condition is constant

$$\begin{aligned}\mathcal{K}_B(0) &= 2R\int_{-\pi}^{\pi}\frac{-R^2\cos(\theta)\Psi_b\mathrm{Ki}_3\left(\sigma_t R\right)}{R^3}d\theta \\ &= -2\Psi_b\mathrm{Ki}_3\left(\sigma_t R\right)\int_{-\pi}^{\pi}\cos(\theta) = 0.\end{aligned} \tag{3.87}$$

Similarly to what was performed to compute $\mathcal{K}_b(r)$ in $r = R$ we need to understand the behavior of the integral originated in the treatment of the boundary in the case of $\mathcal{K}_B(r)$. Here, follows the theorem:

Theorem 3.2. *The limit of*

$$\int_{\partial D}\Psi_b(\mathbf{y})k_b(\mathbf{x},\mathbf{y})\,d\mathcal{S} = \mathcal{K}_B(r) \tag{3.88}$$

when $r \to R^-$ *is*

$$\mathcal{K}_B(r) - \int_{-\frac{\pi}{2}}^{\frac{\pi}{2}}\Psi_b(\alpha)d\alpha. \tag{3.89}$$

The proof of this theorem can be seen in the paper [23]. From the theorem, we note that in the case of a constant boundary condition Ψ_b, the quantity $-\pi\Psi_b$ has to be added to the value of $\mathcal{K}_B(r)$ computed from equation (3.73) when $r = R$.

3.1.2 Problem 2: Infinite Non-axisymmetric Cylinder

Now we consider the general non-axisymmetric case for the two-dimensional cylindrical domain $D = \{(x_1, x_2) : x_1^2 + x_2^2 \leq R^2\}$. In this context, by beginning with the equation (3.1a) and the boundary condition (3.1b), the scalar flux (see equation (3.15)) takes the form

$$\begin{aligned}\Phi(\mathbf{x}) &= 4\pi\int_D S(\mathbf{x},\mathbf{y})k_1(\mathbf{x},\mathbf{y})\,d\mathbf{y} + 4\pi\int_{\partial D}\Psi_b(\mathbf{y},\Omega)k_2(\mathbf{x},\mathbf{y})\,d\mathcal{S} \\ &= 4\pi\int_0^R\int_0^{2\pi} r' S(\mathbf{x},\mathbf{y})k_1(\mathbf{x},\mathbf{y})\,d\theta' dr' + 4\pi\int_0^{2\pi}\Psi_b(\mathbf{y},\Omega)k_2(\mathbf{x},\mathbf{y})\,d\theta' \\ &= 4\pi\int_0^R\int_0^{2\pi} S(r',\theta')k_a(\mathbf{x},\mathbf{y})\,d\theta' dr' + 4\pi\int_{-\pi}^{\pi}\Psi_b(r',\theta')k_b(\mathbf{x},\mathbf{y})\,d\theta'\end{aligned} \tag{3.90}$$

where

$$k_a(\mathbf{x},\mathbf{y}) = \frac{r'}{2\pi}\frac{\mathrm{Ki}_1\left(\sigma_t\sqrt{r^2-2rr'\cos(\Theta)+r'^2}\right)}{\sqrt{r^2-2rr'\cos(\Theta)+r'^2}}, \tag{3.91}$$

and

$$k_b(\mathbf{x},\mathbf{y}) = \frac{R}{2\pi}(R-r\cos(\Theta))\frac{\mathrm{Ki}_2\left(\sigma_t\sqrt{r^2-2rR\cos(\Theta)+R^2}\right)}{r^2-2rR\cos(\Theta)+R^2}, \tag{3.92}$$

noting that $\Theta := \theta' - \theta$.

Then, by the definition of $S(\mathbf{x})$ it follows that

$$\begin{aligned}\Phi(\mathbf{x}) = \sigma_s\int_0^R\int_0^{2\pi}\Phi(\mathbf{y})k_a(\mathbf{x},\mathbf{y})d\theta'dr' + 4\pi Q\int_0^R\int_0^{2\pi}k_a(\mathbf{x},\mathbf{y})d\theta'dr' \\ + 4\pi\int_{-\pi}^{\pi}\Psi_b(r',\theta')k_b(\mathbf{x},\mathbf{y})\,d\theta'.\end{aligned} \tag{3.93}$$

In order to deal with the diagonal singularity ($\mathbf{y} = \mathbf{x}$), we begin by rewriting the equation as

$$\begin{aligned}\Phi(\mathbf{x}) = \sigma_s\int_0^R\int_0^{2\pi}\left[\Phi(\mathbf{y})-\Phi(\mathbf{x})\right]k_a(\mathbf{x},\mathbf{y})d\theta'dr' + [\sigma_s\Phi(\mathbf{x})+4\pi Q]K(\mathbf{x}) \\ + H(\mathbf{x}),\end{aligned} \tag{3.94}$$

where

$$K(\mathbf{x}) := \int_0^R\int_0^{2\pi}k_a(\mathbf{x},\mathbf{y})d\theta'dr' \tag{3.95}$$

and

$$H(\mathbf{x}) = 4\pi\int_{-\pi}^{\pi}\Psi_b(r',\theta')k_b(\mathbf{x},\mathbf{y})\,d\theta'. \tag{3.96}$$

Here, it can be noted that $K(\mathbf{x}) = B(r)$ (see equation (3.34)).

3.1.2.1 Computation of the current

From the definition of the current given in (3.3), it follows that:

$$\mathbf{J}(\mathbf{x}) = \int_D \Omega\frac{e^{-\sigma_t|\mathbf{x}-\mathbf{y}|}}{|\mathbf{x}-\mathbf{y}|^2}S(\mathbf{y})\,d\mathbf{y} + \int_{\partial D}\Omega\frac{e^{-\sigma_t|\mathbf{x}-\mathbf{y}|}}{|\mathbf{x}-\mathbf{y}|^2}\Psi_b(\mathbf{y})\,d\mathcal{S}. \tag{3.97}$$

Then, the radial and angular components of the current are given by

$$J_r(r,\theta) = \int_0^{2\pi}\int_0^{R} k_r(r,r',\theta,\theta')S(r',\theta')\,dr'd\theta' + K_{b1}(r,\theta) \tag{3.98}$$

and

$$J_\theta(r,\theta) = \int_0^{2\pi}\int_0^{R} k_\theta(r,r',\theta,\theta')S(r',\theta')\,dr'd\theta' + K_{b2}(r,\theta), \tag{3.99}$$

where

$$k_r(r,r',\theta,\theta') = \frac{2r'(r - r'\cos(\Theta))}{d_j^2}\mathrm{Ki}_2(\sigma_t d_j), \tag{3.100}$$

$$k_\theta(r,r',\theta,\theta') = \frac{-2r'^2\sin(\Theta)}{d_j^2}\mathrm{Ki}_2(\sigma_t d_j), \tag{3.101}$$

$$K_{b1}(r,\theta) = \int_0^{2\pi}\frac{2R(r - R\cos(\Theta))(R - r\cos(\Theta))}{d_r^3}\Psi_b(\mathbf{y})\mathrm{Ki}_3(\sigma_t d_r)d\theta', \tag{3.102}$$

$$K_{b2}(r,\theta) = \int_0^{2\pi}\frac{-2R^2(R - r\cos(\Theta))\sin(\Theta)}{d_r^3}\Psi_b(\mathbf{y})\mathrm{Ki}_3(\sigma_t d_r)\,d\theta', \tag{3.103}$$

$$d_j = \sqrt{r^2 - 2rr'\cos(\Theta) + r'^2}, \tag{3.104}$$

$$d_r = \sqrt{r^2 - 2rR\cos(\Theta) + R^2}. \tag{3.105}$$

Replacing the equation (3.5) in equations (3.98) and (3.99) and removing the singularity from both terms, the radial and angular components of the current can be written as, respectively,

$$\begin{aligned} J_r(r,\theta) = {} & \frac{\sigma_s}{4\pi}\int_0^{L}\int_0^{R} k_r(r,r',\theta,\theta')\left[\Phi(r',\theta') - \Phi(r,\theta)\right]\,dr'd\theta' \\ & + \left[\frac{\sigma_s}{4\pi}\Phi(r,\theta) + Q\right]\int_0^{L}\int_0^{R} k_r(r,r',\theta,\theta')\,dr'd\theta' + K_{b1}(r,\theta), \end{aligned} \tag{3.106}$$

$$\begin{aligned} J_\theta(r,\theta) = {} & \frac{\sigma_s}{4\pi}\int_0^{L}\int_0^{R} k_\theta(r,r',\theta,\theta')\left[\Phi(r',\theta') - \Phi(r,\theta)\right]\,dr'd\theta' \\ & + \left[\frac{\sigma_s}{4\pi}\Phi(r,\theta) + Q\right]\int_0^{L}\int_0^{R} k_\theta(r,r',\theta,\theta')\,dr'd\theta' + K_{b2}(r,\theta). \end{aligned} \tag{3.107}$$

Similarly to the development carried out for the axisymmetric case, the kernels of the integrals of both equations can be decomposed into the sum of multiple integrals (see equation (3.79)). Such decompositions are important to remove the singularity and produce high precision numerical results.

3.1.2.2 Numerical implementation

After removing the singularity, we apply the Nyström method in equation (3.94) to discretize the integral operator involved, obtaining the following expression to the quadrature points $\mathbf{x}_{ij} = (r_i, \theta_j)$:

$$\begin{aligned}\Phi(\mathbf{x}_{ij}) \approx \sigma_s \sum_{(l,m)\neq(i,j)} w_{lm} k_a(\mathbf{x}_{ij}, \mathbf{x}_{lm}) \left[\Phi(\mathbf{x}_{lm}) - \Phi(\mathbf{x}_{ij})\right] \\ +[\sigma_s \Phi(\mathbf{x}_{ij}) + 4\pi Q] K(\mathbf{x}_{ij}) + H(\mathbf{x}_{ij}),\end{aligned} \tag{3.108}$$

where w_{lm} and $\mathbf{x}_{lm}$, with $1 \leq l \leq N_x$ and $1 \leq m \leq N_y$, are the weights and nodes, respectively, of the two-dimensional quadrature scheme selected.

In order to simplify the notation, we define $k_{ijlm} = k_a(\mathbf{x}_{ij}, \mathbf{x}_{lm})$, $\Phi_{ij} = \Phi(\mathbf{x}_{ij})$, $K_{ij} = K(\mathbf{x}_{ij})$, and $H_{ij} = H(\mathbf{x}_{ij})$, which is the variable of the discrete problem. Thus, the linear system to solve is given by

$$\Phi_{ij} = \sigma_s \sum_{(k,l)\neq(i,j)} w_{lm} k_{ijlm} [\Phi_{lm} - \Phi_{ij}] + [\sigma_s \Phi_{ij} + 4\pi Q] K_{ij} + H_{ij}, \tag{3.109}$$

which has a large (of order $N_x^2 N_y^2$) coefficient matrix. Therefore, the best approach in this case is to solve it through the iterative approach, i.e., to use the Neumann series expansion (3.22) to construct the following iterative process:

$$\Phi_{ij} = \sum_{n=0}^{M} \sigma_s^n L_{ij}^n + \frac{\sigma_s^{M+1} \lambda_c}{1 - \sigma_s \lambda_c} L_{ij}^{M+1}, \tag{3.110}$$

where

$$L_{ij}^0 = 4\pi Q K_{ij} + H_{ij}, \tag{3.111}$$

$$L_{ij}^{n+1} = \sum_{(l,m)\neq(i,j)} w_{lm} [L_{lm}^n - L_{ij}^n] k_{ijlm} + L_{ij}^n \sigma_s K_{ij},\ n \geq 0, \tag{3.112}$$

and the dominant eigenvalue λ_c can be approximated by the Rayleigh quotient (see equation (3.67)).

The solution of linear system (3.109) by the presented iterative process provides the scalar flux at mesh points. However, the discretization can be adapted to compute the scalar flux at any point of the medium as follows:

$$G(\mathbf{x}) \approx \frac{\sigma_s \sum_{\mathbf{x}_{lm} \neq \mathbf{x}} w_{lm} k(\mathbf{x}, \mathbf{x}_{lm}) \Phi(\mathbf{x}) + 4\pi Q K(\mathbf{x}) + H(\mathbf{x})}{1 + \sigma_s \sum_{\mathbf{x}_{lm} \neq \mathbf{x}} w_{lm} k(\mathbf{x}, \mathbf{x}_{lm}) - \sigma_s K(\mathbf{x})}. \tag{3.113}$$

3.1.2.3 Test Problem

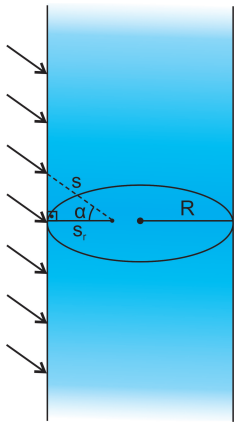

Figure 3.2: Domain illustration for the test problem with $\Omega_0 = (\cos(\alpha), 0, \sin(\alpha))$. $s_r = \sqrt{R^2 - r^2 \sin^2(\theta)} + r\cos(\theta)$.

Let's consider a collimated neutron flux ψ_b entering in the boundary at direction Ω_0, i.e.,

$$\Psi_b(\mathbf{x}, \Omega) = \psi_b \, \delta(\Omega - \Omega_0), \tag{3.114}$$

where δ is the Dirac delta distribution in S^2. Thus, we can write

$$\begin{aligned} H(\mathbf{x}) &= \int_{S^2} \Psi_b(\mathbf{x} - s\Omega) e^{-\sigma_t s} \, d\Omega \\ &= \int_{S^2} \psi_b \, \delta(\Omega - \Omega_0) e^{-\sigma_t s} \, d\Omega \\ &= \psi_b e^{-\sigma_t s(\mathbf{x}, \Omega_0)}. \end{aligned} \tag{3.115}$$

Without loss of generality, we consider $\Omega_0 = (\cos(\alpha), 0, \sin(\alpha))$ (see Figures 3.2 and 3.3), so that

$$H(\mathbf{x}) = \psi_b e^{-\frac{\sigma_t\left(\sqrt{R^2 - r^2\sin^2(\theta)} + r\cos(\theta)\right)}{\cos(\alpha)}}. \tag{3.116}$$

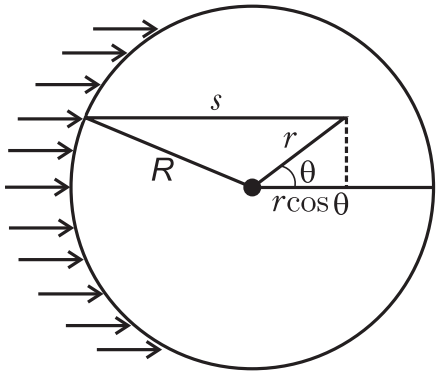

Figure 3.3: Right section of domain of for the test problem with $\alpha = 0$.

3.2 Three-dimensional Problem

Here, let's consider $\mathbf{x} \in D$, $D \subset \mathbb{R}^3$, with $\nabla\Psi(\mathbf{x}, \Omega) = \frac{\partial\Psi}{\partial x_1}\vec{i} + \frac{\partial\Psi}{\partial x_2}\vec{j} + \frac{\partial\Psi}{\partial x_3}\vec{k}$. The development in the present section has been published in the paper [24]. For more details, see the reference at https://doi.org/10.1016/j.jqsrt.2022.108087.

We begin with the equation (3.1a) and the boundary condition (3.1b). Considering that s is the distance along the particle trajectory, by taking

$$S(\mathbf{x} - s\Omega) = \frac{\sigma_s}{4\pi}\int_{S^2} \Psi(\mathbf{x}, \Omega')\, d\Omega' + Q \tag{3.117}$$

and applying the method of characteristics [78], the following representation of the scalar flux is obtained:

$$\Phi(\mathbf{x}) = \int_{S^2} \Psi(\mathbf{x}, \Omega)\, d\Omega = 4\pi\int_D S(\mathbf{y})k(\mathbf{x}, \mathbf{y})\, d\mathbf{y} + 4\pi\int_{\partial D} \Psi_b(\mathbf{y})k(\mathbf{x}, \mathbf{y})\, d\mathcal{S}, \tag{3.118}$$

where the kernel $k(\mathbf{x}, \mathbf{y})$ is given by

$$k(\mathbf{x}, \mathbf{y}) = \frac{e^{-\sigma_t |\mathbf{x}-\mathbf{y}|}}{4\pi |\mathbf{x}-\mathbf{y}|^2}. \tag{3.119}$$

3.2.1 Problem 3: Three-Dimensional axisymmetric case

Here, we consider the three-dimensional cylindrical domain $D = \{(x_1, x_2, x_3) : x_1^2 + x_2^2 \leq R^2, 0 \leq x_3 \leq L\}$. The axisymmetric case is considered. In Figure 3.4 is presented the illustration of the cylindrical medium. Then, equation (3.15) is used with the following boundary condition:

$$\Psi(\mathbf{r}, \Omega) = I_b(\mathbf{r}, \Omega) = \begin{cases} \Psi_{b1}(\mathbf{r}, \Omega), & \mathbf{n} \cdot \Omega < 0, \quad z = 0 \\ \Psi_{b2}(\mathbf{r}, \Omega), & \mathbf{n} \cdot \Omega < 0, \quad z = L \\ \Psi_{b3}(\mathbf{r}, \Omega), & \mathbf{n} \cdot \Omega < 0, \quad x^2 + y^2 = R^2. \end{cases} \tag{3.120}$$

By using cylindrical coordinates, the scalar flux (see equation (3.15)) can be written as

$$\begin{aligned} \Phi(\mathbf{x}) &= 4\pi \int_D S(\mathbf{y}) k(\mathbf{x}, \mathbf{y})\, d\mathbf{y} + 4\pi \int_{\partial D} \Psi_b(\mathbf{y}) k(\mathbf{x}, \mathbf{y})\, d\mathcal{S} \\ &= 4\pi \int_0^L \int_0^R \int_0^{2\pi} r' S(\mathbf{y}) k(\mathbf{x}, \mathbf{y})\, d\theta dr' dz' + 4\pi \int_0^R \int_0^{2\pi} \Psi_{b1}(\mathbf{y}) k(\mathbf{x}, \mathbf{y})\, d\theta dr' \\ &+ 4\pi \int_0^R \int_0^{2\pi} \Psi_{b2}(\mathbf{y}) k(\mathbf{x}, \mathbf{y})\, d\theta dr' + 4\pi \int_0^L \int_0^{2\pi} \Psi_{b3}(\mathbf{y}) k(\mathbf{x}, \mathbf{y})\, d\theta dz' \\ &= 4\pi \int_0^L \int_0^R S(r', z') \mathcal{K}_a(r, r', z, z')\, dr' dz' + \mathcal{K}_{b1}(r, z) + \mathcal{K}_{b2}(r, z) + \mathcal{K}_{b3}(r, z), \end{aligned} \tag{3.121}$$

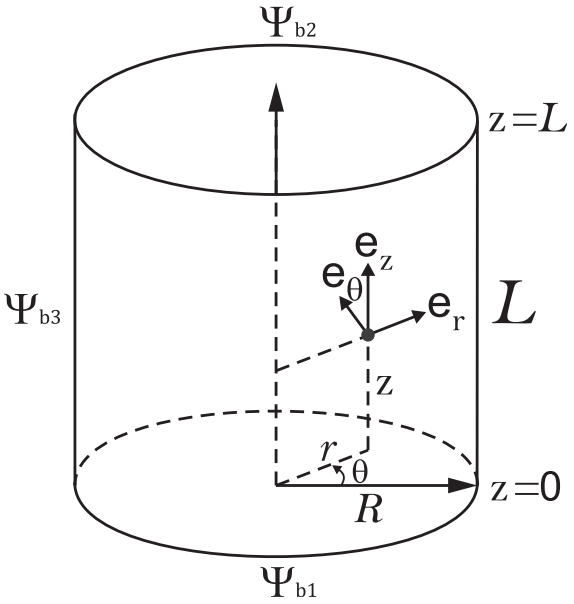

Figure 3.4: Illustration of the cylindrical medium with the system of coordinates.

where $\mathbf{x} = (x_1, x_2, x_3) = (r\cos(\theta), r\sin(\theta), z)$ and

$$\mathcal{K}_a(r, r', z, z') = \frac{1}{4\pi} \int_0^{2\pi} \frac{r' e^{-\sigma_t d(r',z')}}{d(r', z')^2}\, d\theta, \tag{3.122}$$

$$\mathcal{K}_{b1}(r, z) = \int_0^R \int_0^{2\pi} \Psi_{b1} \frac{r' z e^{-\sigma_t d(r',0)}}{d(r', 0)^3}\, d\theta dr', \tag{3.123}$$

$$\mathcal{K}_{b2}(r, z) = \int_0^R \int_0^{2\pi} \Psi_{b2} \frac{r'(L - z) e^{-\sigma_t d(r',L)}}{d(r', L)^3}\, d\theta dr', \tag{3.124}$$

$$\mathcal{K}_{b3}(r, z) = R \int_0^L \int_0^{2\pi} \Psi_{b3} \frac{(R - r\cos(\theta)) e^{-\sigma_t d(R,z')}}{d(R, z')^3}\, d\theta dz', \tag{3.125}$$

and

$$d(r', z') = \sqrt{r^2 - 2rr'\cos(\theta) + r'^2 + (z' - z)^2}. \tag{3.126}$$

The three last terms of equation (3.121) represent the boundary contributions. As a way to simplify the notation, we consider $B(\mathbf{x}) = B(r, z) = \mathcal{K}_{b1}(r, z) + \mathcal{K}_{b2}(r, z) + \mathcal{K}_{b3}(r, z)$ so that, by (3.5) and (3.121), the scalar flux is given

by

$$\begin{aligned}\Phi(r,z) = \sigma_s \int_0^L \int_0^R \Phi(r',z')\mathcal{K}_a(r,r',z,z')dr'dz' \\ + 4\pi Q \int_0^L \int_0^R \mathcal{K}_a(r,r',z,z')dr'dz' + B(r,z).\end{aligned} \tag{3.127}$$

In order to deal with the diagonal singularity ($\mathbf{y} = \mathbf{x}$), the technique of subtraction of singularity can be applied to the previous equation, which produces

$$\begin{aligned}\Phi(\mathbf{x}) = \sigma_s \int_0^L \int_0^R \left[\Phi(\mathbf{y}) - \Phi(\mathbf{x})\right] \mathcal{K}_a(\mathbf{x},\mathbf{y})dr'dz' + \left[\sigma_s \Phi(\mathbf{x}) + 4\pi Q\right] K(\mathbf{x}) \\ + B(\mathbf{x}),\end{aligned} \tag{3.128}$$

where

$$K(\mathbf{x}) = K(r,z) := \int_0^L \int_0^R \mathcal{K}_a(r,r',z,z')dr'dz'. \tag{3.129}$$

In favor to deal with the singularity of the term (3.122) to produce more precise results, it can be decomposed into a sum of three integrals, i.e., $\mathcal{K}_a(r,r',z,z') = \mathcal{K}_{a1}(r,r',z,z') + \mathcal{K}_{a2}(r,r',z,z') + \mathcal{K}_{a3}(r,r',z,z')$, where

$$\mathcal{K}_{a1}(r,r',z,z') := \frac{1}{4\pi} \int_0^{2\pi} \frac{(r'-r)\left(e^{-\sigma_t d(r',z')} - 1\right)}{d(r',z')^2}\, d\theta, \tag{3.130}$$

$$\mathcal{K}_{a2}(r,r',z,z') := \frac{1}{4\pi} \int_0^{2\pi} \frac{r\left(e^{-\sigma_t d(r',z')} - 1\right)}{d(r',z')^2}\, d\theta, \tag{3.131}$$

$$\mathcal{K}_{a3}(r,r',z,z') := \frac{1}{4\pi} \int_0^{2\pi} \frac{r'}{d(r',z')^2}\, d\theta. \tag{3.132}$$

The term $\mathcal{K}_{a3}$ may be analytically computed, producing

$$\mathcal{K}_{a3}(r,r',z,z') = \frac{r'}{2\sqrt{(r^2 + r'^2 + \mathtt{z}^2)^2 - 4r^2 r'^2}}. \tag{3.133}$$

where $\mathtt{z} = z' - z$.

We also note that, for $r' \neq 0$, the definition of $\mathcal{K}_a$ produces

$$\mathcal{K}_a(0,r',z,z') = \frac{1}{4\pi} \int_0^{2\pi} \frac{r' e^{-\sigma_t \sqrt{r'^2 + \mathtt{z}^2}}}{r'^2 + \mathtt{z}^2}\, d\theta = \frac{r' e^{-\sigma_t \sqrt{r'^2 + \mathtt{z}^2}}}{2\left(r'^2 + \mathtt{z}^2\right)} \tag{3.134}$$

and, for $r \neq 0$, results $\mathcal{K}_a(r, 0, z, z') = 0$. Moreover

$$\int_0^R \mathcal{K}_{a3}(r, r', z, z')dr' = \frac{1}{2}\ln\left(\frac{-r^2 + \mathtt{z}^2 + R^2 + \sqrt{(r^2 + R^2 + \mathtt{z}^2)^2 - 4r^2R^2}}{2\mathtt{z}^2}\right). \tag{3.135}$$

3.2.1.1 Computation of the current

From the definition of the current given in (3.3), it follows that:

$$\mathbf{J}(\mathbf{x}) = \int_D \Omega \frac{e^{-\sigma_t|\mathbf{x}-\mathbf{y}|}}{|\mathbf{x}-\mathbf{y}|^2} S(\mathbf{y})\, d\mathbf{y} + \int_{\partial D} \Omega \frac{e^{-\sigma_t|\mathbf{x}-\mathbf{y}|}}{|\mathbf{x}-\mathbf{y}|^2} \Psi_b(\mathbf{y})\, d\mathcal{S}. \tag{3.136}$$

Then, the radial and axial components of the current are given by

$$J_r(r, z) = \int_0^L \int_0^R K_r(r, r', z, z') S(r', z')\, dr' dz' + K_{b1}(r, z) \tag{3.137}$$

and

$$J_z(r, z) = \int_0^L \int_0^R K_z(r, r', z, z') S(r', z')\, dr' dz' + K_{b2}(r, z), \tag{3.138}$$

where

$$\begin{aligned} K_{b1}(r, z) = &\int_0^R z K_r(r, r', z, 0)\Psi_{b1}(\mathbf{y}) dr' \\ &+ \int_0^R (L - z) K_r(r, r', z, L)\Psi_{b2}(\mathbf{y}) dr' \\ + &\int_0^L (R - r\cos(\theta)) K_r(r, R, z, z')\Psi_{b3}(\mathbf{y}) dz', \end{aligned} \tag{3.139}$$

$$\begin{aligned} K_{b2}(r, z) = &\int_0^R z K_z(r, r', z, 0)\Psi_{b1}(\mathbf{y})\, dr' \\ &+ \int_0^R (L - z) K_z(r, r', z, L)\Psi_{b2}(\mathbf{y})\, dr' \\ + &\int_0^L (R - r\cos(\theta)) K_z(r, R, z, z')\Psi_{b3}(\mathbf{y})\, dz', \end{aligned} \tag{3.140}$$

$$K_r(r, r', z, z') = \int_0^{2\pi} \frac{r'(r - r'\cos(\theta))e^{-\sigma_t d(r', z')}}{d(r', z')^3} d\theta, \tag{3.141}$$

$$K_z(r,r',z,z') = \int_0^{2\pi} \frac{r'(z-z')e^{-\sigma_t d(r',z')}}{d(r',z')^3} d\theta. \tag{3.142}$$

Replacing the equation (3.5) in equations (3.137) and (3.138) and removing the singularity from both terms, the radial and axial components of the current can be written as, respectively,

$$\begin{aligned} J_r(r,z) = &\frac{\sigma_s}{4\pi} \int_0^L \int_0^R K_r(r,r',z,z') \left[\Phi(r',z') - \Phi(r,z)\right] dr'dz' \\ &+ \left[\frac{\sigma_s}{4\pi}\Phi(r,z) + Q\right] \int_0^L \int_0^R K_r(r,r',z,z')\, dr'dz' + K_{b1}(r,z), \end{aligned} \tag{3.143}$$

$$\begin{aligned} J_z(r,z) = &\frac{\sigma_s}{4\pi} \int_0^L \int_0^R K_z(r,r',z,z') \left[\Phi(r',z') - \Phi(r,z)\right] dr'dz' \\ &+ \left[\frac{\sigma_s}{4\pi}\Phi(r,z) + Q\right] \int_0^L \int_0^R K_z(r,r',z,z')\, dr'dz' + K_{b2}(r,z). \end{aligned} \tag{3.144}$$

Once more, the kernels of the integrals of both equations can be decomposed into the sum of multiple integrals. Such decompositions are important to produce high precision numerical results and are given by $K_r(r,r',z,z') = K_{r1}(r,r',z,z') + K_{r2}(r,r',z,z') + K_{r3}(r,r',z,z')$ and $K_z(r,r',z,z') = K_{z1}(r,r',z,z') + K_{z2}(r,r',z,z') + K_{z3}(r,r',z,z')$, where

$$K_{r1}(r,r',z,z') := 2\int_0^\pi \frac{(r'-r)(r-r'\cos(\theta))e^{-\sigma_t d(r',z')}}{d(r',z')^3} d\theta, \tag{3.145}$$

$$K_{r2}(r,r',z,z') := 2\int_0^\pi \frac{r(r-r'\cos(\theta))\left(e^{-\sigma_t d(r',z')} - 1\right)}{d(r',z')^3} d\theta, \tag{3.146}$$

$$K_{r3}(r,r',z,z') := 2\int_0^\pi \frac{r(r-r'\cos(\theta))}{d(r',z')^3} d\theta, \tag{3.147}$$

$$K_{z1}(r,r',z,z') := 2\int_0^\pi \frac{(r'-r)(z-z')e^{-\sigma_t d(r',z')}}{d(r',z')^3} d\theta, \tag{3.148}$$

$$K_{z2}(r,r',z,z') := 2\int_0^\pi \frac{r(z-z')\left(e^{-\sigma_t d(r',z')} - 1\right)}{d(r',z')^3} d\theta, \tag{3.149}$$

$$K_{z3}(r,r',z,z') := 2\int_0^\pi \frac{r(z-z')}{d(r',z')^3} d\theta. \tag{3.150}$$

We define

$$U_{r3}(r,z) = \int_0^L \int_0^R K_{r3} dr'dz' \quad \text{and} \quad U_{z3}(r,z) = \int_0^L \int_0^R K_{z3} dr'dz' \tag{3.151}$$

In the case of triple integral $U_{z3}(r,z)$, due to mathematical properties of the integrand, the integration limits in the variable z can be changed. For $z < L/2$, it follows that

$$U_{z3}(r,z) = \int_{2z}^{L}\int_{0}^{R} K_{z3}dr'dz', \tag{3.152}$$

while for $z > L/2$ results

$$U_{z3}(r,z) = \int_{0}^{2z-L}\int_{0}^{R} K_{z3}dr'dz', \tag{3.153}$$

Then, for the case $0 < z < L$, $U_{z3}(r,z)$ is no longer singular. For the case $z = 0$, it can be noted that

$$\begin{aligned} U_{z3}(r,0) &= 2\int_{0}^{L}\int_{0}^{R}\int_{0}^{\pi} \frac{r(-z')}{(r^2 - 2rr'\cos(\theta) + r'^2 + z'^2)^{3/2}}d\theta dr'dz' \\ &= 2\int_{0}^{R}\int_{0}^{\pi} \frac{r}{\sqrt{r^2 - 2rr'\cos(\theta) + r'^2 + L^2}}d\theta dr' \\ &+ \int_{0}^{R}\int_{0}^{\pi} \frac{2(r'-r)}{\sqrt{r^2 - 2rr'\cos(\theta) + r'^2}}d\theta dr' - M(r) \end{aligned} \tag{3.154}$$

The first integral in the last equality is not singular and the second has a well comported integrand and is easy to evaluate numerically. The remainder $M(r)$ is given by

$$M(r) = \int_{0}^{R}\int_{0}^{\pi} \frac{2r'}{\sqrt{r^2 - 2rr'\cos(\theta) + r'^2}}d\theta dr' \tag{3.155}$$

For the integral in the θ variable it can be noted that

$$\begin{aligned} \int_{0}^{\pi} \frac{2r'}{\sqrt{r^2 - 2rr'\cos(\theta) + r'^2}}d\theta &= \frac{4r'}{r+r'}\int_{0}^{\frac{\pi}{2}} \frac{1}{\sqrt{1 - \frac{4rr'}{(r+r')^2}\sin^2(\theta)}}d\theta \\ &= \frac{4r'}{r+r'}\mathrm{K}\left(\frac{2\sqrt{rr'}}{r+r'}\right). \end{aligned} \tag{3.156}$$

By using equations 3.44, 3.47, and 3.48 [54] it follows that

$$\begin{aligned}
M(r) &= \int_0^R \frac{4r'}{r+r'}\mathrm{K}\left(\frac{2\sqrt{rr'}}{r+r'}\right) \\
&= \int_0^r \frac{4r'}{r+r'}\mathrm{K}\left(\frac{2\sqrt{rr'}}{r+r'}\right) dr' + \int_r^R \frac{4r'}{r+r'}\mathrm{K}\left(\frac{2\sqrt{rr'}}{r+r'}\right) dr' \\
&= \int_0^1 \frac{4tr}{t+1}\mathrm{K}\left(\frac{2\sqrt{t}}{1+t}\right) dt + \int_1^{\frac{r}{R}} \frac{-4r}{t^2(t+1)}\mathrm{K}\left(\frac{2\sqrt{t}}{1+t}\right) dt \\
&= \int_0^1 4r\mathrm{K}\left(tr\right) dt + \int_1^{\frac{r}{R}} \frac{-4r}{t^2}\mathrm{K}\left(t\right) dt \\
&= 4r\left[(\mathrm{E}(1) - \mathrm{E}(0) + \mathrm{K}(0)) + \left(\frac{R}{r}\mathrm{E}\left(\frac{r}{R}\right) - \mathrm{E}(1)\right)\right] \\
&= 4r\left(-\mathrm{E}(0) + \mathrm{K}(0) + \frac{R}{r}\mathrm{E}\left(\frac{r}{R}\right)\right) \\
&= 4R\mathrm{E}\left(\frac{r}{R}\right).
\end{aligned} \tag{3.157}$$

Furthermore, for the integral U_{z3}, we note that some computations can be accelerated because $U_{z3}(r, L/2) = 0$ and $U_{z3}(r, L) = -U_{z3}(r, 0)$.

3.2.1.2 Collimated neutron beam normal to the surface $z = 0$

We consider a finite cylinder exposed to normal collimated neutron flux ψ_b on the surface $z = 0$, so that

$$\Psi_b(\mathbf{x}, \Omega) = \psi_b\, \delta(\Omega - \Omega_0), \tag{3.158}$$

where δ is the Dirac delta distribution in S^2 and $\Omega_0 = (0, 0, 1)$. Thus, it follows that

$$B(\mathbf{x}) = \int_{S^2} \psi_b\, \delta(\Omega - \Omega_0) e^{-\sigma_t s}\, d\Omega = \psi_b e^{-\sigma_t s(\mathbf{x}, \Omega_0)} = \psi_b e^{-\sigma_t z}, \tag{3.159}$$

that is, $\mathcal{K}_{b1}(r, z) = \psi_b e^{-\sigma_t z}$, $\mathcal{K}_{b2}(r, z) = 0$ and $\mathcal{K}_{b3}(r, z) = 0$.

Moreover,

$$\int_{S^2} \Omega\psi_b\, \delta(\Omega - \Omega_0) e^{-\sigma_t s}\, d\Omega = \psi_b \Omega_0 e^{-\sigma_t s(\mathbf{x}, \Omega_0)} = \psi_b \Omega_0 e^{-\sigma_t z}, \tag{3.160}$$

so that $K_{b1}(r, z) = 0$ and $K_{b2}(r, z) = \psi_b e^{-\sigma_t z}$.

3.2.1.3 Numerical implementation

In order to deal with the problem numerically, the Nyström method can be applied to the equation (3.128) to discretize the integral operator involved, obtaining the following expression for the quadrature points $\mathbf{x}_{ij} = (r_i, z_j)$:

$$\begin{aligned}\Phi(\mathbf{x}_{ij}) \approx \sigma_s \sum_{(l,m)\neq(i,j)} w_{lm}\mathcal{K}_a(\mathbf{x}_{ij}, \mathbf{x}_{lm})\left[\Phi(\mathbf{x}_{lm}) - \Phi(\mathbf{x}_{ij})\right] \\ +[\sigma_s\Phi(\mathbf{x}_{ij}) + 4\pi Q]K(\mathbf{x}_{ij}) + B(\mathbf{x}_{ij}),\end{aligned} \tag{3.161}$$

where w_{lm} and $\mathbf{x}_{lm}$, with $1 \leq l \leq N_r$ and $1 \leq m \leq N_z$, are the weights and nodes, respectively, of the two-dimensional quadrature scheme selected.

In order to simplify the notation, define $k_{ijlm} = \mathcal{K}_a(\mathbf{x}_{ij}, \mathbf{x}_{lm})$, $K_{ij} = K(\mathbf{x}_{ij})$, $B_{ij} = B(\mathbf{x}_{ij})$, and the variable of the discrete problem $\Phi_{ij} = \Phi(\mathbf{x}_{ij})$. Thus, the linear system to be solved is given by

$$\Phi_{ij} = \sigma_s \sum_{(l,m)\neq(i,j)} w_{lm}k_{ijlm}[\Phi_{lm} - \Phi_{ij}] + [\sigma_s\Phi_{ij} + 4\pi Q]K_{ij} + B_{ij}, \tag{3.162}$$

which has a large coefficient matrix (of order $N_r^2 N_z^2$). Therefore, the best approach in this case is to solve it through an iterative approach, for instance, the Neumann series expansion (3.22). Such approach creates the following iterative process:

$$\Phi_{ij} = \sum_{n=0}^{M} \sigma_s^n L_{ij}^n + \frac{\sigma_s^{M+1}\lambda_c}{1 - \sigma_s\lambda_c} L_{ij}^{M+1}, \tag{3.163}$$

where

$$L_{ij}^0 = 4\pi Q + B_{ij}, \tag{3.164}$$

$$L_{ij}^{n+1} = \sum_{(l,m)\neq(i,j)} w_{lm}[L_{lm}^n - L_{ij}^n]k_{ijlm} + L_{ij}^n K_{ij},\ n \geq 0, \tag{3.165}$$

and the dominant eigenvalue λ_c can be approximated by the Rayleigh quotient (see equation (3.67)).

The solution of linear system (3.162) by the presented iterative process provides the scalar flux at mesh points. However, the discretization can be adapted

to compute the scalar flux at any point of the medium as follows:

$$\Phi(\mathbf{x}) \approx \frac{\sigma_s \sum_{\mathbf{x}_{lm} \neq \mathbf{x}} w_{lm} k(\mathbf{x}, \mathbf{x}_{lm}) \Phi(\mathbf{x}) + 4\pi Q + B(\mathbf{x})}{1 + \sigma_s \sum_{\mathbf{x}_{lm} \neq \mathbf{x}} w_{lm} k(\mathbf{x}, \mathbf{x}_{lm}) - \sigma_s K(\mathbf{x})}. \tag{3.166}$$

To compute the approximations to the components of the current, it is necessary numerically compute the boundary contributions K_{b1} and K_{b2}, the multiple integrals of the kernels K_r and K_z that appear in equations (3.143) and (3.144). Finally, (3.143) and (3.144) are used to provide axial and radial components the of current, respectively, after the first integral in each one of these equations is approximated by the quadrature scheme selected.

4 RESULTS

The obtainment of our numerical results is based on the application of the Nyström method with the singularity-subtraction strategy for the integral formulation of the transport equation. For that, the following sequence of steps was considered:

1. Computation of the necessary integrals, such as kernels and boundary contributions;

2. Use of the iterative process based on Neumann series to compute the scalar flux at mesh points;

3. Applying the quadrature scheme selected in the appropriate equations to compute the current from the previously computed scalar flux.

In step 2, if we want to compute the scalar flux at points out of the mesh an interpolation formula is used. For Problem 1, the scalar flux at mesh points can be alternatively obtained by the numerical solution of the linear system (3.63).

4.1 Computational Details

All algorithms we have used to generate the numerical results were implemented in C and C++ programming language. We use the GNU Scientific Library Free Software Foundation [45] to solve the Problems 1 and 2. For the Problem 3, we combine the use of GSL with the Cubature Library [1], a code for adaptive multidimensional integration of vector-valued integrands via the Genz-Malik algorithm designed by the Ab-Initio Physics Research Group at Massachusetts Institute of Technology. Also, parallelization with OpenMP [76] was used in order

to accelerate the computation and tabulation of the kernels in step 1 for Problems 2 and 3.

For Problems 1 and 2 the numerical integrals computed with the adaptive Gauss-Kronrod 21-point integration rule (QAGS or QAGP) from GSL. In the case of Problem 3, the use of adaptive Gauss-Kronrod 21-point integration rule of GSL is important to deal with singularities in the integration region and ensure precision whereas the adaptive multidimensional integration with Genz-Malik algorithm of Cubature is used to speed up the computations of multiple integrals whose singularity is not very strong. The hybrid approach with libraries allowed to obtain high quality results with reduced computational times.

In numerical integration, the use of adaptive routines in presence of an integrable singularity in the integration region causes the concentration of new subintervals around the singularity. As these subintervals decrease in size the successive approximations to the integral converge in a limiting fashion [45]. The QAGS algorithm combines adaptive bisection with the Wynn epsilon-algorithm to accelerate the integration of many types of integrable singularities and QAGP routine applies the adaptive integration algorithm QAGS taking account of the user-supplied locations of singular points. The relative error limits used in Problems 1 and 2 were 10^{-9}, 10^{-8} and 10^{-8} for first, second and third integration, respectively, in the case of $R \leq 1$. For $R > 1$ all integration tolerances have been chosen to obtain relative errors less than 10^{-9}. For Problem 3 all integration tolerances have been chosen to obtain relative errors less than 10^{-7}. However, for the same problem, to generate the data needed to build the graphics, the tolerance in the third integration for GSL routines was taken as 10^{-5} to speed up the process.

For the numerical computation of complete elliptic integrals several approaches are available (see [46]). An example is the use of expansion series. Here, we tested GSL routines (based on duplication theorem), Chebyshev approximations

of the Hastings form [30] and truncations of Taylor series expansions of the integrals proposed by Fukushima [46]. The latter was more effective in our numerical tests.

The Bickley-Naylor functions are tabulated in one dimensional tables after removing the singularities [36, 88]. To improve the accuracy, removal is done only near to the singularity point. Furthermore, a quadratic interpolation is used to speed up obtaining the numerical results for the Bickley-Naylor functions.

In the case of the non-iterative approach for the Problem 1, the linear system (3.63) is numerically solved by Gaussian elimination with partial pivoting as implemented in GSL, using gsl_linalg_LU_decomp and gsl_linalg_LU_solve algorithms. For critical value determination, the algorithm of computing eigenvalues used was the QR double-shift Francis method [53] implemented in GSL routine named gsl_eigen_nonsymmv.

4.2 Problem 1

In this section an overview of the results reported in the work [23], which is available at https://doi.org/10.1016/j.anucene.2020.107701, is presented. Some results are revisited and new or updated results are presented. The iterative process (3.64) had not been proposed in [23] and was used in this work to produce equally accurate results more quickly.

For the purposes of validation of our code, we compare the results of the numerical integrals (when possible) with the values obtained by the numerical quadrature internal routines of the Maple 15 software [75] or by online tool Wolfram|Alpha [58]. A test problem, with $\Psi_b(r) = 1$, $Q = 0.5$, $\sigma_s = 0.5$ and $\sigma_t = 1$ produced the desired constant scalar flux $\Phi(r) = 1$ and constant current $J(r) = 0$ (see equations (4.1) and (4.2)).

We compare the numerical results obtained for the flux and current profiles with those presented in the literature by Altaç [8], Siewert and Thomas Jr. [94], and Ganapol [47,48]. For such comparison, in the present study we consider total macroscopic cross section (σ_t) equal to 1 cm^{-1} and cylinders of radii 1 and 10 cm. Constant boundary condition (measured in $cm^{-2}sr^{-1}s^{-1}$) and source (measured in $cm^{-3}s^{-1}$) are taken. Units of Ψ, Φ, σ_s, and σ_c are, respectively, $cm^{-2}sr^{-1}s^{-1}$, $cm^{-2}s^{-1}$, cm^{-1}, and cm^{-1}. For critical value determination, several values for R are used.

In the research of Siewert and Thomas Jr. [94] an integral transformation technique and the F_N method are used to solve a neutron transport problem for an infinite bare cylinder with constant boundary condition $\Psi_b(r) = \Psi_b$. In that work, the authors provided numerical results for the surrogate flux $P(r)$ for a problem with constant source term Q. In this case, scalar flux is given by

$$\Phi(r) = \frac{Q}{1-c} - \left(\frac{Q}{1-c} - \Psi_b\right) P(r), \tag{4.1}$$

where c is the mean number of secondary neutrons produced per collision and $P(r)$ is independent of Q and Ψ_b. Also in that work, under equal conditions, the authors provided numerical results for the function $C(r)$, which is related to the current by equation

$$J(r) = \left(\frac{Q}{1-c} - \Psi_b\right) C(r), \tag{4.2}$$

with $C(r)$ independent of Q and Ψ_b.

In 2007 and 2008, Ganapol [47,48] used a new formulation of F_N method and found nearly complete agreement with results of Siewert and Thomas Jr. [94] in a head-to-head comparison with the $P(r)$ of benchmark for cylinders of radii 1 and 10. In such works, Ganapol extended the numerical results for the case of vacuum boundary condition, providing the surrogate flux for several values of c.

The Tables 4.1, 4.2, and 4.3 present the results for the surrogate flux $P(r)$, determined with equation (4.1) from the previously computed scalar flux, for

$R = 1$ and $N = 4001$. The absolute error for the present results is expected to be less than 3×10^{-8}. In [23] it was shown that $N = 1001$ is sufficient to obtain a complete agreement in a head-to-head comparison with the benchmarks of six decimal places computed by Siewert and Thomas Jr. [94] and by Ganapol [47, 48]. With a mesh of $N = 401$, few values remain different from the benchmarks, which have only a difference of one unit in the last decimal place (see [23] for more details). The Tables 4.1-4.3 also include the results for cases $c = 0.35$, 0.45, 0.55, 0.65, 0.75, 0.85, 0.95, which are not available in [47, 48, 94].

Table 4.1: Surrogate flux $P(r)$ for $R = 1$, $\Psi_b(r) = 0$ and $N = 4001$.

r	$c = 0.1$	$c = 0.15$	$c = 0.2$	$c = 0.25$	$c = 0.3$	$c = 0.35$
0.0	0.29925565	0.31361712	0.32916525	0.34604043	0.36440518	0.38444854
0.1	0.30116269	0.31553343	0.33108731	0.34796405	0.36632530	0.38635909
0.2	0.30696552	0.32136170	0.33693030	0.35380888	0.37215655	0.39215831
0.3	0.31692038	0.33135068	0.34693475	0.36380653	0.38212084	0.40205755
0.4	0.33149512	0.34595412	0.36153906	0.37837874	0.39662188	0.41644106
0.5	0.35144655	0.36590494	0.38145041	0.39820495	0.41630925	0.43592641
0.6	0.37797376	0.39236240	0.40778542	0.42435627	0.44220556	0.46148451
0.7	0.41304366	0.42722423	0.44236865	0.45857984	0.47597613	0.49469425
0.8	0.46019669	0.47389947	0.48847149	0.50400291	0.52059723	0.53837394
0.9	0.52724144	0.53989370	0.55328527	0.56749083	0.58259601	0.59869954
1.0	0.65289475	0.66241146	0.67245910	0.68309118	0.69436904	0.70636344

Table 4.2: Surrogate flux $P(r)$ for $R = 1$, $\Psi_b(r) = 0$ and $N = 4001$.

r	$c = 0.4$	$c = 0.45$	$c = 0.5$	$c = 0.55$	$c = 0.6$	$c = 0.65$
0.0	0.40639161	0.43049457	0.45706547	0.48647164	0.51915442	0.55564847
0.1	0.40828532	0.43236269	0.45889747	0.48825483	0.52087344	0.55728467
0.2	0.41403038	0.43802706	0.46444929	0.49365570	0.52607696	0.56223456
0.3	0.42382676	0.44767537	0.47389536	0.50283448	0.53491007	0.57062716
0.4	0.43803772	0.46164830	0.48755221	0.51608190	0.54763600	0.58269653
0.5	0.45724652	0.48049247	0.50592735	0.53386385	0.56467652	0.59881780
0.6	0.48236909	0.50506541	0.52981641	0.55691046	0.58669261	0.61957916
0.7	0.51489317	0.53675874	0.56050978	0.58640567	0.61475640	0.64593552
0.8	0.55747168	0.57805238	0.60030643	0.62445927	0.65077995	0.67959239
0.9	0.61591592	0.63437869	0.65424475	0.67569970	0.69896490	0.72430662
1.0	0.71915642	0.73284372	0.74753781	0.76337177	0.78050431	0.79912640

The results for the function $C(r)$ for several values of c in the case $R = 1$ are available in Tables 4.4, 4.5, and 4.6. We expect the error in our results to be less

Table 4.3: Surrogate flux $P(r)$ for $R = 1$, $\Psi_b(r) = 0$ and $N = 4001$.

r	$c = 0.7$	$c = 0.75$	$c = 0.8$	$c = 0.85$	$c = 0.9$	$c = 0.95$
0.0	0.59660746	0.64283871	0.69535050	0.75541811	0.82467744	0.90526098
0.1	0.59813808	0.64423582	0.69657964	0.75643639	0.82543104	0.90568161
0.2	0.59813808	0.64845727	0.70029121	0.75950926	0.82770367	0.90694927
0.3	0.61060255	0.65559724	0.70656082	0.76469324	0.83153253	0.90908208
0.4	0.62185170	0.66582675	0.71552595	0.77209129	0.83698563	0.91211337
0.5	0.63683930	0.67942049	0.72740790	0.78186973	0.84417332	0.91609754
0.6	0.65607714	0.69681047	0.74255572	0.79429196	0.85327145	0.92112210
0.7	0.68039749	0.71870095	0.76154056	0.80979133	0.86457145	0.92733349
0.8	0.71129025	0.74635697	0.78539316	0.82915472	0.87860693	0.93500287
0.9	0.75204821	0.78258652	0.81641429	0.85415127	0.89658850	0.94475238
1.0	0.81946998	0.84181971	0.86652911	0.89404286	0.92492862	0.95992299

than 3×10^{-8}. In [23] it was shown that $N = 601$ is sufficient to obtain a complete agreement, for the cases $c = 0.3$, $c = 0.5$, $c = 0.7$, $c = 0.9$, in a head-to-head comparison with the benchmarks of six significant digits computed by Siewert and Thomas Jr. [94] (see [23] for more details). For the cases $c = 0.1$, $c = 0.15$, $c = 0.2$, $c = 0.25$, it is sufficient to use a mesh of $N = 401$ to obtain complete agreement with benchmark results presented in [48]. The Tables 4.4-4.6 include the results for the cases $c = 0.35$, 0.45, 0.55, 0.65, 0.75, 0.85, 0.95, which are not available in the literature.

Table 4.4: $C(r)$ function for $R = 1$, $\Psi_b(r) = 0$ and $N = 4001$.

r	$c = 0.1$	$c = 0.15$	$c = 0.2$	$c = 0.25$	$c = 0.3$	$c = 0.35$
0.0	0.00000000	0.00000000	0.00000000	0.00000000	0.00000000	0.00000000
0.1	0.01350936	0.01336940	0.01320501	0.01301255	0.01278775	0.01252559
0.2	0.02727831	0.02698509	0.02664245	0.02624311	0.02577855	0.02523874
0.3	0.04157899	0.04110488	0.04055524	0.03991918	0.03918393	0.03833449
0.4	0.05671052	0.05601128	0.05520878	0.05428852	0.05323354	0.05202391
0.5	0.07301780	0.07202871	0.07090654	0.06963322	0.06818764	0.06654512
0.6	0.09091918	0.08954871	0.08801288	0.08629013	0.08435538	0.08217934
0.7	0.11095251	0.10907176	0.10699080	0.10468474	0.10212476	0.09927726
0.8	0.13386380	0.13128781	0.12847453	0.12539608	0.12202023	0.11830959
0.9	0.16082193	0.15727087	0.15344480	0.14931337	0.14484160	0.13998901
1.0	0.19433604	0.18931092	0.18397847	0.17830675	0.17225913	0.16579325

As discussed above, excellent results are obtained for $R = 1$ in the case of vacuum boundary condition. In the paper [23], results for the functions $P(r)$ and

Table 4.5: $C(r)$ function for $R = 1$, $\Psi_b(r) = 0$ and $N = 4001$.

r	$c = 0.4$	$c = 0.45$	$c = 0.5$	$c = 0.55$	$c = 0.6$	$c = 0.65$
0.0	0.00000000	0.00000000	0.00000000	0.00000000	0.00000000	0.00000000
0.1	0.01222013	0.01186426	0.01144952	0.01096566	0.01040027	0.00973816
0.2	0.02461180	0.02388361	0.02303725	0.02205235	0.02090421	0.01956263
0.3	0.03735312	0.03621874	0.03490615	0.03338505	0.03161869	0.02956221
0.4	0.05063615	0.04904239	0.04720937	0.04509713	0.04265730	0.03983094
0.5	0.06467658	0.06254759	0.06011715	0.05733610	0.05414505	0.05047172
0.6	0.07972762	0.07695957	0.07382693	0.07027194	0.06622499	0.06160152
0.7	0.09610292	0.09255542	0.08857986	0.08411073	0.07906925	0.07335996
0.8	0.11422049	0.10970165	0.10469245	0.09912076	0.09290006	0.08592572
0.9	0.13470848	0.12894483	0.12263300	0.11569579	0.10804079	0.09955655
1.0	0.15885997	0.15140184	0.14335131	0.13462834	0.12513735	0.11476325

Table 4.6: $C(r)$ function for $R = 1$, $\Psi_b(r) = 0$ and $N = 4001$.

r	$c = 0.7$	$c = 0.75$	$c = 0.8$	$c = 0.85$	$c = 0.9$	$c = 0.95$
0.0	0.00000000	0.00000000	0.00000000	0.00000000	0.00000000	0.00000000
0.1	0.00896058	0.00804421	0.00695965	0.00566945	0.00412527	0.00226368
0.2	0.01799036	0.01614103	0.01395631	0.01136189	0.00826188	0.00453052
0.3	0.02716035	0.02434436	0.02102782	0.01710078	0.01242137	0.00680374
0.4	0.03654549	0.03271083	0.02821380	0.02291055	0.01661571	0.00908665
0.5	0.04622732	0.04130171	0.03555681	0.02881732	0.02085763	0.01138275
0.6	0.05629786	0.05018564	0.04310420	0.03484990	0.02516102	0.01369585
0.7	0.06686604	0.05944317	0.05091103	0.04104148	0.02954177	0.01603023
0.8	0.07807002	0.06917550	0.05904581	0.04743293	0.03401921	0.01839105
0.9	0.09010728	0.07952593	0.06760455	0.05408096	0.03861986	0.02078532
1.0	0.10336607	0.09077387	0.07677297	0.06109430	0.04339417	0.02322624

$C(r)$ for a problem with a boundary condition $\Psi_b(r) = 1$, source term $Q = 1$ and $c = 0.5$ were presented. Complete agreement (up to the sixth significant digit) is noted to functions $P(r)$ and $C(r)$ when compared with benchmark results of Siewert and Thomas Jr. [94]. Furthermore, for the same conditions, contour lines for scalar flux and vector field of the current were presented in [23]. Here, we add in Tables 4.7 and 4.8 the results of scalar flux and current for the same problem. The results in these tables show that convergence also behaves well for problems with a constant boundary condition. Also, for completeness we include in Figures 4.1-4.2 the contour lines of the scalar flux and vector field of the current for different problems.

Table 4.7: Convergence of scalar flux $\Phi(r)$ computed with Boole's rule for $R = 1$, $\Psi_b(r) = 1$, $\sigma_t = 1$, $\sigma_s = 0.5$, $Q = 1$.

r	$N = 101$	$N = 201$	$N = 401$	$N = 801$	$N = 1601$	$N = 3201$
0.0	1.54293397	1.54293439	1.54293450	1.54293452	1.54293453	1.54293453
0.1	1.54110194	1.54110239	1.54110249	1.54110252	1.54110253	1.54110253
0.2	1.53555013	1.53555057	1.53555068	1.53555070	1.53555071	1.53555071
0.3	1.52610403	1.52610449	1.52610461	1.52610463	1.52610464	1.52610464
0.4	1.51244716	1.51244763	1.51244775	1.51244778	1.51244779	1.51244779
0.5	1.49407196	1.49407248	1.49407261	1.49407264	1.49407265	1.49407265
0.6	1.47018286	1.47018341	1.47018355	1.47018358	1.47018359	1.47018359
0.7	1.43948938	1.43949002	1.43949017	1.43949021	1.43949022	1.43949022
0.8	1.39969261	1.39969333	1.39969351	1.39969355	1.39969356	1.39969357
0.9	1.34575397	1.34575495	1.34575517	1.34575523	1.34575525	1.34575525
1.0	1.25245572	1.25246041	1.25246170	1.25246206	1.25246216	1.25246218

Table 4.8: Convergence of current $J(r)$ computed with Boole's rule for $R = 1$, $\Psi_b(r) = 1$, $\sigma_t = 1$, $\sigma_s = 0.5$, $Q = 1$.

r	$N = 101$	$N = 201$	$N = 401$	$N = 801$	$N = 1601$	$N = 3201$
0.0	0.00000000	0.00000000	0.00000000	0.00000000	0.00000000	0.00000000
0.1	0.14388006	0.14387893	0.14387889	0.14387888	0.14387888	0.14387888
0.2	0.28949493	0.28949466	0.28949460	0.28949458	0.28949458	0.28949458
0.3	0.43864736	0.43864380	0.43864370	0.43864367	0.43864367	0.43864367
0.4	0.59325120	0.59325065	0.59325051	0.59325048	0.59325047	0.59325047
0.5	0.75546112	0.75545464	0.75545446	0.75545441	0.75545440	0.75545440
0.6	0.92773771	0.92773683	0.92773661	0.92773655	0.92773654	0.92773653
0.7	1.11313837	1.11312772	1.11312745	1.11312737	1.11312736	1.11312735
0.8	1.31560594	1.31560462	1.31560428	1.31560419	1.31560417	1.31560417
0.9	1.54107170	1.54105232	1.54105190	1.54105180	1.54105177	1.54105177
1.0	1.80139648	1.80140343	1.80140516	1.80140558	1.80140569	1.80140572

As shown in [23], for the case $R = 10$ a larger N is needed ($N = 4001$) to obtain a greater agreement with benchmark results of Siewert and Thomas Jr. [94] and Ganapol [47]. For $R = 10$, the results obtained to $P(r)$ are in Tables 4.9 and 4.10. The values of surrogate flux presented in [94] and [47] for $c = 0.5$, 0.9 are the same. For $c = 0.3$, Ganapol results of $P(1)$ and $P(10)$ are one unit smaller in the last digit, which also occurs with the value of $P(10)$ for $c = 0.7$. The highlighted value in the Table 4.9 is the only one that is discrepant with respect to Siewert and Thomas Jr. [94] results, but it coincides with that presented in [47].

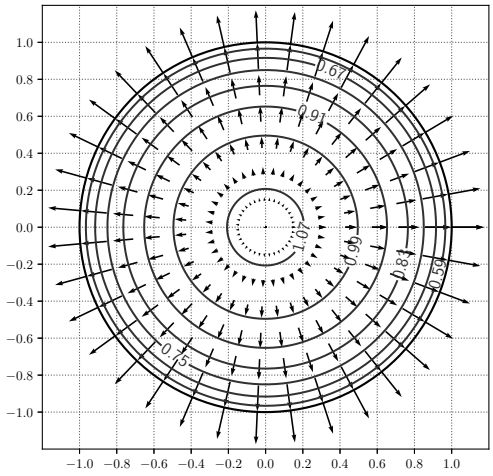

Figure 4.1: Contour lines of the scalar flux and vector field of the current for the Problem 1 with $R = 1$, $\sigma_s = 0.5$, $Q = 1$, $\Psi_b = 0$.

The highlighted values in the Table 4.10 are in disagreement with those presented by Ganapol [47]. The discrepant values are just one unit smaller in the last digit if compared with benchmarks. We note that the discrepancy of a single digit is irrelevant since results are within the quoted accuracy of the published benchmark ($\pm$ one digit in the last place). With the use of Boole's rule two additional values appear one unit larger in the last decimal place (see [23] for more details).

Table 4.9: Surrogate flux $P(r)$ for $R = 10$, $\Psi_b(r) = 0$ and $N = 4001$.

r	$c = 0.3$	$c = 0.5$	$c = 0.7$	$c = 0.9$
0	0.460882e-4	0.138859e-3	0.801829e-3	0.201898e-1
1	0.595324e-4	0.173680e-3	0.946293e-3	0.216079e-1
2	0.112121e-3	0.305085e-3	0.145897e-2	0.261624e-1
3	0.253579e-3	0.637744e-3	0.262685e-2	0.348252e-1
4	0.625301e-3	0.144881e-2	0.512494e-2	0.494721e-1
5	0.162250e-2	0.344884e-2	0.104520e-1	0.733358e-1
6	0.437880e-2	0.848704e-2	0.219360e-1	0.111811e-0
7	0.122887e-1	0.215284e-1	0.471009e-1	0.173872e-0
8	0.362559e-1	0.566444e-1	0.103616e-0	0.274762e-0
9	0.116748e-0	0.158763e-0	0.237138e-0	0.442664e-0
10	0.558361e-0	0.600996e-0	0.663331e-0	0.781243e-0

The highlighted value 0.595324e-4 $= 0.595324 \times 10^{-4}$ is the only one that is discrepant with respect to results presented in [94], but it is in agreement with that presented by Ganapol [47].

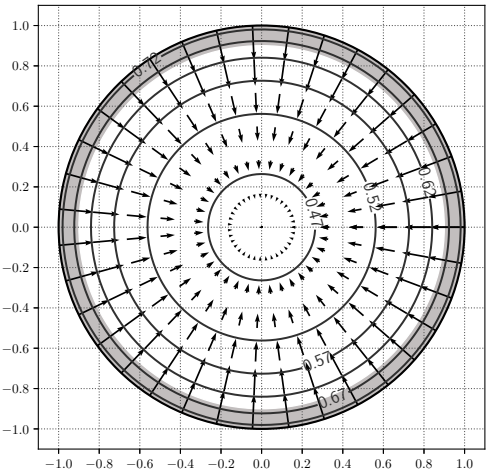

Figure 4.2: Contour lines of the scalar flux and vector field of the current for the Problem 1 with $R = 1$, $\sigma_s = 0.5$, $Q = 0$, $\Psi_b = 1$.

As shown in [23], if $R = 10$, for the cases $c = 0.3, 0.5, 0.7, 0.9$ a mesh of $N = 4001$ is needed to obtain complete agreement with benchmark results of Siewert and Thomas Jr. [94] for the function $C(r)$. We note that, with a mesh of $N = 2501$, the few discrepant values appear one unit greater in the last digit (see [23] for more details). For the cases $c = 0.1, 0.15, 0.2, 0.25$, we obtain complete agreement with benchmark results of Ganapol [48] with $N = 4001$. The results computed in the present research are given in Tables 4.11 and 4.12.

As noted above, our methodology also produces excellent results for the case $R = 10$. It can be noted that since the radius of the cylinder has been increased tenfold, the necessary increase in mesh size is acceptable. For the cases $R = 1$ and $R = 10$, scalar flux profiles for several values of σ_s are given in [23]. The curves of the scalar flux are smooth (see [23]), which shows that the ray effect does not appear or, at least, is irrelevant in the integral formulation used in this work to solve the transport problem.

In obtaining the numerical results, different quadrature schemes were extensively tested, namely Gauss-Legendre, Trapezoidal, Simpson, and Boole. Among the quadrature schemes for uniformly spaced meshes tested, the Boole's rule had

Table 4.10: Surrogate flux $P(r)$ computed with Gauss-Legendre rule for $R = 10$, $\Psi_b(r) = 0$, $N = 3201$, and different values of c.

r	$c = 0.1$	$c = 0.15$	$c = 0.2$	$c = 0.25$
0	0.218198e-4	0.256864e-4	0.306790e-4	0.372505e-4
1	0.286832e-4	0.336496e-4	0.400294e-4	0.48378**0**-4
2	0.560906e-4	0.6531**69**e-4	0.77036**3**e-4	0.921787e-4
3	0.132442e-3	0.152913e-3	0.178578e-3	0.211254e-3
4	0.342077e-3	0.391281e-3	0.452101e-3	0.528318e-3
5	0.933715e-3	0.105700e-2	0.120704e-2	0.139184e-2
6	0.266667e-2	0.298339e-2	0.336212e-2	0.381968e-2
7	0.798668e-2	0.881266e-2	0.978052e-2	0.109243e-1
8	0.254732e-1	0.276356e-1	0.301085e-1	0.329550e-1
9	0.907754e-1	0.962760e-1	0.102371e-0	0.109156e-0
10	0.526092e-0	0.533448e-0	0.541241e-0	0.549525e-0

The highlighted values are one unit smaller in the last place if compared with Ganapol's benchmarks [47].

Table 4.11: $C(r)$ function for $R = 10$, $\Psi_b(r) = 0$ and $N = 4001$.

r	$c = 0.3$	$c = 0.5$	$c = 0.7$	$c = 0.9$
0	0.000000e-0	0.000000e-0	0.000000e-0	0.000000e-0
1	0.184303e-4	0.389822e-4	0.130955e-3	0.104474e-2
2	0.534070e-4	0.107912e-3	0.333733e-3	0.231088e-2
3	0.138456e-3	0.262732e-3	0.724214e-3	0.407205e-2
4	0.360162e-3	0.635751e-3	0.153521e-2	0.671926e-2
5	0.956164e-3	0.155958e-2	0.326708e-2	0.108557e-1
6	0.259910e-2	0.389208e-2	0.702139e-2	0.174461e-1
7	0.725771e-2	0.990046e-2	0.152642e-1	0.280614e-1
8	0.209862e-1	0.257960e-1	0.336452e-1	0.453015e-1
9	0.641922e-1	0.698261e-1	0.757463e-1	0.736022e-1
10	0.229733e-0	0.210537e-0	0.181187e-0	0.121792e-0

presented the better performance in all our numerical experiments, although Simpson's quadrature provided very similar results (see Tables 4.13-4.16). In addition, analyzing the convergence of scalar flux, it was verified that oscillation in results rarely appear in uniformly spaced meshes, unlike what happened with the Gauss-Legendre quadrature (see Table 4.16).

Furthermore, we note that, for some cases the Gauss-Legendre rule presented better results if compared to the other tested schemes. For example, it showed greater compatibility with benchmarks presented in Table 4.10. In particular, this

Table 4.12: $C(r)$ function for $R = 10$, $\Psi_b(r) = 0$ and $N = 4001$.

r	$c = 0.1$	$c = 0.15$	$c = 0.2$	$c = 0.25$
0	0.000000e-0	0.000000e-0	0.000000e-0	0.000000e-0
1	0.113254e-4	0.125682e-4	0.140974e-4	0.160069e-4
2	0.336497e-4	0.371580e-4	0.414416e-4	0.467437e-4
3	0.903044e-4	0.990372e-4	0.109583e-3	0.122476e-3
4	0.244640e-3	0.266123e-3	0.291723e-3	0.322562e-3
5	0.679825e-3	0.732693e-3	0.794737e-3	0.868227e-3
6	0.194516e-2	0.207437e-2	0.222334e-2	0.239639e-2
7	0.575879e-2	0.606628e-2	0.641341e-2	0.680752e-2
8	0.178390e-1	0.185156e-1	0.192591e-1	0.200789e-1
9	0.594902e-1	0.605804e-1	0.617260e-1	0.629293e-1
10	0.243762e-0	0.240603e-0	0.237230e-0	0.233618e-0

quadrature provided rapid convergence at the origin and at the boundary (or at points very close to). However, the Gaussian quadrature caused a larger difficulty in the numerical integration with algorithms of the GSL library (isolated cases with the presence of error in the computation of integrals using a very small tolerance), which was partially controlled by the computational refinements performed. Then, the use of Boole quadrature has shown to be a safer approach due to the sensitivity of the integration algorithms in points close to the singularities, although the difference between the results is small, disappearing as the value of N increases. For example, if the Gauss-Legendre quadrature is used to generate the results in the Tables 4.1-4.6, very few values appear different, always with only a difference of one unit in the last decimal place. Also, regardless of the scheme used, the reduction in tolerance in numerical integration did not produce different results considering up to the eighth decimal place.

In Table 4.17 are presented the computational times demanded to determine the profiles of scalar flux, current, surrogate flux, and $C(r)$ for a given value of c. Each result in the table includes the time necessary for the generation of look-up tables for integrals. We note that the recorded times refer to problems with vacuum boundary condition. However, if a constant boundary condition is used, a negligible increase in time is needed. We emphasize that computational techniques employed

Table 4.13: Convergence of scalar flux $\Phi(r)$ for trapezoidal rule with $R = 1$, $\Psi_b(r) = 0$, $\sigma_t = 1$, $\sigma_s = 0.5$, $Q = 1$.

r	$N = 101$	$N = 201$	$N = 401$	$N = 801$	$N = 1601$	$N = 3201$
0.0	1.08585956	1.08586642	1.08586834	1.08586886	1.08586901	1.08586905
0.1	1.08219531	1.08220235	1.08220431	1.08220486	1.08220500	1.08220504
0.2	1.07109137	1.07109863	1.07110066	1.07110122	1.07110137	1.07110141
0.3	1.05219882	1.05220638	1.05220849	1.05220907	1.05220923	1.05220927
0.4	1.02488459	1.02489252	1.02489475	1.02489536	1.02489552	1.02489557
0.5	0.98813360	0.98814206	0.98814441	0.98814506	0.98814524	0.98814529
0.6	0.94035452	0.94036367	0.94036622	0.94036693	0.94036712	0.94036717
0.7	0.87896640	0.87897655	0.87897938	0.87898016	0.87898037	0.87898043
0.8	0.79937092	0.79938263	0.79938589	0.79938679	0.79938704	0.79938711
0.9	0.69149017	0.69150485	0.69150894	0.69151008	0.69151039	0.69151047
1.0	0.50486458	0.50490620	0.50491895	0.50492278	0.50492392	0.50492425

Table 4.14: Convergence of scalar flux $\Phi(r)$ for Simpson's rule with $R = 1$, $\Psi_b(r) = 0$, $\sigma_t = 1$, $\sigma_s = 0.5$, $Q = 1$.

r	$N = 101$	$N = 201$	$N = 401$	$N = 801$	$N = 1601$	$N = 3201$
0.0	1.08586766	1.08586870	1.08586897	1.08586904	1.08586906	1.08586906
0.1	1.08220362	1.08220470	1.08220497	1.08220504	1.08220505	1.08220506
0.2	1.07109996	1.07110106	1.07110133	1.07110140	1.07110142	1.07110142
0.3	1.05220778	1.05220891	1.05220919	1.05220926	1.05220928	1.05220929
0.4	1.02489400	1.02489518	1.02489548	1.02489556	1.02489558	1.02489558
0.5	0.98814361	0.98814488	0.98814520	0.98814528	0.98814530	0.98814530
0.6	0.94036535	0.94036673	0.94036707	0.94036716	0.94036718	0.94036719
0.7	0.87897839	0.87897993	0.87898032	0.87898042	0.87898044	0.87898045
0.8	0.79938474	0.79938653	0.79938698	0.79938710	0.79938712	0.79938713
0.9	0.69150745	0.69150974	0.69151031	0.69151045	0.69151049	0.69151050
1.0	0.50490878	0.50492006	0.50492320	0.50492406	0.50492430	0.50492436

to accelerate the computations reduced the run-time of our algorithm considerably. Furthermore, it should be noted that the times necessary were reduced, if compared with those presented in [23]. The reduction in the time required to produce the numerical results is justified by optimizations carried out in our code and by the use of the iterative method (3.64) to solve the linear system, instead of the use of the GSL routine of Gaussian elimination.

It is important to note that our methodology was able to reproduce the high precision benchmarks of Siewert and Thomas Jr. [94], unlike other strategies available in the literature. Among them we can cite the works of Thynell and

Table 4.15: Convergence of scalar flux $\Phi(r)$ for Boole's rule with $R = 1$, $\Psi_b(r) = 0$, $\sigma_t = 1$, $\sigma_s = 0.5$, $Q = 1$.

r	$N = 101$	$N = 201$	$N = 401$	$N = 801$	$N = 1601$	$N = 3201$
0.0	1.08586794	1.08586878	1.08586899	1.08586905	1.08586906	1.08586906
0.1	1.08220389	1.08220477	1.08220499	1.08220504	1.08220505	1.08220506
0.2	1.07110026	1.07110113	1.07110135	1.07110141	1.07110142	1.07110142
0.3	1.05220805	1.05220898	1.05220921	1.05220927	1.05220928	1.05220929
0.4	1.02489432	1.02489526	1.02489550	1.02489556	1.02489558	1.02489558
0.5	0.98814392	0.98814496	0.98814522	0.98814528	0.98814530	0.98814530
0.6	0.94036572	0.94036682	0.94036710	0.94036717	0.94036718	0.94036719
0.7	0.87897876	0.87898004	0.87898035	0.87898042	0.87898044	0.87898045
0.8	0.79938522	0.79938665	0.79938701	0.79938710	0.79938713	0.79938713
0.9	0.69150793	0.69150989	0.69151035	0.69151046	0.69151049	0.69151050
1.0	0.50491143	0.50492081	0.50492341	0.50492412	0.50492431	0.50492437

Table 4.16: Convergence of scalar flux $\Phi(r)$ for Gauss-Legendre quadrature rule with $R = 1$, $\Psi_b(r) = 0$, $\sigma_t = 1$, $\sigma_s = 0.5$, $Q = 1$.

r	$N = 101$	$N = 201$	$N = 401$	$N = 801$	$N = 1601$	$N = 3201$
0.0	1.08586907	1.08586907	1.08586906	1.08586906	1.08586906	1.08586906
0.1	1.08220524	1.08220505	1.08220506	1.08220506	1.08220506	1.08220506
0.2	1.07110234	1.07110123	1.07110137	1.07110141	1.07110142	1.07110143
0.3	1.05220782	1.05220908	1.05220933	1.05220930	1.05220929	1.05220929
0.4	1.02489563	1.02489623	1.02489575	1.02489556	1.02489559	1.02489558
0.5	0.98814537	0.98814531	0.98814530	0.98814530	0.98814530	0.98814530
0.6	0.94036705	0.94036611	0.94036691	0.94036723	0.94036718	0.94036720
0.7	0.87898488	0.87898108	0.87898031	0.87898043	0.87898043	0.87898045
0.8	0.79938165	0.79938834	0.79938747	0.79938722	0.79938715	0.79938713
0.9	0.69150780	0.69151062	0.69151049	0.69151048	0.69151049	0.69151050
1.0	0.50492439	0.50492439	0.50492439	0.50492439	0.50492439	0.50492439

Ozişik [101] and Wu and Wu [108], who solved accurately the related problem in radiative transfer theory. Thynell and Ozişik [101] used the Galerkin method and a collocation method. In the paper of Wu and Wu [108], the Nyström method was used, but the integrals are approximated by using the partition-extrapolation technique, which limited the obtainment of higher precision results.

Thynell and Ozişik [101] state that F_N have the disadvantage of requiring the knowledge of a particular solution corresponding to the inhomogeneous source term within the medium, which can make the method not be extendable to more complicated cases. In this way, the main advantage of the use of the pro-

Table 4.17: Approximate CPU time, in seconds, for compute $\Phi(r)$, $J(r)$, $P(r)$, and $C(r)$ in a Intel Core i7-7500U 2.70GHz machine (using a single core).

R	$N = 101$	$N = 201$	$N = 401$	$N = 801$	$N = 1601$	$N = 3201$	$N = 4001$
1	3	4	5	10	30	101	156
10	3	4	6	15	41	142	226

posed strategy, if compared with F_N method, is the possible generalization for more complex problems, including more general geometries. This can be noted in the papers [36] and [88]. Furthermore, the results presented in the present study show the potential of the methodology to deal with non-rectangular geometries, whose results are scarce in the literature.

Altaç [8] is another author who has worked with a cylindrical transport problem. An one group constant source problem for a homogeneous cylinder of radius 1 cm was used for comparison of the flux profile at spatial points with the total and scattering macroscopic cross sections for the homogeneous region being 1 and 0.382 cm^{-1}, respectively. A constant source of unit strength was used everywhere in the region and the vacuum/blackbody boundary condition was used at the surface of the cells. As mentioned by the author, the results in [8] are of limited accuracy (two digit of precision in general).

For such a problem, Bublitz *et al.* [23] present results to the scalar flux profile with at least six figures of precision using different quadrature schemes. The convergence of scalar flux for different quadrature schemes, the convergence of the surrogate flux and the function $C(r)$ for the Boole's rule and contour lines of the scalar flux and vector field of the current for the same problem can also be seen in [23].

In an article published in 2003, Altaç [5] provided more accurate results for several transport problems with cylindrical geometries in the radiative transfer theory. More recently, Zhou and Li [113] used the Chebyshev collocation spectral method to obtain high precision results for similar problems. In the Table 4.18 a

comparison of current work solutions with those available in [5, 113] for a problem with $Q = 0$ and $\Psi_b = 1$ is presented. We note that our solutions are obtained with Boole's rule using $N = 3201$. In addition, an increasing M needs to be used in the iterative process as the value of σ_s approaches 1, especially for $R = 2.5$. An excellent agreement is observed. More than that, since it is not necessary to take a high N to achieve six decimal places of precision with our methodology (see Tables 4.13-4.16), we expect that current work results are of higher quality.

Table 4.18: Comparison of current work solutions (CW), for a problem with $Q = 0$ and $\Psi_b = 1$, with those presented in [5, 113].

R	σ_s	$\Phi(0)$		$\Phi(R)$		$-J(R)$		
		Ref. [5]	CW	Ref. [5]	CW	Ref. [5]	Ref. [113]	CW
0.5	0.1	0.53493	0.5349268	0.75051	0.7505100	1.75493	1.754932	1.7549316
	0.3	0.60112	0.6011231	0.78907	0.7890740	1.48903	-	1.4890314
	0.5	0.68278	0.6827767	0.83480	0.8348045	1.17066	1.170660	1.1706598
	0.7	0.78557	0.7855746	0.89015	0.8901530	0.78159	-	0.7815956
	0.9	0.91829	0.9182901	0.95887	0.9588708	0.29391	0.2939137	0.2939137
	0.999	0.99912	0.9991211	0.99956	0.9995617	0.00314	-	0.0031394
1.0	0.1	0.29926	0.2992557	0.65289	0.6528948	2.44210	2.442099	2.4420987
	0.3	0.36440	0.3644052	0.69437	0.6943690	2.16467	-	2.1646720
	0.5	0.45707	0.4570655	0.74754	0.7475378	1.80140	1.801406	1.8014057
	0.7	0.59661	0.5966075	0.81947	0.8194700	1.29893	-	1.2989363
	0.9	0.82468	0.8246774	0.92493	0.9249286	0.54530	0.5453072	0.5453072
	0.999	0.99794	0.9979437	0.99914	0.9991408	0.00626	-	0.0062736
2.5	0.1	0.05676	0.0567642	0.56701	0.5670056	2.94701	-	2.9470150
	0.3	0.08108	0.0810839	0.60301	0.6030127	2.73078	-	2.7307846
	0.5	0.12661	0.1266065	0.65105	0.6510430	2.43168	-	2.4316838
	0.7	0.22729	0.2272875	0.72218	0.7221724	1.96833	-	1.9683484
	0.9	0.52983	0.5298299	0.85483	0.8548249	1.05227	-	1.0522892
	0.999	0.99237	0.9923665	0.99788	0.9978769	0.01560	-	0.0156278

Finally, we observe that there is an interest in transport solutions for multiplying media in critical, cylindrical geometry, which arises from the widespread occurrence of such configurations in reactor design and fuel process plant applications [107]. In multiplying media where the only source is fission, i.e., in equation (3.1) of our problem, replacing Q with

$$Q(\mathbf{x}) = \frac{\nu\sigma_f}{4\pi} \int_{S^2} \Psi(\mathbf{x}, \Omega')\, d\Omega', \tag{4.3}$$

the mean number of secondary neutrons per collision can be defined by $c = (\nu\sigma_f + \sigma_s)/\sigma_t$, where ν is the average number of neutrons produced per fission and σ_f stands for the macroscopic fission cross section [77].

With the assumption of isotropic scattering, the monoenergetic form of the neutron transport equation has been solved by several researchers to obtain values of critical radii for the axially infinite cylinder. Here, we compute the critical value $\sigma_c = 1/\lambda_c$ from the previously defined radius R. In the Table 4.19 we present the values obtained for the critical eigenvalue, for several values of R, by using equation (3.67). We note that our results are compatible with those presented by Sanchez [86], Westfall [107], Thomas Jr. *et al.* [97] and Ganapol [47]. Furthermore, we note that our results are the same as those obtained in [23]. In such paper, the critical value was determined by a GSL routine of eigenvalue determination. It can be noted that such approach, unlike the use of the Rayleigh quotient (3.67), becomes very time consuming as N increases.

Table 4.19: Critical value σ_c computed with Boole's rule, $N = 1001$ and several values of R. The iterative process with $M = 500$ was used.

R	σ_c
13.12551647	1.010000005
9.04325484	1.020000009
7.2314062	1.030000011
6.1499466	1.040000013
5.41128828	1.050000014
3.57739129	1.100000019
2.28720926	1.200000025
1.72500292	1.300000029
1.39697859	1.400000031
1.17834084	1.500000038
1.02083901	1.600000034
0.90139555	1.700000039
0.80742662	1.800000042
0.73142605	1.900000040
0.66861286	2.000000060

Table 4.20: Convergence of critical value σ_c computed with Boole's rule and several values of R.

R	$N = 101$	$N = 201$	$N = 401$	$N = 801$	$N = 1601$	$N = 3201$
0.5	2.393189639	2.393185578	2.393184534	2.393184269	2.393184202	2.393184186
0.7	1.947774309	1.947771052	1.947770209	1.947769994	1.947769940	1.947769926
0.9	1.667048060	1.683244479	1.692043450	1.696631387	1.698969278	1.700147364
2.5	1.175105056	1.175103689	1.175103297	1.175103192	1.175103165	1.175103158
4.5	1.068483150	1.068482571	1.068482342	1.068482274	1.068482255	1.068482251
6.5	1.036277439	1.036277433	1.036277312	1.036277266	1.036277253	1.036277249
8.5	1.022397696	1.022398169	1.022398133	1.022398103	1.022398093	1.022398090

In Table 4.20 we added the computed data to the convergence of critical value σ_c, with respect with the size of the mesh N, computed with Boole's rule and several values of R (for other values of R see [23]). We note that the greater the value of R, the greater must be the value of M in (3.64) to obtain an accurate eigenvalue. For example, for $R = 10$, a little less than 300 iterations are required to determine a converged with eight decimal places (with respect to M) critical value, while $M = 30$ is more than enough to get this many converged decimal places to scalar flux and current. However, the computational time to compute the additional iterations is negligible.

4.3 Problem 2

In this section we preset the results obtained for the Problem 2. No results were found in the literature for this problem. Then, for the purposes of validation of our code, we consider an axisymmetric problem with $\Psi_b(\mathbf{x}) = 0$, $Q = 1$, $\sigma_s = 0.5$ and $\sigma_t = 1$ and compare the results with those provided for Problem 1 (see Table 4.15 in Section 4.2).

Efficient quadrature rules for the disc are difficult to obtain. A survey of known cubature formulas for the unit disc is presented in [31]. Since the available quadrature rules have a small number of points, their use is not suitable for the Nyström method application if we want high precision results. An alternative is to construct a product rule with appropriate one-dimensional quadratures [31]. In our numerical tests the use of Gauss-Chebyshev quadrature for angular variable proved to be an efficient approach, unlike the use of other quadratures. For the radial variable, different quadrature rules are tested, with Boole's and Gauss-Legendre rules being the ones that stood out.

Table 4.21: Convergence of scalar flux $\Phi(\mathbf{x}) = \Phi(r,\theta)$ for $R = 1$, $\Psi_b(\mathbf{x},\Omega) = 0$, $\sigma_t = 1$, $\sigma_s = 0.5$, $Q = 1$. $N = N_r = N_\theta + 1$. Gauss-Legendre rule for the radial variable.

r	$N = 101$	$N = 201$	$N = 401$	$N = 801$	Problem 1
0.0	1.0858689	1.0858690	1.0858691	1.0858691	1.0858691
0.1	1.0822049	1.0822050	1.0822051	1.0822051	1.0822050
0.2	1.0711016	1.0711013	1.0711014	1.0711014	1.0711014
0.3	1.0522087	1.0522092	1.0522093	1.0522093	1.0522093
0.4	1.0248955	1.0248956	1.0248956	1.0248956	1.0248956
0.5	0.9881454	0.9881453	0.9881453	0.9881453	0.9881453
0.6	0.9403676	0.9403672	0.9403672	0.9403672	0.9403672
0.7	0.8789815	0.8789806	0.8789805	0.8789804	0.8789804
0.8	0.7993893	0.7993874	0.7993872	0.7993871	0.7993871
0.9	0.6915160	0.6915112	0.6915106	0.6915105	0.6915105
1.0	0.5048018	0.5048889	0.5049144	0.5049216	0.5049244

Table 4.22: Convergence of scalar flux $\Phi(\mathbf{x}) = \Phi(r,\theta)$ for $R = 1$, $\Psi_b(\mathbf{x},\Omega) = 0$, $\sigma_t = 1$, $\sigma_s = 0.5$, $Q = 1$. $N = N_r = N_\theta + 1$. Boole's rule for the radial variable.

r	$N = 101$	$N = 201$	$N = 401$	$N = 801$	Problem 1
0.0	1.0858677	1.0858688	1.0858690	1.0858691	1.0858691
0.1	1.0822037	1.0822047	1.0822050	1.0822050	1.0822050
0.2	1.0711000	1.0711011	1.0711014	1.0711014	1.0711014
0.3	1.0522077	1.0522089	1.0522092	1.0522093	1.0522093
0.4	1.0248938	1.0248952	1.0248955	1.0248956	1.0248956
0.5	0.9881431	0.9881448	0.9881452	0.9881453	0.9881453
0.6	0.9403644	0.9403667	0.9403671	0.9403672	0.9403672
0.7	0.8789765	0.8789798	0.8789803	0.8789804	0.8789804
0.8	0.7993813	0.7993862	0.7993870	0.7993871	0.7993871
0.9	0.6914997	0.6915089	0.6915102	0.6915105	0.6915105
1.0	0.5050865	0.5049716	0.5049378	0.5049281	0.5049244

Table 4.23: Convergence of scalar flux $\Phi(r,\theta)$ for $R = 1$, $\Psi_b(\mathbf{x},\Omega) = 0$, $\sigma_t = 1$, $\sigma_s = 0.5$, $Q = 1$. $N_r = 201$. Gauss-Legendre rule for the radial variable.

r	$N_\theta = 100$	$N_\theta = 200$	$N_\theta = 400$	$N_\theta = 800$	$N_\theta = 1600$	$N_\theta = 3200$	Problem 1
0.0	1.0858688	1.0858690	1.0858691	1.0858691	1.0858691	1.0858691	1.0858691
0.1	1.0822048	1.0822050	1.0822051	1.0822051	1.0822051	1.0822051	1.0822051
0.2	1.0711012	1.0711013	1.0711012	1.0711012	1.0711012	1.0711012	1.0711014
0.3	1.0522091	1.0522092	1.0522091	1.0522091	1.0522091	1.0522091	1.0522093
0.4	1.0248955	1.0248956	1.0248958	1.0248961	1.0248962	1.0248962	1.0248956
0.5	0.9881454	0.9881453	0.9881453	0.9881453	0.9881453	0.9881453	0.9881453
0.6	0.9403676	0.9403672	0.9403670	0.9403666	0.9403663	0.9403661	0.9403672
0.7	0.8789814	0.8789806	0.8789806	0.8789809	0.8789811	0.8789811	0.8789805
0.8	0.7993893	0.7993874	0.7993872	0.7993877	0.7993882	0.7993883	0.7993871
0.9	0.6915160	0.6915112	0.6915106	0.6915105	0.6915106	0.6915106	0.6915105
1.0	0.5048018	0.5048889	0.5049144	0.5049216	0.5049236	0.5049242	0.5049244

Table 4.24: Convergence of scalar flux $\Phi(r,\theta)$ for $R = 1$, $\Psi_b(\mathbf{x},\Omega) = 0$, $\sigma_t = 1$, $\sigma_s = 0.5$, $Q = 1$. $N_\theta = 200$. Gauss-Legendre rule for the radial variable.

r	$N_r = 101$	$N_r = 201$	$N_r = 401$	$N_r = 801$	$N_r = 1601$	Problem 1
0.0	1.0858688	1.0858690	1.0858690	1.0858690	1.0858690	1.0858691
0.1	1.0822052	1.0822050	1.0822050	1.0822050	1.0822050	1.0822051
0.2	1.0711022	1.0711013	1.0711014	1.0711014	1.0711014	1.0711014
0.3	1.0522081	1.0522092	1.0522093	1.0522093	1.0522093	1.0522093
0.4	1.0248956	1.0248956	1.0248956	1.0248956	1.0248956	1.0248956
0.5	0.9881453	0.9881453	0.9881453	0.9881453	0.9881453	0.9881453
0.6	0.9403672	0.9403672	0.9403672	0.9403672	0.9403672	0.9403672
0.7	0.8789813	0.8789806	0.8789806	0.8789806	0.8789806	0.8789805
0.8	0.7993872	0.7993874	0.7993874	0.7993874	0.7993874	0.7993871
0.9	0.6915112	0.6915112	0.6915112	0.6915112	0.6915112	0.6915105
1.0	0.5048889	0.5048889	0.5048889	0.5048889	0.5048889	0.5049244

In the Tables 4.21-4.22 we present the convergence of the scalar flux for a homogeneous cylinder with internal energy source $Q = 1$, with vacuum boundary condition, and with macroscopic cross section $\sigma_s = 0.5$. For the radial variable the Gauss-Legendre rule was used to obtain the results available in 4.21, while results in 4.22 were obtained with the Boole's rule. In such tables, it can be noted an excellent agreement with the results presented for Problem 1 (see Tables 4.15 and 4.16). The agreement decreases as the point approaches the boundary $r = R$. We note that the scalar flux obtained was independent of the value of the angular variable (for the mesh points) in all decimal places presented. For the same problem, we add in Tables 4.23-4.24 the convergence of scalar flux $\Phi(r,\theta)$ obtained by refining the mesh in just one coordinate. It is observed that the mesh refinement in the coordinate θ is important for the scalar flux convergence for points on the boundary $r = R$.

In the Tables 4.25-4.28 we explore several convergence scenarios for a test problem with boundary condition $\Psi_b(\mathbf{x}) = \delta(\Omega - (1,0,0))$, i.e., with a collimated neutron flux $\psi_b = 1$ entering perpendicularly through the side surface of the cylinder. Gauss-Legendre and Boole quadratures are used in the discretization of radial variable. We note that, just as in Problem 1, the Gaussian quadrature caused a larger instability in the numerical integration algorithms of the GSL library. How-

ever, to the test problem this quadrature did not provide rapid convergence at the boundary, unlike what was observed in the case of Problem 1. The absolute error for the scalar flux presented in the last columns (that is, for $N = N_r = N_\theta + 1 = 801$) of the Tables 4.25 and 4.26 is expected to be less than 10^{-5}.

Table 4.25: Convergence of scalar flux $\Phi(r, 0)$ for $R = 1$, $\Psi_b(\mathbf{x}, \Omega) = \delta(\Omega - (1, 0, 0))$, $\sigma_t = 1$, $\sigma_s = 0.5$, $Q = 1$. $N = N_r = N_\theta + 1$. Gauss-Legendre rule for the radial variable.

r	$N = 101$	$N = 201$	$N = 401$	$N = 801$	$N = 1601$
0.0	1.1335768	1.1335768	1.1335768	1.1335768	1.1335768
0.1	1.1259166	1.1259178	1.1259185	1.1259189	1.1259191
0.2	1.1110518	1.1110538	1.1110553	1.1110562	1.1110566
0.3	1.0886216	1.0886256	1.0886277	1.0886288	1.0886294
0.4	1.0579826	1.0579868	1.0579893	1.0579906	1.0579913
0.5	1.0180546	1.0180827	1.0180973	1.0181047	1.0181085
0.6	0.9673711	0.9673751	0.9673777	0.9673791	0.9673799
0.7	0.9031843	0.9031874	0.9031897	0.9031911	0.9031918
0.8	0.8209093	0.8209108	0.8209127	0.8209138	0.8209144
0.9	0.7104056	0.7104032	0.7104042	0.7104051	0.7104056
1.0	0.5208008	0.5208906	0.5209173	0.5209252	0.5209276

Table 4.26: Convergence of scalar flux $\Phi(r, 0)$ for $R = 1$, $\Psi_b(\mathbf{x}, \Omega) = \delta(\Omega - (1, 0, 0))$, $\sigma_t = 1$, $\sigma_s = 0.5$, $Q = 1$. $N = N_r = N_\theta + 1$. Boole's rule for the radial variable.

r	$N = 101$	$N = 201$	$N = 401$	$N = 801$	$N = 1601$
0.0	1.1335757	1.1335765	1.1335767	1.1335767	1.1335768
0.1	1.1259072	1.1259129	1.1259162	1.1259178	1.1259186
0.2	1.1110362	1.1110468	1.1110519	1.1110545	1.1110557
0.3	1.0886071	1.0886175	1.0886237	1.0886269	1.0886284
0.4	1.0579642	1.0579781	1.0579850	1.0579885	1.0579902
0.5	1.0180861	1.0180978	1.0181049	1.0181086	1.0181104
0.6	0.9673516	0.9673662	0.9673733	0.9673770	0.9673788
0.7	0.9031662	0.9031783	0.9031853	0.9031889	0.9031907
0.8	0.8208861	0.8209013	0.8209082	0.8209116	0.8209133
0.9	0.7103769	0.7103927	0.7103995	0.7104028	0.7104044
1.0	0.5210838	0.5209704	0.5209389	0.5209307	0.5209288

In Table 4.29 are presented the computational times demanded to determine the profile of scalar flux for a given value of σ_s. Each result in the table includes the time necessary for the generation of look-up tables for integrals.

Table 4.27: Convergence of scalar flux $\Phi(r,0)$ for $R=1$, $\Psi_b(\mathbf{x},\Omega)=\delta(\Omega-(1,0,0))$, $\sigma_t=1$, $\sigma_s=0.5$, $Q=1$. $N_\theta=200$. Gauss-Legendre rule for the radial variable.

r	$N_r=101$	$N_r=201$	$N_r=401$	$N_r=801$	$N_r=1601$
0.0	1.1335768	1.1335768	1.1335768	1.1335768	1.1335768
0.1	1.1259162	1.1259178	1.1259186	1.1259191	1.1259193
0.2	1.1110515	1.1110538	1.1110556	1.1110564	1.1110569
0.3	1.0886196	1.0886256	1.0886280	1.0886292	1.0886298
0.4	1.0579813	1.0579868	1.0579896	1.0579910	1.0579917
0.5	1.0180531	1.0180827	1.0180977	1.0181052	1.0181089
0.6	0.9673690	0.9673751	0.9673781	0.9673797	0.9673804
0.7	0.9031825	0.9031874	0.9031902	0.9031917	0.9031924
0.8	0.8209056	0.8209108	0.8209133	0.8209145	0.8209152
0.9	0.7103993	0.7104032	0.7104052	0.7104062	0.7104067
1.0	0.5208880	0.5208906	0.5208919	0.5208925	0.5208928

In summary, our methodology proved to be effective in solving the transport problem in a non-axisymmetric infinite cylinder (with the assumptions established at the beginning of Chapter 3). To do so, it was necessary to choose the appropriate quadrature for discretization of the angular variable. Unfortunately, the lack of data in the literature made it impossible to carry out a more detailed analysis of the numerical results obtained. However, the development of Problem 2 was important because it should help in the treatment of the three-dimensional problem without axisymmetry (non-axisymmetric finite cylinder).

Table 4.28: Convergence of scalar flux $\Phi(r,0)$ for $R=1$, $\Psi_b(\mathbf{x},\Omega)=\delta(\Omega-(1,0,0))$, $\sigma_t=1$, $\sigma_s=0.5$, $Q=1$. $N_r=201$. Gauss-Legendre rule for the radial variable.

r	$N_\theta=100$	$N_\theta=200$	$N_\theta=400$	$N_\theta=800$	$N_\theta=1600$	$N_\theta=3200$
0.0	1.1335768	1.1335768	1.1335768	1.1335768	1.1335768	1.1335768
0.1	1.1259182	1.1259178	1.1259176	1.1259176	1.1259176	1.1259176
0.2	1.1110546	1.1110538	1.1110535	1.1110534	1.1110534	1.1110534
0.3	1.0886267	1.0886256	1.0886251	1.0886250	1.0886250	1.0886250
0.4	1.0579881	1.0579868	1.0579867	1.0579868	1.0579869	1.0579870
0.5	1.0180842	1.0180827	1.0180823	1.0180823	1.0180822	1.0180822
0.6	0.9673770	0.9673751	0.9673744	0.9673739	0.9673735	0.9673733
0.7	0.9031898	0.9031874	0.9031870	0.9031872	0.9031873	0.9031873
0.8	0.8209142	0.8209108	0.8209102	0.8209106	0.8209111	0.8209112
0.9	0.7104094	0.7104032	0.7104023	0.7104021	0.7104022	0.7104022
1.0	0.5208034	0.5208906	0.5209160	0.5209233	0.5209253	0.5209259

Table 4.29: Approximate CPU time (in seconds) for compute $\Phi(\mathbf{x})$ in a Intel Core i7-7500U 2.7GHz machine, using OpenMP (with four threads).

	$N_r=101$	$N_r=201$	$N_r=401$	$N_r=801$	$N_r=1601$
$N_\theta=100$	6	9			
$N_\theta=200$	9	23	80	328	1594
$N_\theta=400$		83	322		
$N_\theta=800$		322		6458	
$N_\theta=1600$		1283			
$N_\theta=3200$		5865			

4.4 Problem 3

In the present section the results obtained for Problem 3 are given. Detailed research involving this problem and with improved results is presented in the paper [24] (see at https://doi.org/10.1016/j.jqsrt.2022.108087) for the context of radiative transfer theory. In order to compare the numerical results for the scalar flux and the current profiles with those available in the literature, the following problems were considered:

- *Case 1*: Axisymmetrical homogeneous solid cylinder with internal energy source $Q=1-\sigma_s$, with vacuum boundary condition, and with

macroscopic cross section $\sigma_s = 0.5$. Finite cylinders of several dimensions are treated;

- *Case 2*: Axisymmetrical homogeneous solid cylinder exposed to a uniform collimated neutron beam (normal to the bottom surface) with non-reflecting boundaries and no internal energy source ($Q = 0$). Finite cylinders of several dimensions are treated. Cases with $\sigma_s = 1$ were predominantly chosen.

The obtained results were compared with those available in the literature: the works of Li *et al.* [69], Zhang and Sutton [111, 112], and Sutton and Chen [96] for Case 1 and the researches of Wu and Wu [109] and Hsu and Tan [57] for Case 2. We note that these papers present results for the related problem in radiative transfer theory.

Table 4.30: $\Phi(r, 0.5L)$ and $J_r(r, 0.5L)$ for Case 1, $R = 1$, $L = 40$, $\sigma_s = 0.5$, $N = 1601$. Comparison between current work results and those for $\Phi(r)$ and $q(r)$ in the 1-D cylindrical medium.

r	$\Phi(r)$	$\Phi(r, 0.5L)$	$J(r)$	$J_r(r, 0.5L)$
0.00	6.822717	6.822716	0.000000	0.000000
0.25	6.676896	6.676896	0.363511	0.363511
0.50	6.208700	6.208700	0.755454	0.755453
0.75	5.289710	5.289710	1.211926	1.211923
1.00	3.172533	3.172557	1.801406	1.801434

It should be noted that there is a lack of high precision benchmarks dealing with the radiative transfer in cylindrical medium, since several published works are limited to presenting results only in graphics. Then, initially, to ensure that the present method is able to produce high precision results, the numerical outputs obtained for Case 1 with a large L are compared with those produced for the Problem 1.

For a fixed optical radius, scalar flux and current tends to limiting values as L increases, so that $\Phi(r, 0.5L) \to \Phi(r)$ and $J_r(r, 0.5L) \to J(r)$, where $\Phi(r)$

and $J(r)$ are scalar flux and current, respectively, for the infinite solid cylinder with same R. In special, for points in the interior of the medium, the axial component of the current vanishes as L increases.

In the Table 4.30 numerical results obtained using a mesh of $N = 1601$ for a cylindrical medium with $R = 1$, $L = 40$, and $\sigma_s = 0.5$ are presented. An excellent agreement between results is noted and the absolute error of our results is less than 3×10^{-5}. We note that even with the large L, there is a relatively fast convergence. This suggests that a smaller error can be obtained for the case of media with small dimensions.

Table 4.31: Scalar flux and current for Case 1, $R = 1$, $L = 1$, $N = 1601$.

		Ref. [111]	Ref. [112]	Current work
	0	4.4244	-	4.44721
$\Phi(r, 0.25)$	$r = 0.5$	4.1019	-	4.12695
	1	2.0671	-	2.01449
	0	4.7832	4.8022	4.80264
$\Phi(r, 0.5)$	$r = 0.5$	4.4263	4.4478	4.44838
	1	2.2168	2.1619	2.16214
	0	0.0000	-	0.0000
$J_r(r, 0.25)$	$r = 0.5$	0.3853	-	0.38553
	1	1.1981	-	1.20224
	0	0.0000	0.0000	0.0000
$J_r(r, 0.5)$	$r = 0.5$	0.4234	0.4232	0.42324
	1	1.2897	1.2929	1.29271
	0	-	1.4152	1.41522
$J_z(r, 1)$	$r = 0.5$	-	1.3097	1.30978
	1	-	0.6365	0.63647

In the Table 4.31 are presented the numerical results obtained for Case 1 with $R = L = 1$ and $\sigma_s = 0.5$, computed with $N = 1601$, in comparison with those presented by Zhang and Sutton [111, 112]. A better agreement is noted when comparing the present results with those presented in [112]. The absolute error for the current results is expected to be less than 2×10^{-4} for the scalar flux and less than 4×10^{-5} for the current. The error estimate for scalar flux was established by taking a value greater than the largest difference between the values obtained by the iterative process (3.110) and those obtained with equation (3.166) (since both

converge to the same value as N increases). On the other hand, the estimated absolute error for the current was based on convergence, which presented a better behavior when compared to convergence of Φ.

The results presented in the Tables 4.32-4.34 show the convergence of the used algorithm and aid to support the error estimate for this problem. For instance, for the radial current in Table 4.33 it should be noted that, for increasing N, the sequences of points $J_r(r, 0)$ are increasing, while sequences of points $J_r(r, L)$ are decreasing, but both are converging to the same value (for Case 1 it is known that $J_r(r, 0) = J_r(r, L)$). Furthermore, in Table 4.34 all sequences of points $J_z(r, 0.5L)$ for increasing N are converging to zero, noting that $J_z(r, 0.5L) = 0$ is a fact in the Case 1.

Table 4.32: Convergence of scalar flux $\Phi(r, z)$ for Case 1, $R = 1$, $L = 1$, $\sigma_s = 0.5$.

	N = 41	N = 101	N = 201	N = 401	N = 801	N = 1601
$\Phi(0.0, 0.0)$	2.736484	2.737537	2.737832	2.737968	2.738032	2.738063
$\Phi(0.0, 0.5)$	4.800681	4.801897	4.802296	4.802495	4.802593	4.802643
$\Phi(0.0, 1.0)$	2.737247	2.737836	2.737981	2.738042	2.738069	2.738082
$\Phi(0.5, 0.0)$	2.513418	2.514412	2.514705	2.514831	2.514891	2.514920
$\Phi(0.5, 0.5)$	4.446970	4.447854	4.448139	4.448278	4.448348	4.448382
$\Phi(0.5, 1.0)$	2.514043	2.514657	2.514826	2.514891	2.514921	2.514934
$\Phi(1.0, 0.0)$	1.281199	1.280779	1.280589	1.280482	1.280426	1.280397
$\Phi(1.0, 0.5)$	2.161708	2.162048	2.162119	2.162135	2.162139	2.162140
$\Phi(1.0, 1.0)$	1.280060	1.280302	1.280346	1.280359	1.280364	1.280366

Table 4.33: Convergence of radial component of current $J_r(r, z)$ for Case 1, $R = 1$, $L = 1$, $\sigma_s = 0.5$.

	N = 41	N = 101	N = 201	N = 401	N = 801	N = 1601
$J_r(0.0, z)$	0.000000	0.000000	0.000000	0.000000	0.000000	0.000000
$J_r(0.5, 0.0)$	0.285569	0.285379	0.285311	0.285277	0.285260	0.285251
$J_r(0.5, 0.5)$	0.422977	0.423141	0.423193	0.423219	0.423231	0.423238
$J_r(0.5, 1.0)$	0.285192	0.285225	0.285234	0.285238	0.285240	0.285241
$J_r(1.0, 0.0)$	0.744519	0.744071	0.743897	0.743805	0.743758	0.743734
$J_r(1.0, 0.5)$	1.292620	1.292689	1.292713	1.292715	1.292714	1.292714
$J_r(1.0, 1.0)$	0.743564	0.743674	0.743696	0.743704	0.743707	0.743708

We present new numerical results for the Case 1 with $R = L = 0.25$ in Table 4.35. The absolute error for the presented data is expected to be less than

Table 4.34: Convergence of axial component of current $J_z(r,z)$ for Case 1, $R = 1$, $L = 1$, $\sigma_s = 0.5$.

	N = 41	N = 101	N = 201	N = 401	N = 801	N = 1601
$J_z(0.0, 0.0)$	-1.414935	-1.415117	-1.415170	-1.415195	-1.415208	-1.415214
$J_z(0.0, 0.5)$	-0.001346	-0.000539	-0.000269	-0.000135	-0.000067	-0.000034
$J_z(0.0, 1.0)$	1.414986	1.415140	1.415182	1.415202	1.415211	1.415215
$J_z(0.5, 0.0)$	-1.309428	-1.309644	-1.309724	-1.309754	-1.309768	-1.309775
$J_z(0.5, 0.5)$	-0.001092	-0.000437	-0.000219	-0.000109	-0.000055	-0.000027
$J_z(0.5, 1.0)$	1.309495	1.309673	1.309739	1.309761	1.309772	1.309777
$J_z(1.0, 0.0)$	-0.636327	-0.636434	-0.636457	-0.636465	-0.636469	-0.636470
$J_z(1.0, 0.5)$	-0.000048	-0.000019	-0.000010	0.000005	0.000002	0.000001
$J_z(1.0, 1.0)$	0.636420	0.636472	0.636476	0.636475	0.636474	0.636473

2×10^{-5} for the scalar flux and less than 7×10^{-6} for the current. For a cylindrical medium with $R = L = 5$, new results are made available in Table 4.36. For this case, a larger absolute error is expected: less than 2×10^{-3} for the scalar flux and less than 2×10^{-4} for the current. Furthermore, in Table 4.37 are presented the computational times demanded to determine the profiles of scalar flux and current for a given value of σ_s. Each result in the table includes the time necessary for the generation of look-up tables for the necessary integrals.

Table 4.35: Scalar flux and current for Case 1, $R = 0.25$, $L = 0.25$, $\sigma_s = 0.5$, $N = 1601$.

x	$\Phi(r,0)$	$\Phi(r,L)$	$\Phi(0,z)$	$\Phi(R,z)$	$J_z(r,0)$	$J_z(r,L)$	$J_r(r,0)$	$J_r(R,z)$
0.00	0.837210	0.837211	0.837210	0.437933	-0.433078	0.433078	0.000000	0.265458
0.25	0.821470	0.821471	1.242326	0.625722	-0.425369	0.425368	0.058598	0.389284
0.50	0.770660	0.770661	1.329170	0.665377	-0.399780	0.399779	0.120270	0.415694
0.75	0.670059	0.670060	1.242331	0.625722	-0.346366	0.346366	0.188105	0.389283
1.00	0.437933	0.437931	0.837211	0.437931	-0.212058	0.212058	0.265458	0.265456

Note: $r = Rx$, $z = Lx$.

Table 4.36: Scalar flux and current for Case 1, $R = 5$, $L = 5$, $\sigma_s = 0.5$, $N = 1601$.

x	$\Phi(r,0)$	$\Phi(r,L)$	$\Phi(0,z)$	$\Phi(R,z)$	$J_z(r,0)$	$J_z(r,L)$	$J_r(r,0)$	$J_r(R,z)$
0.00	5.133589	5.133769	5.133589	2.139760	-2.645482	2.645566	0.000000	1.137007
0.25	5.109743	5.109926	10.998352	4.376639	-2.635461	2.635544	0.023825	2.382272
0.50	4.998680	4.998864	11.736540	4.621414	-2.587394	2.587476	0.083995	2.504080
0.75	4.582926	4.583097	10.998731	4.376678	-2.396581	2.396651	0.287278	2.382293
1.00	2.139760	2.139520	5.133769	2.139520	-1.091520	1.091534	1.137007	1.136819

Note: $r = Rx$, $z = Lx$.

Figure 4.3 shows the radial component of the $J_r(R,z)$ for Case 1 with $\sigma_s = 0.5$. For the case $R = L = 1$, there is a good agreement between the current

Table 4.37: Approximate CPU time, in seconds, for compute $\Phi(r,z)$, $J_r(r,z)$, $J_z(r,z)$, and $C(r)$ in a Intel Core i7-7500U 2.70GHz machine using OpenMP (with four threads).

R	$N=41$	$N=101$	$N=201$	$N=401$	$N=801$	$N=1601$
0.25	13	85	351	1569	8847	74964
1	17	113	452	1981	10475	81586
5	28	173	703	2969	14412	96971

work and the results of Sutton and Chen [96], while the results of Li *et al.* [69] appear to have limited accuracy for both cases $R = L = 1$ and $R = L = 5$. There are no results available in the paper of Sutton and Chen [96] for the case $R = L = 5$. To the same problem with $R = L = 1$, the Figure 4.4 shows a good agreement of the results for $\Phi(r, 0.5L)$, $J_r(r, 0.5L)$, and $J_z(r, L)$ if compared with those presented by Zhang and Sutton [111].

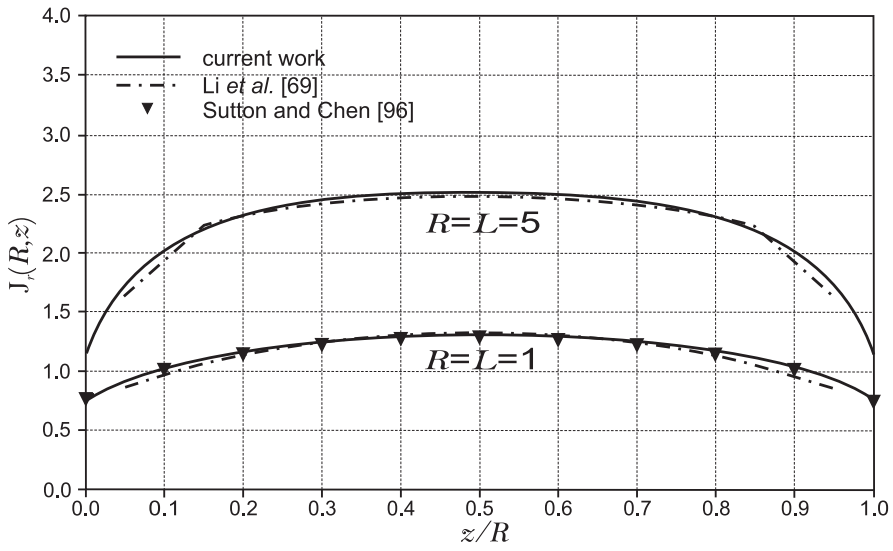

Figure 4.3: $J_r(R,z)$ for Case 1 with $\sigma_s = 0.5$. Comparison between current work results and those presented in [69] and [96].

In general, there is a good agreement between the numerical results presented in this work with those that used other integral methods to solve the Case 1 problem, namely the works of Zhang and Sutton [111, 112] and Sutton and Chen [96]. In particular, the agreement is greater when considering the paper [112] if compared with [111]. In the case of research of Sutton and Chen [96], the results

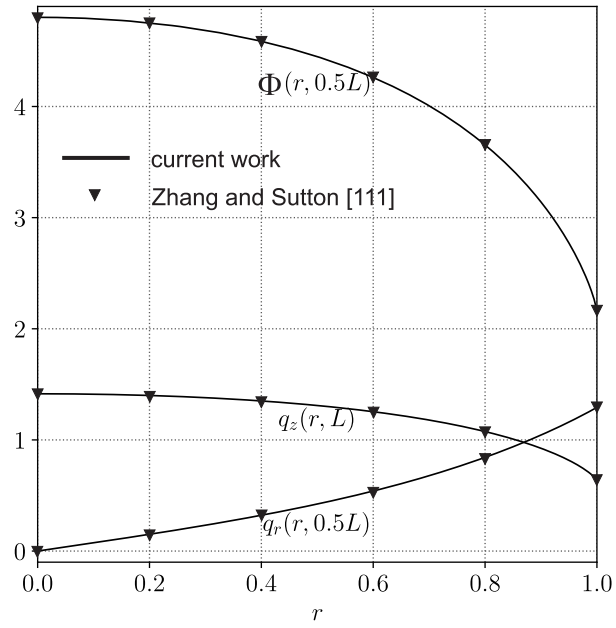

Figure 4.4: $\Phi(r, 0.5L)$, $J_r(r, 0.5L)$, and $J_z(r, L)$ for Case 1, $R = 1$, $L = 1$, $\sigma_s = 0.5$.

are presented only in graphs, which makes a head-to-head comparison impossible. Furthermore, the grids used in the papers of Zhang and Sutton [111,112] and Sutton and Chen [96] were very coarse, i.e., the authors did not explore convergence using finer meshes. We note that larger media need finer meshes to ensure accuracy.

The integral method proposed by Chen and Sutton in [29] and extended in [96] was able to solve a large class of radiative transfer problems in cylindrical media. However, although the method uses a change of variables to remove the singularities, the resultant integrals are still complicated, requiring attention if high accuracy is a concern. Numerical tests following the Chen and Sutton [29] proposal for the determination of integrals were carried out using GSL integration routines. The gain with the referred singularity removal is only noticed for points far from the boundary, if compared to the present strategy. Also, for points close to the boundary, the effect of the change of variables is the opposite due the complicated integration limits originated by the change of variables. So, a hybrid approach in

Table 4.38: Scalar flux for Case 2, $R = 0.5$, $L = 1$, $\sigma_s = 1$, $N = 1601$. Comparison between current work (CW) results and those presented in [109].

x	$\Phi(r,0)$		$\Phi(r,L)$		$\Phi(0,z)$		$\Phi(R,z)$	
	Ref. [109]	CW	Ref. [109]	CW	Ref. [109]	CW	Ref. [109]	CW
0.00000	1.285	1.28529	0.5352	0.53523	1.285	1.28529	1.142	1.14153
0.12497	1.284	1.28381	0.5343	0.53426	1.314	1.31417	1.087	1.08668
0.19798	1.282	1.28156	0.5328	0.53279	1.276	1.27643	1.035	1.03473
0.28298	1.278	1.27759	0.5302	0.53021	1.216	1.21627	0.9708	0.97064
0.37657	1.272	1.27145	0.5263	0.52627	1.140	1.13964	0.8995	0.89928
0.47507	1.263	1.26281	0.5208	0.52081	1.054	1.05357	0.8256	0.82540
0.57455	1.252	1.25150	0.5138	0.51380	0.9645	0.96449	0.7533	0.75311
0.67107	1.238	1.23756	0.5034	0.50538	0.8773	0.87727	0.6856	0.68542
0.76082	1.221	1.22130	0.4959	0.49587	0.7951	0.79511	0.6245	0.62435
0.84021	1.203	1.20329	0.4857	0.48572	0.7201	0.72010	0.5712	0.57113
0.90612	1.185	1.18446	0.4756	0.47557	0.6539	0.65386	0.5266	0.52652
0.95592	1.166	1.16621	0.4662	0.46619	0,5984	0.59839	0,4912	0.49122
0.98765	1.151	1.15063	0.4586	0.45860	0.5568	0.55677	0,4663	0.46634
1.00000	1.142	1.14153	0.4544	0.45443	0.5352	0.53523	0.4544	0.45443

Note: $r = Rx$, $z = Lx$.

the treatment of the integrals can be considered for creating an optimized technique to be used in future works.

Table 4.39: Current for Case 2, $R = 0.5$, $L = 1$, $\sigma_s = 1$, $N = 1601$. Comparison between current work (CW) results and those presented in [109].

x	$J_z(r,0)$		$J_z(r,L)$		$J_r(R,z)$	
	Ref. [109]	CW	Ref. [109]	CW	Ref. [109]	CW
0.0	0.8481	0.848064	0.4684	0.468443	0.0837	0.083687
0.12497	0.8488	0.848839	0.4679	0.467840	0.1244	0.124244
0.19798	0.8500	0.850021	0.4670	0.466924	0.1309	0.130727
0.28298	0.8521	0.852105	0.4654	0.465322	0.1325	0.132340
0.37657	0.8553	0.855342	0.4629	0.462866	0.1298	0.129565
0.47507	0.8599	0.859928	0.4595	0.459451	0.1236	0.123352
0.57455	0.8659	0.865981	0.4551	0.455060	0.1149	0.114751
0.67107	0.8735	0.873517	0.4498	0.449776	0.1048	0.104676
0.76082	0.8824	0.882432	0.4438	0.443784	0.0939	0.093831
0.84021	0.8924	0.892457	0.4374	0.437380	0.0828	0.082752
0.90612	0.9031	0.903127	0.4310	0.430951	0.0720	0.071921
0.95592	0.9137	0.913680	0.4250	0.425000	0.0620	0.061933
0.98765	0.9229	0.922888	0.4202	0.420176	0.0537	0.053696
1.00000	0.9284	0.928391	0.4175	0.417526	0.0490	0.048994

Note: $r = Rx$, $z = Lx$.

In the Tables 4.38 and 4.39 are the results obtained for Case 2 in comparison with results presented by Wu and Wu [109]. It should be noted that for the current $J_z(r,0)$, the numerical results of [109] were adapted since they referred to $J_z^+(r,0)$, the current leaving the surface $z=0$, i.e., did not consider the collimated incidence, which was added. Excellent agreement is observed for the scalar flux and the current if compared with benchmark results. The absolute error in the results computed with the present methodology is expected to be less than 3×10^{-5} for Table 4.38 and less than 7×10^{-6} for Table 4.39.

Table 4.40: Scalar flux for Case 2, $R=2$, $L=4$, $\sigma_s=1$, $N=1601$. Comparison between current work (CW) results and those presented in [57].

x	$\Phi(r,z_1)$		$\Phi(r,z_2)$		$\Phi(r_1,z)$		$\Phi(r_2,z)$	
	Ref. [57]	CW	Ref. [57]	CW	Ref. [57]	CW	Ref. [57]	CW
0.015625	1.93173	1.947382	0.15798	0.157689	1.93173	1.947382	1.37693	1.384630
0.078125	1.92982	1.945399	0.15746	0.157158	2.05274	2.039042	1.27774	1.273923
0.140625	1.92532	1.940744	0.15624	0.155928	1.94811	1.951140	1.11599	1.116271
0.203125	1.91815	1.933346	0.15431	0.153999	1.79435	1.795826	0.95789	0.960172
0.265625	1.90822	1.923090	0.15168	0.151378	1.61078	1.613386	0.81478	0.816974
0.328125	1.89542	1.909812	0.14839	0.148070	1.42307	1.424702	0.68800	0.689910
0.390625	1.87942	1.893285	0.14441	0.144082	1.23979	1.241437	0.55784	0.579223
0.453125	1.85997	1.873208	0.13979	0.139423	1.06891	1.069962	0.48277	0.483897
0.515625	1.83677	1.849179	0.13455	0.134100	0.91268	0.913362	0.40147	0.402407
0.578125	1.80930	1.820658	0.12866	0.128121	0.77259	0.772643	0.33244	0.333069
0.640625	1.77703	1.786902	0.12216	0.121491	0.64760	0.647490	0.27388	0.274211
0.703125	1.73885	1.746856	0.11494	0.114205	0.53733	0.536758	0.22413	0.224245
0.765625	1.69351	1.698929	0.10679	0.106243	0.43973	0.438766	0.18177	0.181702
0.828125	1.63591	1.640503	0.09778	0.097549	0.35424	0.351434	0.14540	0.145206
0.890625	1.56087	1.566539	0.08783	0.087968	0.27350	0.272183	0.11384	0.113404
0.984375	1.37693	1.384630	0.07006	0.070219	0.15798	0.157689	0.07006	0.070219

Note: $r=Rx$, $z=Lx$, $r_1=0.015625R$, $r_2=0.984375R$, $z_1=0.015625L$, $z_2=0.984375L$.

The accuracy of the results presented by Wu and Wu is due to the fact that the authors also used the Nyström method with singularity-subtraction. However, in their research, unlike what is being proposed in the current work, the integrals are approximated by using the partition-extrapolation technique [108], which limits the obtainment of higher precision results. This can be noticed by the fact that such method was not able to reproduce the results presented by Siewert and Thomas Jr. [94] for an infinite cylindrical problem (see [108]). Furthermore, in the present study, the discretization of the integrals in the Nyström method was made

by using the Boole's rule, which permits the reduction of degree of freedom in the integral kernels, and the consequent decrease of the memory storage, in comparison with the use of Gauss-Lobatto quadrature pointed in [109].

Table 4.41: Current for Case 2, $R = 2$, $L = 4$, $\sigma_s = 1$, $N = 1601$. Comparison between current work (CW) results and those presented in [57].

x	$J_z(r,0)$		$J_z(r,L)$		$J_r(R,z)$	
	Ref. [57]	CW	Ref. [57]	CW	Ref. [57]	CW
0.015625	0.59021	0.590068	0.09102	0.090259	0.21531	0.220971
0.078125	0.59103	0.590893	0.09075	0.089980	0.27892	0.275885
0.140625	0.59295	0.592831	0.09009	0.089330	0.28264	0.281463
0.203125	0.59601	0.595910	0.08907	0.088312	0.26719	0.267710
0.265625	0.60028	0.600180	0.08765	0.086928	0.24449	0.245243
0.328125	0.60577	0.605712	0.08590	0.085179	0.21870	0.219340
0.390625	0.61265	0.612603	0.08378	0.083069	0.19237	0.192856
0.453125	0.62102	0.620983	0.08132	0.080602	0.16691	0.167350
0.515625	0.63104	0.631027	0.07852	0.077782	0.14326	0.143629
0.578125	0.64294	0.642974	0.07539	0.074611	0.12179	0.122042
0.640625	0.65702	0.657150	0.07194	0.071093	0.10251	0.102662
0.703125	0.67379	0.674027	0.06806	0.067226	0.08531	0.085388
0.765625	0.69389	0.694313	0.06362	0.063002	0.06999	0.070010
0.828125	0.71858	0.719165	0.05877	0.058401	0.05631	0.056236
0.890625	0.75016	0.750747	0.05348	0.053363	0.04391	0.043679
0.984375	0.82761	0.826356	0.04458	0.044420	0.02517	0.025453

Note: $r = Rx$, $z = Lx$.

In addition, the integral approximation used in [109] makes it difficult to deal with more complex problems. To lead with homogeneous and non-homogeneous scattering media exposed to both uniform and Gaussian distributions of normal collimated flux, Hsu and Tan [57] proposed the use of the YIX method and the quadrature method. However, accuracy has been compromised by the ray effect caused by the YIX method, as can be seen in the Tables 4.40 and 4.41. The current work results are more precise, with the expected absolute error being smaller than 2×10^{-4} for Table 4.40 and smaller than 8×10^{-5} for Table 4.41.

The results presented in the Tables 4.42-4.44 show the convergence of the used algorithm for the Case 2 case with a cylindrical medium with $R = 0.125$, $L = 0.25$, and $\sigma_s = 1$. These tables illustrate the fast convergence of the scalar flux

and the current for cylinders with thin dimensions. The results in these tables are in agreement with those presented by Wu and Wu [109] and $N = 401$ is large enough to expected an absolute error less than 5×10^{-6}.

Table 4.42: Convergence of scalar flux $\Phi(r, z)$ for Case 2, $R = 0.125$, $L = 0.25$, $\sigma_s = 1$.

	N = 41	N = 101	N = 201	N = 401	N = 801	N = 1601
$\Phi(0, 0)$	1.079707	1.079717	1.079719	1.079720	1.079721	1.079721
$\Phi(0, 0.5L)$	1.013979	1.013969	1.013965	1.013963	1.013962	1.013962
$\Phi(0, L)$	0.848599	0.848596	0.848594	0.848593	0.848592	0.848592
$\Phi(0.5R, 0)$	1.073425	1.073431	1.073432	1.073433	1.073433	1.073433
$\Phi(0.5R, 0.5L)$	1.003311	1.003300	1.003296	1.003294	1.003293	1.003292
$\Phi(0.5R, L)$	0.843021	0.843018	0.843017	0.843016	0.843015	0.843015
$\Phi(R, 0)$	1.044365	1.044353	1.044349	1.044346	1.044345	1.044344
$\Phi(R, 0.5L)$	0.952028	0.952017	0.952012	0.952010	0.952009	0.952008
$\Phi(R, L)$	0.818275	0.818269	0.818267	0.818266	0.818265	0.818265

Table 4.43: Convergence of radial component of current for Case 2, $R = 0.125$, $L = 0.25$, $\sigma_s = 1$.

	N = 41	N = 101	N = 201	N = 401	N = 801	N = 1601
$J_r(0, z)$	0.000000	0.000000	0.000000	0.000000	0.000000	0.000000
$J_r(0.5R, 0)$	0.012697	0.012694	0.012692	0.012692	0.012691	0.012691
$J_r(0.5R, 0.5L)$	0.020048	0.020046	0.020045	0.020044	0.020044	0.020044
$J_r(0.5R, L)$	0.011454	0.011453	0.011452	0.011452	0.011451	0.011451
$J_r(R, 0)$	0.026104	0.026094	0.026090	0.026089	0.026088	0.026087
$J_r(R, 0.5L)$	0.042657	0.042651	0.042649	0.042648	0.042647	0.042647
$J_r(R, L)$	0.022885	0.022884	0.022883	0.022883	0.022883	0.022883

Table 4.44: Convergence of axial component of current for Case 2 $R = 0.125$, $L = 0.25$, $\sigma_s = 1$.

	N = 41	N = 101	N = 201	N = 401	N = 801	N = 1601
$J_z(0,0)$	0.955321	0.955321	0.955321	0.955321	0.955321	0.955321
$J_z(0,0.5L)$	0.885656	0.885646	0.885642	0.885641	0.885640	0.885640
$J_z(0,L)$	0.819450	0.819441	0.819438	0.819436	0.819435	0.819435
$J_z(0.5R,0)$	0.958964	0.958965	0.958965	0.958965	0.958965	0.958965
$J_z(0.5R,0.5L)$	0.885333	0.885323	0.885319	0.885318	0.885317	0.885316
$J_z(0.5R,L)$	0.816034	0.816026	0.816023	0.816022	0.816021	0.816021
$J_z(R,0)$	0.976449	0.976449	0.976449	0.976449	0.976449	0.976449
$J_z(R,0.5L)$	0.884145	0.884134	0.884130	0.884128	0.884127	0.884127
$J_z(R,L)$	0.800612	0.800604	0.800602	0.800600	0.800600	0.800599

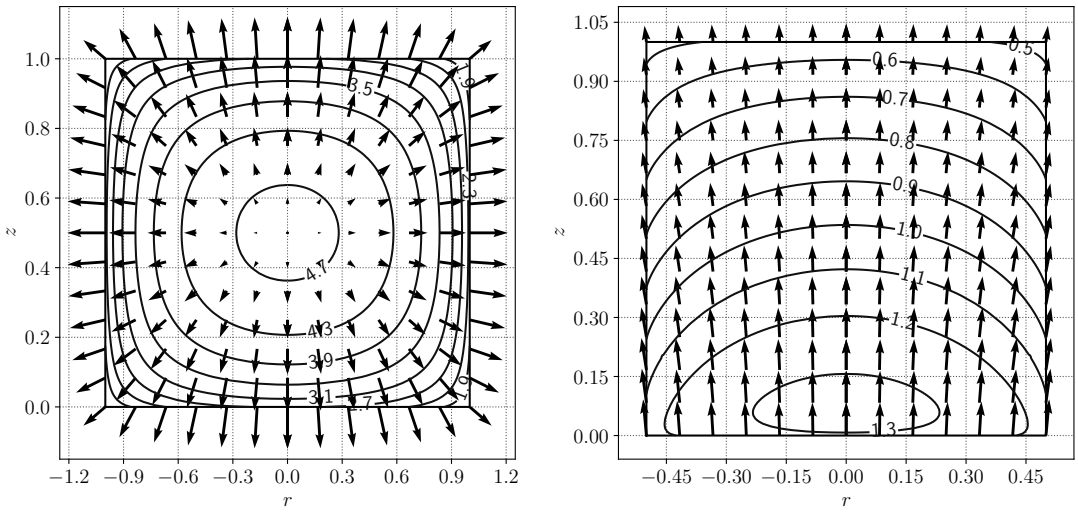

Figure 4.5: Contour lines of the scalar flux and vector field of the current for Case 1 with $R = L = 1$ (left) and for Case 2 with $R = 0.5$ and $L = 1$ (right).

In Figure 4.5 we present the contour lines of the scalar flux and vector field of the current for Cases 1 and 2. For Case 1, the figure shows the increasing of the current as the point approaches to the boundaries in a medium with $R = L = 1$ and $\sigma_s = 0.5$. In the same problem it is noted that as the point approaches to the boundaries the decreasing of scalar flux accelerates. For Case 2, a medium of $R = 0.5$, $L = 1$, and $\sigma_s = 1$ is treated. With no internal source in the cylinder, the behavior of the scalar flux and of the current are dominated by incidence in the bottom surface ($z = 0$), with both decreasing as z increases.

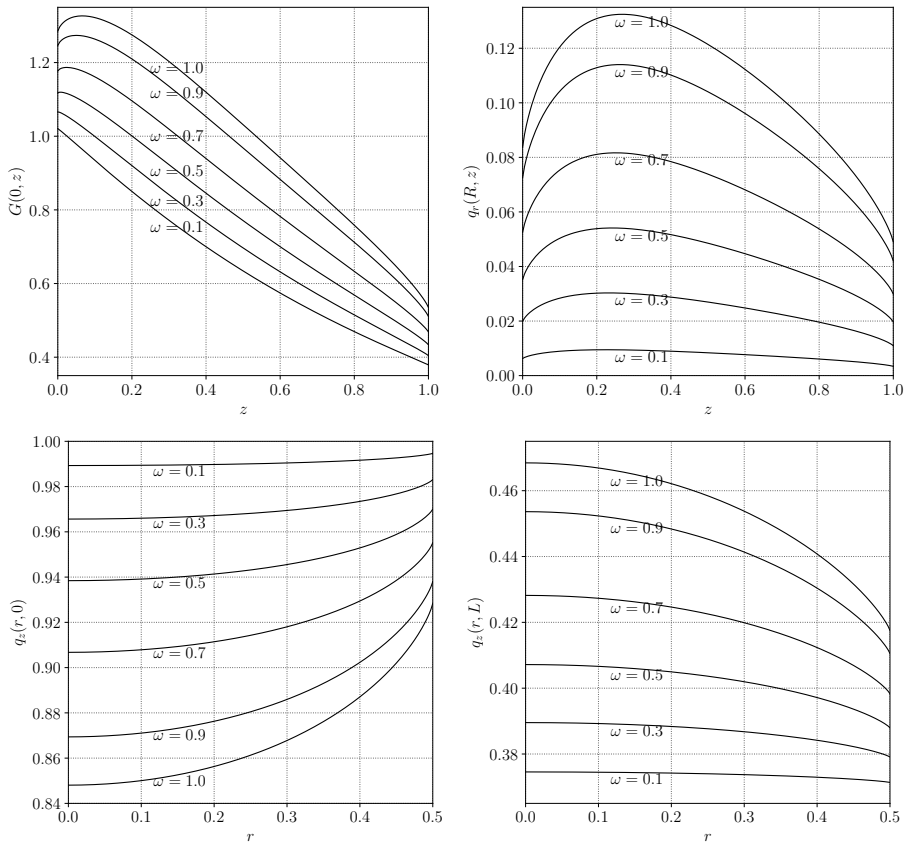

Figure 4.6: Influence of σ_s on $\Phi(0,z)$, $J_r(R,z)$, $J_z(r,0)$, and $J_z(r,L)$ for Case 2 with $R = 0.5$ and $L = 1$.

Lastly, Figure 4.6 presents the effects of σ_s on $\Phi(0,z)$, $J_r(R,z)$, $J_z(r,0)$, and $J_z(r,L)$ for Case 2 with $R = 0.5$ and $L = 1$. It should be noted that the scalar flux and current profiles in the figure are generated with $N_r = N_z = 201$, a size of mesh sufficient to ensure the accuracy necessary to build the graphics. For cases of large dimensions it may be necessary to use a more refined mesh. The smoothness of the curves in the figure and the accuracy of the numerical results presented in the tables show that the ray effect does not appear or, at least, is irrelevant when using the proposed methodology to solve the benchmark problems.

5 FINAL CONSIDERATIONS

Given the difficulty in solving the transport equation, many papers have been published with different deterministic methods proposed in recent years. Some of these methods were briefly discussed in this work.

Among these methodologies, the integral methods stand out for producing accurate numerical results. In particular, the Nyström method is a well-established methodology for the numerical solution of integral equations. Such method consists in replacing the integral operator by a quadrature numerical scheme and producing a linear system to be solved, being of easy numerical implementation.

In the present study, we used the integral formulation of neutron transport equation to solve, by the Nyström method with the singularity-subtraction strategy, three different problems in cylindrical geometries. The following assumptions were considered: steady-state, one-energy group, homogeneous and nonmultiplying medium, and isotropic scattering and source.

The first problem (Problem 1) consisted in determining scalar flux and current for the case of the infinitely long axisymmetric cylinder. For this domain, the problem of criticality of the system was also approached. Extremely satisfactory results were obtained, noting that the analytical treatment of the problem (using elliptic integrals, for example) was fundamental to obtain highly accurate results. In particular, results with the same precision compared to the well-established benchmarks of Siewert and Thomas Jr. [94] and Ganapol [47,48] were obtained, a feat not achieved by authors who dealt with similar problems (and whose researches were mentioned in this work).

The results obtained showed that our methodology is effective in the numerical solution of transport problems in cylindrical geometries, whose results are scarce in the literature. Furthermore, compared to the F_N method, our methodology

has the advantage of using a formulation that can be extended, with some ease, to more general problems. Thus, numerical results for more complex problems can be generated and validation can be done from simpler problems. An example of this is the second problem treated throughout the thesis (Problem 2: infinitely long cylinder without the axisymmetry assumption). Although no available results for scalar flux were found in the literature for this case, the comparison with Problem 1 showed that the results obtained are of high quality. Also, with the study of Problem 2, it was possible to find a suitable quadrature for the treatment of the angular variable in non-axissymmetric multidimensional problems.

In the last problem solved in the present work (Problem 3) a finite axisymmetric cylinder was considered. Once again high precision numerical results for scalar flux and current were provided and validated. When using a large L, the comparison with results obtained for Problem 1 showed excellent agreement. Furthermore, there was a good agreement between the current work results and the results available in the literature, noting that many of them are presented only in graphs (which impeded a head-to-head comparison). The development and results obtained for Problem 3 showed that the Nyström method with singularity-subtraction is also an effective technique to deal with cylindrical problems with variation of flux in the axial direction.

For all problems solved in this thesis, mathematical techniques were applied to deal with singularities, optimize computations, and reduce memory storage. The high precision numerical results for scalar flux and current were obtained using a personal computer (Intel Core i7-7500U 2.70GHz machine). In addition to being consistent with those available in the literature, our results are expected to be more accurate in several cases. Furthermore, it should be noted that the numerical experiments were performed with constants source term and boundary condition in such a way that it was possible to compare the results with those available in the

literature. However, analogous developments can be made to produce more general results.

Finally, we note that the efforts directed to this work in the research group coordinated by professor Fabio S. de Azevedo implied in the presentation of a paper in a conference and the publication of articles on the subject, namely:

- Short communication presented in ICM 2018 (Rio de Janeiro - RJ): "Integral formulation and numerical simulations for the neutron transport equation in two-dimensional axisymmetric cylindrical geometry" [22];
- Paper published (see at https://doi.org/10.1016/j.anucene.2020.107701) in the journal Annals of Nuclear Energy: "Nyström method applied to the transport equation in an axisymmetric cylinder" [23]. This paper presents results referring to Problem 1;
- Paper published (see at https://doi.org/10.1016/j.jqsrt.2022.108087) in Journal of Quantitative Spectroscopy & Radiative Transfer: "Numerical Results for Radiative Heat Transfer in Finite Cylindrical Medium with Isotropic Scattering" [24]. This paper presents results referring to Problem 3.

5.1 Perspectives

Recently, Fabio S. de Azevedo and his research group have been successful in the use of Nyström method with the singularity-subtraction strategy to solve different problems of neutron transport in X-Y geometry. Such method has been shown to be an efficient tool when analytical and computational refinements are made in order to obtain numerical precision and to accelerate the computation process, producing high quality numerical results with reasonable computational times.

Here we presented numerical results for transport problems in cylindrical geometries considering assumptions of constant properties and isotropic scattering. In this way, we can extend this methodology in order to solve different neutron transport problems, exploring, for example, different geometries. With an additional mathematical development, the method also has the potential to produce high precision results for more general cases of neutron transport in a cylinder, as problems considering one or more of the following hypotheses

- Finite non-axisymmetric cylindrical medium;
- Reflecting boundary condition;
- Anisotropic scattering
- Non-homogeneous medium;
- Hollow cylindrical medium.

Another task is to optimize even more the implementation both analytically as well as in coding techniques, testing a different way to handle diagonal singularities, for example. Convergence acceleration techniques should also be used.

REFERÊNCIAS

[1] Ab-Initio Physics Research Group. Cubature (Multi-dimensional integration), 2015.

[2] Abulwafa, E., and Attia, M. Integral form of radiative transfer equation in inhomogeneous cylindrical medium with anisotropic scattering. *Journal of Quantitative Spectroscopy and Radiative Transfer 62*, 6 (1999), 755–763.

[3] Abulwafa, E., and Attia, M. Radiative transfer in inhomogeneous solid cylinder with anisotropic scattering using galerkin method. *Journal of Quantitative Spectroscopy and Radiative Transfer 66*, 5 (2000), 487–500.

[4] Adams, M. L., and Larsen, E. W. Fast iterative methods for discrete-ordinates particle transport calculations. *Progress in nuclear energy 40*, 1 (2002), 3–159.

[5] Altaç, Z. Radiative transfer in absorbing, emitting and linearly anisotropic-scattering inhomogeneous cylindrical medium. *Journal of Quantitative Spectroscopy and Radiative Transfer 77*, 2 (2003), 177–192.

[6] Altaç, Z. Exact series expansions, recurrence relations, properties and integrals of the generalized exponential integral functions. *Journal of Quantitative Spectroscopy and Radiative Transfer 104*, 3 (2007), 310–325.

[7] Altaç, Z., and Spinrad, B. I. The sk n method i: A high-order transport approximation to neutron transport problems. *Nuclear Science and Engineering 106*, 4 (1990), 471–479.

[8] Altaç, Z. *The SK (N) approximation: a new method for solving integral transport equations*. PhD thesis, Iowa State University, 1989.

[9] Altaç, Z., and Sert, Z. Application of alternative synthetic kernel approximation to radiative transfer in regular and irregular two-dimensional media. *Journal of Quantitative Spectroscopy and Radiative Transfer 187* (2017), 293 – 309.

[10] Altaç, Z., and Tekkalmaz, M. Nodal synthetic kernel (N-SKN) method for solving neutron transport equation in one- and two-dimensional X-Y geometries. *Annals of Nuclear Energy 64* (2014), 320–332.

[11] Azmy, Y., and Sartori, E. *Nuclear computational science: a century in review*. Springer, 2010.

[12] Badruzzaman, A. An efficient algorithm for nodal-transport solutions in multidimensional geometry. *Nuclear Science and Engineering 89*, 3 (1985), 281–290.

[13] Barichello, L., da Cunha, R., Picoloto, C., and Tres, A. An analytical approach for a nodal formulation of a two-dimensional fixed-source neutron transport problem in heterogeneous medium. *Kerntechnik 80*, 2 (2015), 167–173.

[14] Barichello, L., Picoloto, C., and da Cunha, R. The ado-nodal method for solving two-dimensional discrete ordinates transport problems. *Annals of Nuclear Energy 108* (2017), 376–385.

[15] Barichello, L. B., and Siewert, C. E. A discrete-ordinates solution for a non-grey model with complete frequency redistribution. *Journal of Quantitative Spectroscopy and Radiative Transfer 62*, 6 (1999), 665–675.

[16] Barichello, L. B., Tres, A., Picoloto, C. B., and Azmy, Y. Y. Recent Studies on the Asymptotic Convergence of the Spatial Discretiza-

tion for Two-Dimensional Discrete Ordinates Solutions. *Journal of Computational and Theoretical Transport 45*, 4 (2016), 299–313.

[17] Bell, G. I., and Glasstone, S. Nuclear reactor theory. Tech. rep., US Atomic Energy Commission, Washington, DC (United States), 1970.

[18] Bickley, W. G., and Nayler, J. Xxv. a short table of the functions ki n (x), from n= 1 to n= 16. *The London, Edinburgh, and Dublin Philosophical Magazine and Journal of Science 20*, 132 (1935), 343–347.

[19] Blair, J. M., Edwards, C. A., and Johnson, J. H. Rational chebyshev approximations for the bickley functions kin(x). *Mathematics of Computation 32*, 143 (1978), 876–886.

[20] Boltzmann, L. Weitere studien über das wärmegleichgewicht unter gasmolekülen. In *Kinetische Theorie II*. Springer, 1970, pp. 115–225.

[21] Brunner, T. A. Forms of approximate radiation transport. *Sandia report* (2002).

[22] Bublitz, C., De Azevedo, F. S., and Sauter, E. Integral formulation and numerical simulations for the neutron transport equation in two-dimensional axisymmetric cylindrical geometry. In *ICM 2018: International Congress of Mathematicians* (Rio de Janeiro, Brazil, 2018).

[23] Bublitz, C., de Azevedo, F. S., and Sauter, E. Nyström method applied to the transport equation in an axisymmetric cylinder. *Annals of Nuclear Energy 148* (2020), 107701.

[24] Bublitz, C., Lorensi, G. A., de Azevedo, F. S., and Sauter, E. Numerical results for radiative heat transfer in finite cylindrical medium with isotropic scattering. *Journal of Quantitative Spectroscopy and Radiative Transfer* (2022), 108087.

[25] Caldeira, A. D. Application of the pn method to the matrix form transport equation. *Annals of Nuclear Energy 32*, 17 (2005), 1889–1894.

[26] Carlson, B. Elliptic integrals of the first kind. *SIAM Journal on Mathematical Analysis 8*, 2 (1977), 231–242.

[27] Carlson, B. C. A table of elliptic integrals of the second kind. *Mathematics of Computation 49*, 180 (1987), 595–606.

[28] Chai, J. C., Lee, H. S., and Patankar, S. V. Ray effect and false scattering in the discrete ordinates method. *Numerical Heat Transfer, Part B Fundamentals 24*, 4 (1993), 373–389.

[29] Chen, X., and Sutton, W. Radiative transfer in finite cylindrical media using transformed integral equations. *Journal of Quantitative Spectroscopy and Radiative Transfer 77*, 3 (2003), 233–271.

[30] Cody, W. Chebyshev approximations for the complete elliptic integrals k and e. *Mathematics of Computation 19*, 89 (1965), 105–112.

[31] Cools, R., and Kim, K. J. A survey of known and new cubature formulas for the unit disk. *Korean Journal of Computational & Applied Mathematics 7*, 3 (2000), 477–485.

[32] Cromianski, S. *Um estudo sobre equações auxiliares em formulações nodais para solução da equação de transporte de nêutrons bidimensionais.* Tese de Doutorado, PPGMAp, UFRGS, 2016.

[33] Cromianski, S., Rui, K., and Barichello, L. A study on boundary fluxes approximation in explicit nodal formulations for the solution of the two-dimensional neutron transport equation. *Progress in Nuclear Energy 110* (2019), 354–363.

[34] Davison, B., Sykes, J. B., and Cohen, E. R. *Neutron transport theory.* Clarendon Press, 1958.

[35] De Abreu, M. P. Numerical methods for the generation of the spectrum of the multigroup slab-geometry discrete ordinates operator in neutron transport theory. *Annals of Nuclear Energy 29*, 15 (2002), 1837–1853.

[36] De Azevedo, F. S., Sauter, E., Konzen, P. H. A., Thompson, M., and Barichello, L. B. Integral formulation and numerical simulations for the neutron transport equation in x-y geometry. *Annals of Nuclear Energy 112* (2018), 735–747.

[37] De Azevedo, F. S., Sauter, E., Thompson, M., and Vilhena, M. T. Existence theory and simulations for one-dimensional radiative flows. *Annals of Nuclear Energy 38*, 5 (2011), 1115–1124.

[38] De Azevedo, F. S., Sauter, E., Thompson, M., and Vilhena, M. T. Solution of the radiative heat transfer equation with internal energy sources in a slab by the green's functions decomposition method for anisotropic scattering. *Progress in Nuclear Energy 65* (2013), 64–69.

[39] De Azevedo, F. S., Thompson, M., Sauter, E., and Vilhena, M. T. Existence theory for a one-dimensional problem arising from the boundary layer analysis of radiative flows. *Progress in Nuclear Energy 53*, 8 (2011), 1105–1113.

[40] Delves, L. M., and Mohamed, J. *Computational methods for integral equations*. CUP Archive, 1988.

[41] Döner, N., and Altaç, Z. Solution of the radiative transfer problems in two-dimensional participating cylindrical medium with isotropic scattering using the skn approximation. *Advanced computational methods in heat transfer IX 53* (2006), 109.

[42] Duderstadt, J. J. *Nuclear reactor analysis*. Wiley, 1976.

[43] Duderstadt, J. J., and Martin, W. R. *Transport theory.* John Wiley & Sons, 1979.

[44] Frank, M., Klar, A., Larsen, E. W., and Yasuda, S. Time-dependent simplified pn approximation to the equations of radiative transfer. *Journal of Computational Physics 226*, 2 (2007), 2289–2305.

[45] Free Software Foundation, Inc. GSL - GNU Scientific Library, 2009.

[46] Fukushima, T. Fast computation of complete elliptic integrals and jacobian elliptic functions. *Celestial Mechanics and Dynamical Astronomy 105*, 4 (2009), 305.

[47] Ganapol, B. D. Analytical benchmarks for nuclear engineering applications. *Case Studies in Neutron Transport Theory. Organisation for Economic Co-operation and Development* (2008).

[48] Ganapol, B. D. A neutron transport benchmark in one-dimensional cylindrical geometry: Revisited. *Nuclear science and engineering 159*, 2 (2008), 169–181.

[49] Garcia, R. D. M., Siewert, C. E., and Thomas Jr, J. R. The classical spherical-harmonics method in transport theory. *Transactions of the American Nuclear Society 71*, CONF-941102– (1994).

[50] Gelbard, E. Panel discussion. *Transactions of the American Nuclear Society 8* (1965), 226.

[51] Gelbard, E. M. Application of spherical harmonics method to reactor problems. *Bettis Atomic Power Laboratory, WAPD-BT-20* (1960).

[52] Gelbard, E. M., Davis, J., and Pearson, J. Iterative solutions to the p1 and double-p1 equations1. *Nuclear Science and Engineering 5*, 1 (1959), 36–44.

[53] Golub, G., and Van Loan, C. *Matrix Computations*, 4 ed. JHU Press, 2013.

[54] Gradshteyn, I. S., and Ryzhik, I. M. *Table of integrals, series, and products*. Academic press, 2014.

[55] Hauser, E. B., Pazos, R. P., and de Vilhena, M. T. An error bound estimate and convergence of the nodal-ltsn solution in a rectangle. *Annals of Nuclear Energy 32*, 10 (2005), 1146–1156.

[56] Hou, M.-F., and Wu, C.-Y. Integral equation method applied to radiative transfer in a 2-D absorbing-scattering refractive medium. *International Communications in Heat and Mass Transfer 43* (2013), 63–68.

[57] Hsu, P.-F., Tan, Z.-M., Wu, S.-H., and Wu, C.-Y. Radiative heat transfer in finite cylindrical homogeneous and nonhomogeneous scattering media exposed to collimated radiation. *Numerical Heat Transfer: Part A: Applications 35*, 6 (1999), 655–679.

[58] Inc., W. R. Wolfram—alpha. Champaign, IL, 2018.

[59] Jeans, J. H. The equations of radiative transfer of energy. *Monthly Notices of the Royal Astronomical Society 78* (1917), 28–36.

[60] Kavenoky, A. The cn method of solving the transport equation: application to plane geometry. *Nuclear Science and Engineering 65*, 2 (1978), 209–225.

[61] Lamarsh, J. R. Introduction to nuclear reactor theory. *Goldstein Herbert. Toi* (1966).

[62] Larsen, E. W. Diffusion theory as an asymptotic limit of transport theory for nearly critical systems with small mean free paths. *Annals of Nuclear Energy 7*, 4-5 (1980), 249–255.

[63] Larsen, E. W., Thömmes, G., Klar, A., Seaïd, M., and Götz, T. Simplified PN Approximations to the Equations of Radiative Heat Transfer and Applications. *Journal of Computational Physics 183*, 2 (2002), 652–675.

[64] Lathrop, K. D. Ray effects in discrete ordinates equations. *Nuclear Science and Engineering 32*, 3 (1968), 357–369.

[65] Lathrop, K. D. Remedies for ray effects. *Nuclear Science and Engineering 45*, 3 (1971), 255–268.

[66] Lawrence, R. D. Progress in nodal methods for the solution of the neutron diffusion and transport equations. *Progress in Nuclear Energy 17*, 3 (1986), 271 – 301.

[67] Lax, P. D. *Functional Analysis*. Wiley-Interscience, New York, NY, USA, 2002.

[68] Lewis, E. E., and Miller, W. *Computational methods of neutron transport*. Wiley-Interscience, New York, 1984.

[69] Li, H., Ozisik, M., and Tsai, J. Two-dimensional radiation in a cylinder with spatially varying albedo. *Journal of thermophysics and heat transfer 6*, 1 (1992), 180–182.

[70] Lorensi, G. *Simulações de problemas de transporte de partículas em geometria X-Y*. Dissertação de Mestrado, PPGMAp, UFRGS, 2016.

[71] Loyalka, S. K. A Numerical Method for Solving Integral Equations of Neutron Transport. *Nucl. Sci. Eng. 56*, 3 (1975), 317–319.

[72] Loyalka, S. K., and Naz, S. One speed black sphere problem: Some benchmark results. *Annals of Nuclear Energy 35*, 9 (2008), 1774–1778.

[73] Loyalka, S. K., and Tsai, R. W. A Numerical Method for Solving Integral Equations of Neutron Transport-II. *Nuclear Science and Engineering 58*, 2 (1975), 193–202.

[74] Maiorino, J. R. A equação de transporte de boltzmann e sua importância para a física dos reatores nucleares. *Revista Brasileira de Ensino de Física 29*, 1 (2007), 1–2.

[75] Maplesoft, a division of Waterloo Maple Inc. Maple 15, 2015.

[76] Mattson, T., and Meadows, L. A "hands-on" introduction to openmp. *Intel Corporation* (2014).

[77] Mitsis, G. J. Transport solutions to the monoenergetic critical problems (thesis). Tech. rep., Argonne National Lab., Ill., 1963.

[78] Modest, M. F. *Radiative heat transfer*, second ed. Academic Press, San Diego, 2003.

[79] Naz, S., and Loyalka, S. K. One speed criticality problems for a bare slab and sphere: Some benchmark results – II. *Annals of Nuclear Energy 35*, 12 (2008), 2426–2431.

[80] NIST. *Digital Library of Mathematical Functions*. http://dlmf.nist.gov/, Release 1.0.13 of 2016-09-16, 2016. F. W. J. Olver, A. B. Olde Daalhuis, D. W. Lozier, B. I. Schneider, R. F. Boisvert, C. W. Clark, B. R. Miller and B. V. Saunders, eds.

[81] Nyström, E. J. Über Die Praktische Auflösung von Integralgleichungen mit Anwendungen auf Randwertaufgaben. *Acta Mathematica 54*, 1 (1930), 185–204.

[82] Olbrant, E., Larsen, E. W., Frank, M., and Seibold, B. Asymptotic derivation and numerical investigation of time-dependent simplified pn equations. *Journal of Computational Physics 238* (2013), 315–336.

[83] Pazos, R. P., Thompson, M., and Vilhena, M. T. Error bounds for spectral collocation method for the linear boltzmann equation. *International Journal of Computational and Numerical Analysis and Applications 1*, 3 (2002), 237–268.

[84] Picoloto, C., Tres, A., da Cunha, R., and Barichello, L. Closed-form solutions for nodal formulations of two dimensional transport problems in heterogeneous media. *Annals of Nuclear Energy 86* (2015), 65–71.

[85] Press, W. H., Flannery, B. P., Teukolsky, S. A., Vetterling, W. T., et al. Numerical recipes, 1989.

[86] Sanchez, R. Generalization of asaoka method to linearly anisotropic scattering: benchmark data in cylindrical geometry. Tech. rep., CEA Centre d'Etudes Nucleaires de Cadarache, 1975.

[87] Sanchez, R., and Ganapol, B. D. Benchmark values for monoenergetic neutron transport in one-dimensional cylindrical geometry with linearly anisotropic scattering. *Nuclear Science and Engineering 84*, 1 (1983), 61–67.

[88] Sauter, E., de Azevedo, F., and Konzen, P. Nyström method applied to the transport equation in a semi-reflective rectangle. *Journal of Computational and Theoretical Transport* (2019), 1–22.

[89] Sauter, E., de Azevedo, F. S., Thompson, M., and Vilhena, M. T. Eigenvalues of the anisotropic transport equation in a slab. *Transport Theory and Statistical Physics 41*, 5-6 (2012), 448–472.

[90] Segatto, C. F., Vilhena, M. T., and Leite, S. Q. B. The ltsn angular multigrid approach in a slab. *Journal of Quantitative Spectroscopy and Radiative Transfer 95*, 3 (2005), 415–422.

[91] Segatto, C. F., Vilhena, M. T., Thompson, M., and Barros, R. C. Generalized discrete ordinates methods for neutral particle transport problems in slab geometry. *Progress in Nuclear Energy 50*, 7 (2008), 788–794.

[92] Siewert, C., and Benoist, P. The fn method in neutron-transport theory. part i: Theory and applications. *Nuclear Science and Engineering 69*, 2 (1979), 156–160.

[93] Siewert, C., and Thomas Jr, J. Radiative transfer calculations in spheres and cylinders. *Journal of Quantitative Spectroscopy and Radiative Transfer 34*, 1 (1985), 59–64.

[94] Siewert, C. E., and Thomas Jr, J. R. Neutron transport calculations in cylindrical geometry. *Nuclear Science and Engineering 87*, 2 (1984), 107–112.

[95] Spinrad, B. I., and Altaç, Z. The sk n method ii: Heterogeneous problems. *Nuclear Science and Engineering 106*, 4 (1990), 480–488.

[96] Sutton, W., and Chen, X. A general integration method for radiative transfer in 3-d non-homogeneous cylindrical media with anisotropic scattering. *Journal of Quantitative Spectroscopy and Radiative Transfer 84*, 1 (2004), 65–103.

[97] Thomas Jr, J., Southers, J., and Siewert, C. The critical problem for an infinite cylinder. *Nuclear Science and Engineering 84*, 2 (1983), 79–82.

[98] Thompson, M., De Vilhena, M. T., and Bodmann, B. E. J. Existence theory for radiative flows. *Transport Theory and Statistical Physics 37*, 2-4 (2008), 307–326.

[99] Thompson, M., Segatto, C., and De Vilhena, M. T. Existence theory for the solution of a stationary nonlinear conductive-radiative heat-transfer problem in three space dimensions. *Transport Theory and Statistical Physics 33*, 5-7 (2004), 563–576.

[100] Thynell, S. The integral form of the equation of transfer in finite, two-dimensional, cylindrical media. *Journal of Quantitative Spectroscopy and Radiative Transfer 42*, 2 (1989), 117–136.

[101] Thynell, S., et al. Radiation transfer in absorbing, emitting, isotropically scattering, homogeneous cylindrical media. *Journal of Quantitative Spectroscopy and Radiative Transfer 38*, 6 (1987), 413–426.

[102] Thynell, S., and Özışık, M. Integral form of the equation of transfer for an isotropically scattering, inhomogeneous solid cylinder. *Journal of Quantitative Spectroscopy and Radiative Transfer 36*, 6 (1986), 497–503.

[103] Tres, A., Picoloto, C. B., Filho, J. P., da Cunha, R. D., and Barichello, L. B. Explicit formulation of a nodal transport method for discrete ordinates calculations in two-dimensional fixed-source problems. *Kerntechnik 79*, 2 (2014), 155–162.

[104] Tsai, R. W., and Loyalka, S. K. Numerical method for solving integral equations of neutron transport: III. *Nuclear Science and Engineering 61* (1976), 536–540.

[105] Vargas, R. F., Segatto, C. F., and Vilhena, M. T. Solution of the radiative heat transfer equation with internal energy sources in a slab by the method. *Journal of Quantitative Spectroscopy and Radiative Transfer 105*, 1 (2007), 1–7.

[106] Vilhena, M. T., and Barichello, L. B. A new analytical approach to solve the neutron transport equation. *Kerntechnik 56*, 5 (1991), 334–336.

[107] Westfall, R. Benchmark solutions for the infinite critical cylinder. Tech. rep., Oak Ridge National Lab., 1983.

[108] Wu, S.-C., and Wu, C.-Y. Partition-extrapolation integration applied to radiative transfer in cylindrical media. *Journal of Quantitative Spectroscopy and Radiative Transfer 48*, 3 (1992), 279–286.

[109] Wu, S.-C., and Wu, C.-Y. Radiative heat transfer in a two-dimensional cylindrical medium exposed to collimated radiation. *International communications in heat and mass transfer 24*, 4 (1997), 475–484.

[110] Yosida, K. *Functional Analysis*, 6th ed. Springer-Verlag, Berlin, 1966.

[111] Zhang, J., and Sutton, W. Multidimensional radiative transfer in absorbing, emitting, and linearly anisotropic scattering cylindrical medium with space-dependent properties. *Journal of Quantitative Spectroscopy and Radiative Transfer 52*, 6 (1994), 791–808.

[112] Zhang, J.-M., and Sutton, W. H. Predictions of radiative transfer in two-dimensional nonhomogeneous participating cylindrical media. *Journal of thermophysics and heat transfer 10*, 1 (1996), 47–53.

[113] Zhou, R.-R., and Li, B.-W. Chebyshev collocation spectral method for one-dimensional radiative heat transfer in linearly anisotropic-scattering cylindrical medium. *Journal of Quantitative Spectroscopy and Radiative Transfer 189* (2017), 206–220.